

Spring 1997

Numerical analysis for blood distribution in complete flow cross-section microvascular networks

Jewen Xiao

University of New Hampshire, Durham

Follow this and additional works at: <https://scholars.unh.edu/dissertation>

Recommended Citation

Xiao, Jewen, "Numerical analysis for blood distribution in complete flow cross-section microvascular networks" (1997). *Doctoral Dissertations*. 1965.

<https://scholars.unh.edu/dissertation/1965>

This Dissertation is brought to you for free and open access by the Student Scholarship at University of New Hampshire Scholars' Repository. It has been accepted for inclusion in Doctoral Dissertations by an authorized administrator of University of New Hampshire Scholars' Repository. For more information, please contact nicole.hentz@unh.edu.

INFORMATION TO USERS

This manuscript has been reproduced from the microfilm master. UMI films the text directly from the original or copy submitted. Thus, some thesis and dissertation copies are in typewriter face, while others may be from any type of computer printer.

The quality of this reproduction is dependent upon the quality of the copy submitted. Broken or indistinct print, colored or poor quality illustrations and photographs, print bleedthrough, substandard margins, and improper alignment can adversely affect reproduction.

In the unlikely event that the author did not send UMI a complete manuscript and there are missing pages, these will be noted. Also, if unauthorized copyright material had to be removed, a note will indicate the deletion.

Oversize materials (e.g., maps, drawings, charts) are reproduced by sectioning the original, beginning at the upper left-hand corner and continuing from left to right in equal sections with small overlaps. Each original is also photographed in one exposure and is included in reduced form at the back of the book.

Photographs included in the original manuscript have been reproduced xerographically in this copy. Higher quality 6" x 9" black and white photographic prints are available for any photographs or illustrations appearing in this copy for an additional charge. Contact UMI directly to order.

UMI

A Bell & Howell Information Company
300 North Zeeb Road, Ann Arbor MI 48106-1346 USA
313/761-4700 800/521-0600

**NUMERICAL ANALYSIS FOR BLOOD DISTRIBUTION IN COMPLETE FLOW
CROSS-SECTION MICROVASCULAR NETWORKS**

BY

Jewen Xiao

**B.S. South China University of Technology, 1983
M.S. South China University of Technology, 1986**

DISSERTATION

**Submitted to the University of New Hampshire
in Partial Fulfillment of
the Requirement for the degree of**

Doctor of Philosophy

in

Engineering

May, 1997

UMI Number: 9730848

UMI Microform 9730848
Copyright 1997, by UMI Company. All rights reserved.

**This microform edition is protected against unauthorized
copying under Title 17, United States Code.**

UMI
300 North Zeeb Road
Ann Arbor, MI 48103

This dissertation has been examined and approved.



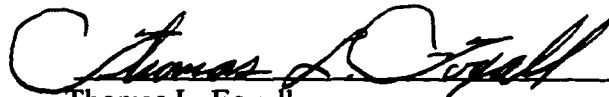
Dissertation director, Russell T. Carr
Associate Professor of Chemical Engineering



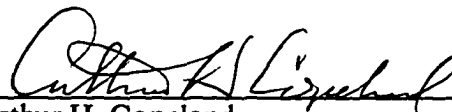
Virendra K. Mathur
Professor of Chemical Engineering



Dale P. Barkey
Associate Professor of Chemical Engineering



Thomas L. Foxall
Associate Professor of Animal and Nutritional Science



Arthur H. Copeland
Professor Of Mathematics

December 19, 1996

Date

This dissertation is dedicated to my wife Yu Zhong.

ACKNOWLEDGEMENTS

Here I would like to thank my advisor, Dr. R. T. Carr, for his wonderful ideas and encouragement to me throughout this study.

Thanks to Dr. Mathur, Dr. Barkey, Dr. Foxall, and Dr. Copeland for their help serving as my committee members.

The analytical solution, the *in vitro* experimental data for serial bifurcations and the function programs visrat, qyc, qstar, partq and fnum and the subroutine program map in Appendix A, computer program are provided courtesy of Dr. Carr.

I would also like to thank Dr. Mary D. S. Frame for providing me the *in vivo* data on vessel diameters and lengths in hamster cremaster muscle.

This study was supported by NIH Grant 5 R01HL49231.

TABLE OF CONTENTS

DEDICATION	iii
ACKNOWLEDGEMENTS.....	iv
LIST OF TABLES.....	vii
LIST OF FIGURES	viii
ABSTRACT.....	xi
CHAPTER	PAGE
I. INTRODUCTION	1
1.1 Introduction	1
1.2 Blood and its Rheology	2
1.3 Definition of Microcirculation.....	5
1.4 Hemodynamics Microcirculation.....	8
1.5 Summary of the Dissertation.....	16
II. MATHEMATICAL MODELS OF PLASMA SKIMMING AT A BIBURCATION AND RBC DISPERSION AT BRANCH SEGMENT	18
2.1 Introduction	18
2.2 Velocity and Red Blood Cell Concentration Profile	19
2.3 The Mapping Technique.....	20
2.4 The RBC Dispersion Process	23
2.5 Comparison of Numerical Solution to Experimental Data	36
III. THE SYMMETRIC RECOVERY LENGTH	46

3.1 The Calculation of Symmetric Recovery Length	46
3.2 Comparison to <i>In Vivo</i> Experimental Data.....	53
IV. HETEROGENEITY OF BLOOD FLOW IN MICROVASCULAR NETWORK.	56
4.1 Introduction.....	56
4.2 Definition of Heterogeneity.....	56
4.3 Complete Flow Cross-Section Network	64
4.4 Computational Results.....	67
V. CONCLUSIONS AND RECOMMENDATIONS.....	80
BIBLIOGRAPHY.....	82
NOMENCLATURE.....	88
APPENDIX A COMPUTER PROGRAM.....	91
APPENDIX B <i>IN VIVO</i> DATA.....	119
APPENDIX C <i>IN VITRO</i> DATA.....	121

LIST OF TABLES

TABLE	PAGE
1-1 Cells in the blood.....	2
1-2 Diameter and flow rate in the microcirculation of various species.....	5
1-3 Bifurcation ratio for some microvascular networks	8
1-4 The ratio of microvessel hematocrit to systemic hematocrit.....	11
2-1 The total red blood cell mass of various distances downstream of the bifurcation .	36
2-2 The linear regression results for different velocity profiles.....	43
2-3 The linear regression results for different dispersion models.....	43
2-4 The linear regression results for variable dispersion and symmetric profile models.....	44
2-5 The range of volumetric flow fraction from Sarelius's data	53
B-1 The experimental data for vessel diameter and unbranched vessel segment	119
C-1 The serial bifurcation experimental data	122

LIST OF FIGURES

FIGURE	PAGE
1-1 The relative viscosity of human blood as a function of shear rate.....	4
1-2 The apparent viscosity of human blood as a function of hematocrit.....	4
2-1 Flat or concave arc separation surface	21
2-2 The mapping technique.....	22
2-3 Indices scheme	28
2-4 Absolute difference between analytical solution and numerical calculation for different dimensionless radii at the angle 54°	35
2-5 Absolute difference between analytical solution and numerical calculation for different dimensionless radii at the angle 126°	35
2-6 Schematic of a serial bifurcation	37
2-7 The parity plot for velocity profile $\omega=2$ model.....	39
2-8 The parity plot for velocity profile $\omega=4$ model.....	39
2-9 The parity plot for velocity profile $\omega=6$ model.....	40
2-10 The parity plot for constant dispersion model.....	40
2-11 The parity plot for variable dispersion model	41
2-12 The parity plot for symmetric profile model	41
2-13 The parity plot for no RBC dispersion model.....	42
2-14 Residual histogram for variable dispersion model.....	44
2-15 Residual histogram for symmetric profile model.....	45
3-1 Dimensionless symmetry recovery length for flat separation surface.....	48

3-2 Dimensionless symmetry recovery length for curved separation surface	49
3-3 Dimensional symmetry recovery length for flat separation surface.....	51
3-4 Dimensional symmetry recovery length for curved separation surface	51
3-5 Schematic of a microvascular tree structure in Hamster cremaster muscles	53
3-6 Comparison of symmetric recovery length and in vivo data for average velocity 1000 μ m/sec.....	55
3-7 Comparison of symmetric recovery length and in vivo data for average velocity 30 μ m/sec.....	55
4-1 Microvascular Network Structure: Branches at the same side	65
4-2 Microvascular Network Structure: Branches alternating or rotating 180 $^{\circ}$	65
4-3 Microvascular Network Structure: Branches alternating 90 $^{\circ}$	66
4-4 Microvascular Network Structure: Branches rotating 90 $^{\circ}$	66
4-5 Microvascular Network Structure: Serial Tree.....	66
4-6 Microvascular Network Structure: Parallel Tree.....	67
4-7 The heterogeneity of hematocrit for a serial tree with six branches.....	68
4-8 The heterogeneity of red blood cell flow for a serial tree with six branches.....	69
4-9 Magnitude of RBC flow heterogeneity as a function of magnitude of blood flow heterogeneity at different total flow rates	71
4-10 Magnitude of RBC flow heterogeneity as a function of magnitude of blood flow heterogeneity for different departure angles.....	72
4-11 Magnitude of RBC flow heterogeneity as a function of magnitude of blood flow heterogeneity at different segment distances for branches at the same side.	73
4-12 Magnitude of RBC flow heterogeneity as a function of magnitude of blood flow heterogeneity at different segment distances for alternating 180 $^{\circ}$ branch.....	74
4-13 Magnitude of RBC flow heterogeneity as a function of magnitude of blood flow heterogeneity for different vessel diameters for a serial tree with	

branches at the same side.....	75
4-14 Comparison of hematocrit heterogeneity for serial and parallel trees	76
4-15 Comparison of hematocrit heterogeneity for serial and parallel trees	76
C-1 The schematic of experiment for a serial bifurcation	121

ABSTRACT

NUMERICAL ANALYSIS FOR BLOOD DISTRIBUTION IN COMPLETE FLOW CROSS-SECTION MICROVASCULAR NETWORKS

by

Jewen Xiao
University of New Hampshire, May, 1997

As the blood flows through a bifurcation, the axisymmetric red blood cell concentration profile is skewed by plasma skimming. In the downstream segment of the bifurcation the concentration profile of red blood cells recovers symmetry by the red blood cell dispersion process.

In this study, the concentration convective equation, which models the red blood cell dispersion process, is solved with the method of finite differences in cylindrical coordinates. In the computation, a shear-induced diffusivity coefficient is used. The computed hematocrit ratios at the second bifurcation are compared with *in vitro* experimental data obtained from 50 μm serial trees with two bifurcations. The variable dispersion model gave the best description of experimental data. The symmetric recovery lengths are computed to compare to branch segment lengths measured *in vivo*. The comparison shows that for 25 μm or above microvascular vessels, the concentration profile most likely remained as asymmetric when the blood reached the next bifurcation.

A new way to measure the quantity of heterogeneity of blood flow in microvascular network based on vector algebra and conservation of mass is proposed. The heterogeneity of red blood cell flow is strongly correlated with the heterogeneity of blood flow. No correlation existed between the heterogeneity of hematocrit and the heterogeneity of blood flow. The influences of departure angle, vessel diameter and branch segment length to the heterogeneity of red blood cell flow were examined. The computational results shows that the heterogeneity of red blood cell in a 3 dimensional microvascular tree network is in the range of the heterogeneity in a 2 dimensional network. The serial tree type of microvascular network has higher heterogeneity of hematocrit and red blood cell flow than the parallel type one.

CHAPTER I

INTRODUCTION

1.1 Introduction

It is generally agreed that William Harvey was the first person to clarify that blood flows in circulatory manner, i.e. the blood passes en route from arteries to veins. Blood circulates to supply oxygen, metabolic fuels, hormones, and vitamins to the organs and individual cells of the body. It also provides a means of removal of metabolic products (such as CO₂, water) from the cells. The blood circulation also serves to maintain a stable temperature within the body under varying external conditions. The vascular system conveys the blood. It consists of a distributing system of arteries and arterioles to the organs and a diffusing system of fine capillaries which are in contact with the cells of the body. The venous system returns the blood, depleted in oxygen, to the heart and lungs.

Blood consists of three types of particles suspended in a continuous medium. The three types of particles are red blood cells(RBC), white blood cells(WBC) and platelets. RBC occupy 97% of the total cell volume of the blood. The volume fraction of red cells in normal human blood—hematocrit—is about 42 to 45% [1]. The continuous medium (plasma) is a complex solution of organic and inorganic salts and organic macromolecules in water. Each of the red blood cells, also called erythrocytes, consists

of a thin, flexible, but essentially unstretchable membrane, and an interior filled with a complex aqueous solution, which is a nearly saturated hemoglobin solution. The resting shape of normal human red cell is a biconcave discoid, with a major diameter of 8.1 microns and a maximum thickness of about 2 microns. The macromolecules in plasma (fibrinogen, globulin, and plasma expanders, *etc.*) cause red cell aggregation. These aggregations contain 6-10 red cells in a stack, called a rouleau. Under shear force, red blood cell undergo a deformation without changing volume or surface area.

Table 1-1 Cells in the blood

Cell	Number (per mm ³)	Unstressed shape and dimensions (μm)	Volume concentration (%) in blood
Erythrocytes	4-6x10 ⁶	Biconcave disc, 8x1-3	45
Leukocytes	4-11x10 ³	Roughly spherical, 7-22	
Platelets	250-500x10 ³	Rounded or oval 2-4	

1.2 Blood and its Rheology

The rheological properties of blood and its constituents play an important role in the physiology of the blood circulation. The rheological complexities of blood and its flow in small vessel systems have posed a serious challenge to researchers through the ages. One and a half centuries ago Poiseuille[2] attempted to quantify the pressure flow relation for blood but his efforts were restricted to fluids much simpler than blood. His very careful and accurate experiments resulted in the establishment of the law governing flow of water, alcohol and mercury in fine circular glass capillaries. The results are summarized by the so called Poiseuille's law :

$$Q = \frac{128 \pi d^4}{\mu L} \Delta P \quad (1-1)$$

The rheology of blood is largely influenced by its particulate nature. Blood plasma is a Newtonian fluid and the normal value of plasma viscosity (μ_p) averages 1.2-1.3 cP at 37°C. The plasma viscosity is primarily a function of the concentration of plasma proteins, especially large proteins with molecular asymmetry, like fibrinogen and some of the globulin fractions.

Results of viscometric measurements, however, demonstrate that normal blood is a non-Newtonian fluid. The apparent viscosity rises with decreasing shear rate. This behavior can be interpreted by red cell aggregation and deformation. In low shear rate range, rouleaux are formed due to red blood cell aggregation. NP in Figure 1-1 is normal human blood having aggregation and deformation. NA is blood without cells aggregation, but cells having the ability to deform. HA is blood having neither aggregation nor deformation. In low shear rate regions, cell aggregation causes the apparent viscosity increase, comparing the curves NP and NA in Figure 1-1. As shear rate increases, aggregates are dispersed and the apparent viscosity decreases. At higher shear rates, red blood cells deform along with streamlines. The apparent viscosity decreases to a constant as shear rate further increases. [3]The apparent viscosity is independent of further increased shear rate. Along with shear rate, hematocrit is another factor which influences the rheology of blood. The apparent viscosity increases as hematocrit increases(see Figure 1-2).

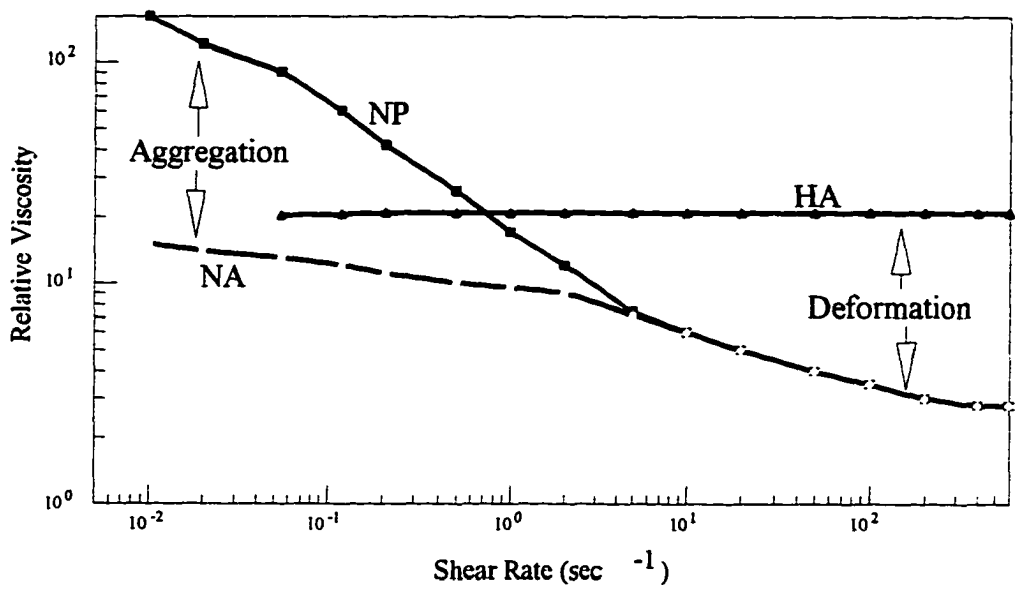


Figure 1-1 The relative viscosity of human blood as a function of shear rate[3], The relative viscosity equals the apparent viscosity divided by the suspending medium viscosity (1.2 mPa*s). NP =normal red blood cells in plasma, NA =normal blood cells in isotonic saline containing 11% albumin (having the same viscosity as plasma), and HA =hardened discoid red blood cells in the same saline.

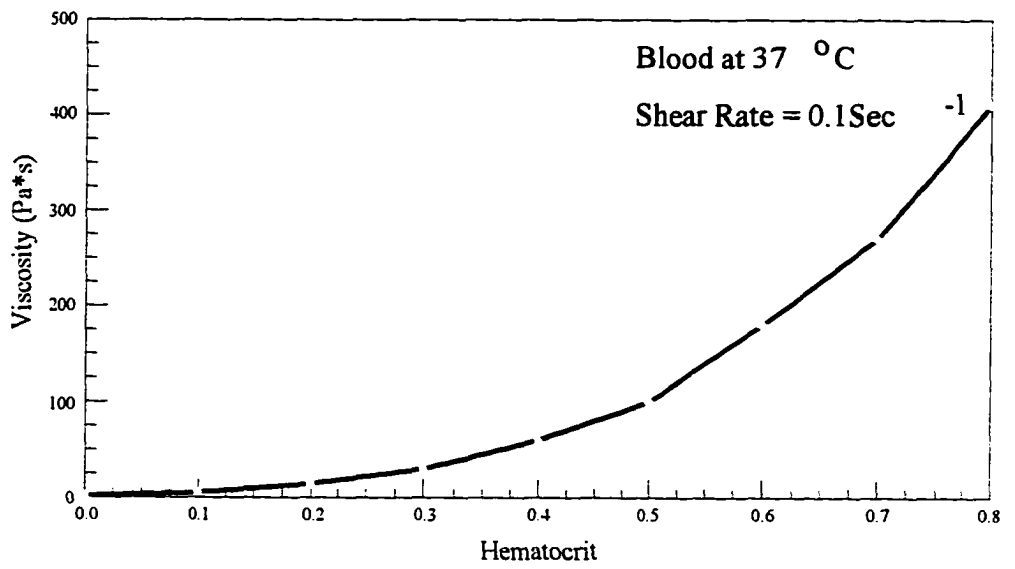


Figure 1-2 The apparent viscosity of human blood as a function of hematocrit

1.3 Definition of Microcirculation

Arterioles, capillaries, and venules are often referred as the microcirculation, or peripheral circulation. The arterioles, capillaries, and venules function as a physiological entity where the exchange of materials between the blood stream and the tissue happens. The capillaries are endothelial tubes, 5 to 10 μm in diameter. Their walls consist of a single layer of flattened endothelial cells, 0.1 to 0.3 μm in thickness. Most of exchange of materials takes place through the capillary wall. Some transfer of water, respiratory gases, and macromolecules also occurs across the wall of terminal segments of arterioles and venules. The terminal arterioles contain smooth muscle and are 10 to 20 μm in diameter. Venules are slightly larger in diameter and with less smooth muscle. Architecture and flow dynamics in the microcirculation are suited to mass transfer.

Table 1-2 Diameters and flow rates in the microcirculation of various species[4]

Property	Arteriole		Capillary		Venule	
	Large	Small	Artery end	Vein end	Small	Large
Diameter(μm)						
Bat wing	19	7	3.7	7.3		
Bat mesentery	70	20	10			
Rat cremaster muscle	80	14	5.5	6.1	24	74
Cat tenissimus muscle	22	10	4.7	5.9	10	40
Length (μm)						
Bat wing	3500	950		450	1000	
Bat mesentery	380	200		130	130	350
Rat cremaster muscle				615	300	
Cat tenissimus muscle	300	100		1000	100	
Number						
Bat wing	12	120		1700	350	25
Bat mesentery	2	9		20	10	2
Velocity (mm/s)						
Bat mesentery	1.0-31.7		0-1.7		0.5-11.1	
Rat cremaster muscle	0.8-12.9		0.2-1.2		0.4-6.6	
Cat tenissimus muscle			0-1.5			

The microcirculation network consists of many bifurcations. Arterioles become smaller during the evolution of the terminal vascular bed. Idealized versions depict the microvascular beds as a series of dichotomous branchings that on the arterial side become successively smaller and terminate by forming a network of endothelial tubes, the capillaries. The venous side is represented as essentially a mirror image except for the greater of the successive confluences of returning blood to the systemic circulation. The diameters of arterioles range from 100 to 10 μm ; by progressive bifurcation it is decreased until at the level of metarterioles in about 30 μm . One single arteriole can provide several metarterioles along its length. The angle at which metarterioles branch off the parent arteriole strongly depends upon the particular vascular bed. In many mesenteric tissues metarterioles have been found to branch off at 30-60 $^\circ$, while in skeletal muscle they often have right branching angle.

Williams and Segal [5] reported the length of unbranched arteriole segments varies widely, from 10 μm to more than 1000 μm in rat soleus muscles. In tissue like skeletal muscle the vascular bed extends into three dimensions. The microcirculation follows a tree-like branching pattern and the capillaries form a complex meshwork, often supplied by several arterioles and drained by several venules. This architecture clearly provides for a great diversity of pathways through the microcirculation. In addition to geometrical parameters such as diameters and lengths of vascular segments, and the branching angles, the knowledge of topological structure is important to understand the microcirculation of a network. The topological structure differs from one network to another. Microvascular network topology can be described by grouping vessels

according to their structural characteristics. Horton introduced centripetal ordering to describe rivers. In centripetal ordering scheme, the most distal branches in the tree are assigned order one. When two vessels of order one converge an order two vessel is formed, two order two vessels form an order three vessel, etc. When vessels of unequal order converge, the higher order is retained. Fenton [6] was among the first to use the centripetal ordering scheme to the microcirculation.

The branching ratio (bifurcation ratio) is defined as the ratio of the number of vessels of a given order to the number of vessels of the next higher order.

$$(R_b)_\alpha = \frac{N_\alpha}{N_{\alpha+1}} \quad (1-2)$$

where N_α is the number of branches of order α and $N_{\alpha+1}$ of order $\alpha+1$, $(R_b)_\alpha$ is the bifurcation ratio of order α . It has been shown that R_b is independent of α . So N_α can be expressed as:

$$N_\alpha = N_1 R_b^{1-\alpha} \quad (1-3)$$

where N_1 is the number of branches of order 1.

A similar relationship can be applied to the average length and diameter of vessels of a given order.

$$L_\alpha = L_1 R_l^{\alpha-1} \quad (1-4)$$

$$D_\alpha = D_1 R_d^{\alpha-1} \quad (1-5)$$

where L_α , D_α are the average length and diameter of a given order α respectively, L_1 , D_1 of first order and R_l , R_d bifurcation ratios for length and diameter. The bifurcation ratios for several microvascular networks have been reported[7].

Table 1-3 Bifurcation ratio for some microvascular networks

Microvascular network	R_b	R_l	R_d
Rabbit omentum			
Arterioles	3.12	1.61	1.30
Venules	2.30	1.56	1.35
Human bulbar conjunctiva			
Arterioles	2.77	1.36	1.26
Venules	2.80	1.41	1.51
Cat sartorius			
Muscle arterioles	3.35	1.86	1.25

1.4 Hemodynamics Microcirculation

The Reynolds number is very low in the microcirculation. Typical Reynolds numbers in 100 μm arterioles are about 0.09 and in a 10 μm capillary, they fall to less than 0.005. It means viscous rather than inertial effects dominate the flow in the microcirculation. Another important parameter in hemodynamics of circulation is Womersley number α . It indicates the extent to which the velocity profile in laminar flow in a long pipe differs from the Poiseuille profile when the fluid is subject to a sinusoidally varying pressure gradient of angular frequency ω . In the microcirculation, α is very small. It approximately ranges from 0.08 in 100 μm vessels to 0.005 in capillaries. This means that in the microcirculation the flow is in phase with the local pressure gradient. It can be considered as quasi-steady. In addition to small Reynolds and Womersley numbers, the wall shear rates in the small vessels are much higher than in the large vessels of systemic circulation. It is of the order of 1000 s^{-1} .

The velocity profile of blood in microcirculation is changed by the presence of cells in blood. Goldsmith[8] measured the velocity profile of emulsions, ghost cell plasma suspensions and found that the particle velocity distribution depends on volume concentrations, particle to tube radius ratio and flow rate. As volume concentration and particle to tube radius ratio increase, the velocity profile changes from parabolic to blunted in the center of the tube. Schmid-Schonbein and Zweifach[9] measured RBC velocity profiles in arterioles and venules of rabbit omentum. They found the velocity profiles are often asymmetric; profiles on the arteriole side are less asymmetric than on the venous side. The vessel diameter has the most influence on the velocity profile. The velocity profile becomes more blunt as the vessel diameter decreases. The shape of velocity profile also depends on the hematocrit. The increase in hematocrit resulted in a more blunt velocity profile. When the maximum velocity is larger than 1.5 mm/sec, the velocity profile is independent of flow rate. Tangelder *et al.* [10] measured red blood cell velocity profile in rabbit mesenteric arterioles (diameter 17-32 μm). They concluded that the velocity profile was blunt compared to the parabolic profile. And the velocity profile became more parabolic as the vessel diameter increased. Baker and Wayland[11] reported that velocity profiles in tubes above 40 μm diameter, hematocrit between 0.06 and 0.60, are almost parabolic at the value of average velocity divided by the vessel diameter above 6 sec^{-1} . Sato and Ohshima[12] used a ten channel dual-sensor method to measure velocity profiles of blood flow at arteriole bifurcation. They found that at about two- diameters downstream length from the bifurcation the velocities of the branches become axisymmetric and blunt. Their results were in conflict with Schmid-Schonbein

and Zweifach's results. This discrepancy may be due to the different experimental measuring techniques.

The interaction of particles in suspensions with a vessel wall cause radial migration. In a diluted suspension, deformable spheres migrate away from the wall toward the tube axis[13]. As the concentration of the suspension increases, particle-particle interaction and near collisions happen, altering the radial migration of RBCs. Furthermore the red cells deform much more than they do in a diluted suspension. The radial migration of cells leads to the nonuniformity of cell concentration across the tube. It is highest in the center of the tube and decreasing sharply in a small layer near the wall that is depleted of cells - the cell free layer (plasma layer). The importance of the plasma layer depends upon hematocrit, shear rate and cell to tube radius ratio. The thickness of the plasma layer increases with decreasing shear rate, decreasing hematocrit and cell to tube radius ratio. It was also found that when the suspending fluid contained dextran, which enhances aggregation of RBCs, the plasma layer width increased. Up to the present there has been no theoretical way to derive the thickness of the plasma layer.

The wall exclusion effect - the impossibility of having cells within one cell radius of the tube wall is one of the mechanisms that cause the existence of the plasma layer. Thomas [14] reported that the thickness of the plasma layer is about 0.71 times the particle radius. Bugliarello and Sevilla [15]found that hematocrit is a major factor which affects the thickness of the plasma layer. It ranges from 4 - 13 μm depending on the hematocrit in 40 - 70 μm diameter glass tubes. Tateishi *et al.* [16] measured the thickness of cell-free layer in microvessels of isolated rabbit mesentery. The thickness of the cell-free layer was reported from 0.5 - 6 μm in microvessels with diameters 5 - 40

μm . The cell free layer increased with microvessel diameter in a saturation manner. Decreasing hematocrit increased the thickness. Published[9, 15] *in vivo* and *in vitro* experimental data suggests that for vessel diameters of 5 - 40 μm , cell-free layer thickness to vessel radius ratio ranges from 0.05 to 0.3, for vessel diameters of 100 - 135 μm , the ratio is between 0.05 and 0.38.

The distribution of red blood cells through the microcirculation plays an important role in oxygen transport and nutrient delivery to tissues. Microvessel hematocrits in several tissues have been measured. The experimental data showed that the average tube and discharge hematocrits gradually decrease through the arterial network and increase through the venous network [17]. Table 1-4 shows the ratio of microvessel hematocrit to systemic hematocrit.

Two important concepts are involved in microvessel hematocrits. 1) Tube hematocrit which is determined by suddenly stopping the flow in a vessel i.e. by freezing and measuring the packed red cell fraction. 2) Discharge hematocrit which is obtained by collecting the effluent of a vessel in a mixing cup and measuring its packed red cell fraction. Hematocrit measurements in whole organs have indicated that microvessel hematocrits are lower than systemic ones.

Table 1-4 The ratio of microvessel hematocrit to systemic hematocrit, H_{MV}/H_{SYS}

Human	H_{MV}/H_{SYS}	Reference
Cerebrum	0.92	[18]
Cranium	0.84	[19]
Cat		
Kidney	0.48	[20]
Tongue	0.84	[21]
Rabbit		
Placenta	0.68	[22]

The mechanisms governing the hematocrit distribution in the microcirculation are not fully understood. Some mechanisms have been proposed. They are the Fahraeus effect, the Fahraeus-Lindqvist effect, the screening effect, the network Fahraeus effect and plasma skimming at bifurcations.

When vessel diameter smaller than 500 μm , the average hematocrit in tube (H_T) is less than the feed hematocrit (H_F) or discharge hematocrit (H_D). This is generally referred to as the Fahraeus effect. This phenomenon can be explained by two factors: (1) the distribution of red blood cells across the vessel lumen is not uniform; (2) the velocity is highest at the center of the vessel and decreases toward zero at the wall. Thus the mean velocity of red cells is higher than the mean velocity of the blood. Consider the plasma layer exists near the wall. The mean residence time of red blood cells is less than that of the plasma. To satisfy the mass conservation, the tube hematocrit H_T should be less than the feed hematocrit H_F or discharge hematocrit H_D . H_T / H_D decreases with decreasing vessel diameter. For single circular vessel blood flow, the value of H_T / H_D is above 0.5. This ratio is a function of the tube hematocrit and the blood velocity.

The fact that the effective viscosity (evaluated from Poiseuille equation) of blood decreases as vessel diameter decreases below about 300 μm is called Fahraeus-Lindqvist effect. This effect could be due to the Fahraeus effect, i.e. the hematocrit decreasing in the vessel causes a lower viscosity of the blood. Barbee and Cokelet [23] proposed that, for vessels greater than 29 μm , the viscosity is equal to the bulk viscosity if the bulk hematocrit is equal to the vessel tube hematocrit.

The screening effect [24] occurs when blood flows into a small vessel. The cells may collide with the entrance edge or other cells, and be retarded, while plasma flows easily into the tube. It is a hydrodynamic effect, which results in a decreased tube hematocrit.

Network Fahraeus effect generalizes the Fahraeus effect to microvessel networks. The phenomenon that the average discharge hematocrit over a complete flow cross-section is less than the feeding hematocrit is called network Fahraeus effect [25]. In any complete flow cross-section conservation of mass is required for total blood flow and red blood cell flow. The network Fahraeus effect is caused by the velocity difference of red cells and blood between the vessels in a complete flow cross-section. The prerequisite for the network Fahraeus effect is a correlation between hematocrit and velocity among the vessel segments of a complete flow cross-section. Pries *et al.* [25] showed that the network Fahraeus effect can account for about 20% of the total hematocrit reduction.

Due to the presence of a plasma layer near the vessel wall, a side vessel branching off a main vessel will contain blood with a higher fraction of plasma than that in the parent vessel. This is because the side vessel gets blood from near the wall in the main vessel where blood cells are in low concentration. This phenomenon is called as “plasma skimming” [26]. Many studies have been made on plasma skimming both *in vivo* and *in vitro*. Krogh [27] observed that the hematocrit in the small side branch is lower than that in the main vessel. Svanes and Zweifach [28] studied plasma skimming at arteriolar bifurcation by using the micro-occlusion technique. They found that the flow

fraction which split into the side branch determines the hematocrit change at the bifurcation. Klitzman and Johnson *et al* [29] used optical opacity as an index of hematocrits in cat mesentery. They found that the hematocrits of side branches depend on the flow fraction in each branch. Schmid - Schonbein *et al.* [30] studied plasma skimming at capillary bifurcations in rabbit ear chambers. They found that cell concentration profile can be characterized by a nonaxisymmetric eccentricity and depends on the blood cell distribution at the upstream entrance to the branch.

Plasma skimming has been studied by conducting *in vitro* experiments. Bugliarello and Hsiao [31] used scaled-up model to simulate plasma skimming at small vessels. They found that plasma skimming at bifurcations was determined by the flow rate of the side branch, particle concentration of the main vessel, and the ratio of side to main vessel radius. The bifurcation angle had no effect on the extent of plasma skimming. Yen and Fung [32] used flexible gelatin disks suspended in silicone oil in their experiments. They noticed that there exists a critical flow rate, above which all of the particles will flow into the branch with the highest velocity. This critical flow rate depends on the feeding particle concentration and the particle to tube diameter ratio. Palmer [33] conducted plasma skimming experiments using 2 dimensional slit bifurcations. He showed that nonuniform red cells distribution existed across the slit. A layer of cell - free (at least deficient) fluid near the vessel wall should cause plasma skimming. Fenton *et al.* [34] used normal and rigid blood cells flowing through 20 to 100 μm bifurcations. They observed that deformability has a negligible effect on plasma skimming. They concluded that three major factors to plasma skimming at bifurcations

are feed hematocrit, tube diameter and flow rate distribution. Carr and Wickham[35] conducted plasma skimming experiments in simple two bifurcation networks. Their findings indicated plasma skimming at an upstream bifurcation can influence the phase separation at downstream bifurcations.

Several mathematical models have been developed to describe the plasma skimming effect at bifurcations. Klitzman and Johnson [36] conducted experiments to study the red cell distribution in hamster cremaster muscle. They correlated their *in vivo* data to a sigmoidal curve represented by a single- parameter logit function,

$$\text{logit } F^* = A \text{ logit } Q^* \quad (1-6)$$

where F^* the ratio of side branch to main vessel red blood cell flux; Q^* the ratio of side branch to main vessel volumetric flow; and $\text{logit } x = \ln[(1-x)/x]$. The single-parameter logit function does not include the effect of critical flow.

Pries *et al.* [37] studied the red blood cell distribution at 65 arteriolar bifurcations in the rat mesentery. They proposed a three-parameter function to take account for the critical flow,

$$\text{logit } F^* = B \text{ logit } \frac{Q^* - X_0}{1 - 2X_0} + A \quad (1-7)$$

where the three unknown parameters A, B, and X_0 should be evaluated for each bifurcation.

Another model of plasma skimming has been developed based on physical grounds. *In vivo* and *in vitro* data for plasma skimming indicated the fractional volumetric flow rate, feeding hematocrit, cell to vessel diameter ratio, and red cell concentration profile in the feeding vessel are important factors. When blood flows

through a microvascular bifurcation, the flow domain in the main vessel is divided into two capture tubes flowing into the distal branches. The separation surface is defined as the three dimensional boundary surface separating those two capture tubes. The separation surface is either flat or a concave arc depending on the ratio of the bifurcation type (T or Y) , the ratio of daughter to parent branch diameters and the Reynolds number of the inlet flow to the bifurcation [38]. The separation surface plays an important role in the red blood cell distribution in downstream of the bifurcation. It has been shown that plasma skimming at a bifurcation can skew the red cell concentration profile in downstream branches. If this asymmetric red cell concentration profile is not completely rearranged when it reaches the next bifurcation, this asymmetric red cell concentration profile will change the plasma skimming of the second bifurcation [35]. The rearrangement process of the skewed red blood cell concentration profile between bifurcations is thought to be due to random collisions among the red cells and depends on the particle diffusivity [39].

1.5 Summary of the Dissertation

The rearrangement process of the skewed red cell concentration profile is considered as a diffusion process. A mathematical model is developed to describe this rearrangement process. The mathematical model is solved by using finite differencing in cylindrical coordinates to obtain red blood cell concentration profile symmetry recovery length. The calculated symmetry recovery lengths are compared to anatomical distances between branch points measured in hamster cremaster muscle. The result will indicate

the need to consider the influence of the upstream bifurcations to plasma skimming of the downstream bifurcations. The mathematical model is then applied to calculate the red blood cell concentrations at each branch outlet in a microvascular network. The effects of topological and geometric parameters of a microvascular network to the hematocrit heterogeneity and the red blood cell flow heterogeneity are studied. The computational results showed that for a 25 μm or larger microvascular vessel the red blood cell concentration profile is most likely not axisymmetric when the blood reached the next bifurcation.

CHAPTER II

MATHEMATICAL MODEL OF PLASMA SKIMMING AT A BIFURCATION AND RBC DISPERSION AT BRANCH SEGMENT

2.1 Introduction

Separation surface, velocity profile and red blood cell concentration profile are three important factors determining the amount of plasma skimming at bifurcations. Fu[40] used the dye tracing technique to determine the shapes of separation surfaces of *in vitro* bifurcations. The flat separation surfaces were obtained when the side branches had similar diameters with the parent vessel. The arc separation surfaces bulging away from the opening of the side branch were got when the side branches had smaller diameters than the parent vessel. The mapping technique was developed to determine how the red blood cells followed the streamline through the bifurcation and shifted into the downstream branch of the bifurcation. The red blood cells can migrate across the streamline in the downstream vessel segment to rearrange the red blood cell concentration profile. This migration process will be modeled as the dispersion process due to random collisions between the red blood cells.

2.2 Velocity and Red Blood Cell Concentration Profiles

Several velocity profiles will be considered in this study. They are the uniform velocity profile, the generalized Poiseuille flow profile, and the two concentric Newtonian phases velocity profile. The two concentric Newtonian phases are cell-rich core phase in the vessel center and cell-free plasma layer near the wall. These velocity profiles can be expressed in the following dimensionless forms:

1). the uniform velocity profile

$$V(\xi) = \frac{v(\xi)}{V_{av}} = 1 \quad 0 < \xi < 1 \quad (2-1)$$

2). the generalized Poiseuille velocity profile

$$V(\xi) = \frac{\omega + 2}{\omega} (1 - \xi^\omega) \quad 0 < \xi < 1 \quad (2-2)$$

If ω is equal to 2, the velocity profile is parabolic. As ω increases the profile becomes more bluni.

3). the two concentric Newtonian phases velocity profile

$$V(\xi) = \begin{cases} \frac{2(1 - \xi^2)}{\phi + (1 - \phi)(1 - \delta)^4} & 1 - \delta < \xi < 1 \\ \frac{2[(1 - \delta)^2 + (1 - (1 - \delta)^2)\phi - \xi^2]}{\phi + (1 - \delta)^4(1 - \phi)} & 0 < \xi < 1 - \delta \end{cases} \quad (2-3)$$

where V_{av} is average velocity, ξ is a dimensionless radial coordinate, δ is a normalized plasma gap width with respect to vessel radius, $=g / R$. ϕ is the ratio of core viscosity to gap viscosity, and ϕ can be found from the correlation suggested by Barbee [41].

$$\phi = \exp\left(\frac{4.2H}{u^{1.2}}\right) \quad (2-4)$$

where H is the hematocrit. u is the average velocity divided by the vessel diameter.

The above velocity profiles can be expressed as:

$$V(\xi) = \alpha(\beta - \xi^m) \quad (2-5)$$

One red blood cell concentration profile examined in this study is uniform profile.

1). uniform concentration profile

$$H(\xi) = \begin{cases} H_c & 0 < \xi < 1 - \delta \\ 0 & 1 - \delta < \xi < 1 \end{cases} \quad (2-6)$$

2.3 The Mapping Technique

Flat and concave arc separation surfaces will be considered in this study. When the side branches have similar diameters with the parent vessel, flat separation surface will be used. When the side branches have smaller diameters than the parent vessel, concave arc The wall exclusion effect prohibits the center of any cell from being located at the wall. That will assume a minimum plasma gap which width is at least one cell radius near the wall. The cells cannot be mapped into plasma gap when using the mapping technique. It means the mapping techniques apply to the core region of the two phase model of blood flow.

When blood flows through a bifurcation, plasma skimming skews the red cell concentration profile downstream of the junction, separation surface will be used. Figure (2-1) shows flat and concave arc separation surfaces. The flat surface can be defined by the perpendicular distance from the separation surface to the vessel center, p.

The Perkkio-Keskinen model [42] will be used in this study for concave arc separation surface. The center of concave arc separation surface is always located at the parent vessel wall. The arc can be determined by the radius of the arc, r .

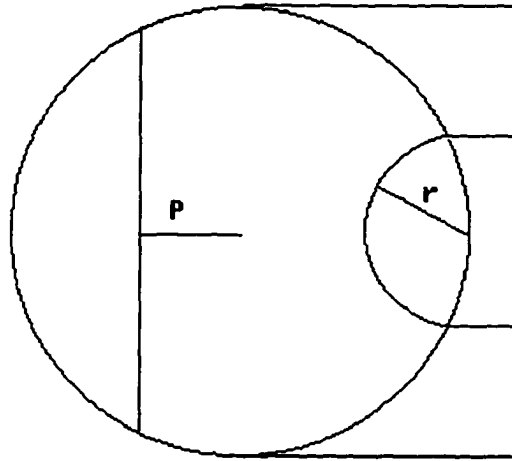


Figure (2-1) Flat or concave arc separation surface

The mapping technique developed by Rong and Carr [43] will be used to compute the shift of the concentration profile across the branch. This technique is based on the principle of mass conservation. It assumed that the fluid elements follow the streamlines across the junctions. In the case of flat separation surface, each fluid element can be located by the intersection of two chords as shown in Figure (2-2).

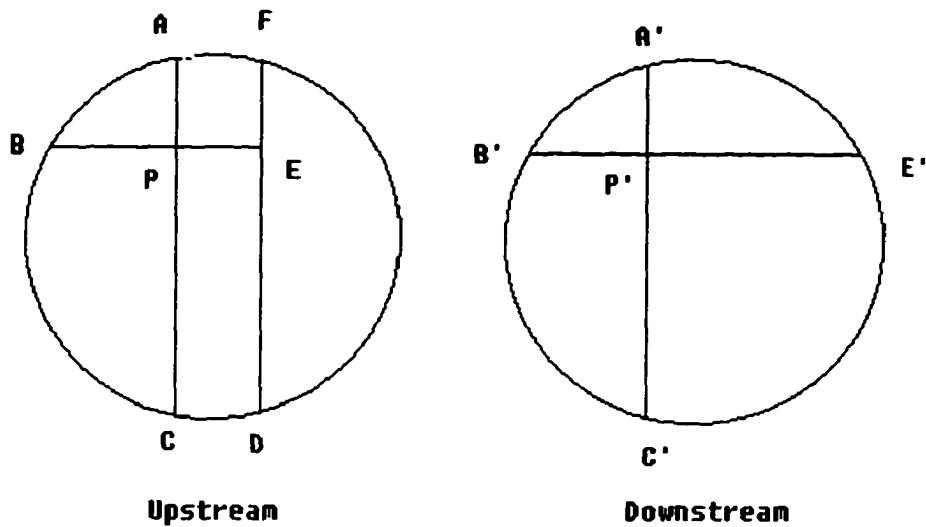


Figure 2-2. The Mapping Technique

In upstream, the fluid element P is described by the chords AC and BE . In downstream, the fluid element P' is described by the chords $A'C'$ and $B'E'$. The principle of mass conservation requires that the flow through area $ABPEF$ upstream matches the flow through area $A'B'P'E'$ downstream. Similarly the flow through area $ABCP$ upstream matches the flow through area $A'B'C'P'$. The location of chord $B'E'$ and $A'C'$ are found by matching the flow in these areas. The result of this mapping technique is almost as good as that obtained by solving the Navier-Stokes equations [44] when comparing with the experimental data of the streamline tracing measurements. The mapping technique can account for the shift of upstream concentration profiles to downstream when they are not uniform.

2.4 The RBC Dispersion Process

The asymmetric red cell concentration profile will regain symmetry due to red cells migration across streamlines. The particle migration across streamlines can occur due to the following reasons:

(1). Tubular pinch effect.

Segre and Silberberg [45] observed that single rigid particles migrate away from the tube wall as well as from the tube center, toward an equilibrium annulus position at high enough particle Reynolds number. This phenomena is induced by inertia force. Goldsmith [8] showed that for deformable drops, even without inertia, there is the possibility of cross streamline migration to the tube axis as the equilibrium position.

(2). Shear-induced particle diffusion in the lateral direction.

Particle migration down a gradient of the shear rate arises when interparticle interactions in a sheared suspension cause suspended particles to experience random fluctuating motion across flow streamlines. A particle moves randomly as it follows along the whole suspension motion. This random motion is due to the chaotic nature of the particle evolution equations in concentrated suspensions. This random motion can give rise to a diffusive behavior. The shear-induced self-diffusivity of non-Brownian rigid particles has been measured experimentally by Eckstein, Bailey and Shapiro [46], and Leighton and Acrivos [47]. From a theoretical standpoint, the mechanism for shear-induced migration has been controversial. Abbott *et al.* [48] attributed it to the existence of forces not described by Stokes equations because it was implicitly assumed that the reversibility of the Stokes flows cannot produce irreversible motion. Leighton and

Acrivos [49] proposed a mechanism to explain the irreversible motion. The small-scale surface roughness of the rigid particles leads to irreversible motion during inter-particle interactions.

In microcirculation, Reynold numbers are much smaller than one. Tubular pinch effect is not likely to account for the cross streamline migration of red cells. Therefore shear induced particle diffusion is assumed to be the mechanism through which the red cell concentration profiles are rearranged.

In this study, the steady-state convective diffusion equation is used to model the rearrangement process of the skewed red cell concentration profile between junctions.

$$\mathbf{v} \cdot \nabla H = \nabla \cdot D \nabla H + \nabla \cdot \mathbf{m} \quad (2-7)$$

where \mathbf{v} is the fully developed velocity profile. H is the cell concentration or hematocrit profile. \mathbf{m} is a fictitious body force, and D is the effective particle dispersion coefficient. The \mathbf{m} is included to account for concentration profiles that are not flat at an infinite distance downstream from the junction. The axisymmetric asymptotic red cell concentration profile can be obtained by solving the following equation:

$$0 = \nabla \cdot D \nabla H + \nabla \cdot \mathbf{m} \quad (2-8)$$

Only constant \mathbf{m} will be considered. Constant \mathbf{m} results in a uniform asymptotic concentration profile. It will eliminate the last term in equation (2-8). If red blood cell motion in sheared blood is considered random, the effective particle dispersion coefficient can be introduced, analogous to the molecular diffusion coefficient.

$$D = \frac{\Delta \bar{R}^2}{2\Delta t} \quad (2-9)$$

where $\Delta \bar{R}^2$ is the mean square displacement, and Δt is the time between observations.

Zydney and Colton [50] proposed a correlation for deformable particle diffusivity in tube flow:

$$D = 0.15a^2\gamma H(1-H)^{0.8} \quad (2-10)$$

where D is the particle diffusivity, a is the particle radius, γ is the shear rate, and H is the hematocrit. The particle diffusivity varies linearly with shear rate. For particles of size $a=1.6-3.5\mu\text{m}$, the above equation gives $D=(1-5)10^{-9}\gamma \text{ cm}^2/\text{sec}$. Thus, $D=2\times 10^{-7}-10^{-6} \text{ cm}^2/\text{sec}$ for $\gamma=200\text{sec}^{-1}$, and $D=2\times 10^{-6}-10^{-5} \text{ cm}^2/\text{sec}$ for $\gamma=2000\text{sec}^{-1}$. In the limit $H=1$ the effective particle dispersion coefficient become zero. This is supported by experimental observations that in packed ghost suspensions tracer red cells undergo no significant lateral migration.

Zydney and Colton[50] assumed that the velocity profile was parabolic in tube flow while developing their correlation. Thus, the particle diffusivity will vary linearly with the tube radius.

$$D = 0.6aV_{av}H(1-H)^{0.8} \quad (2-11)$$

Dimensional analysis shows that the dispersion in the axial direction is negligible.

Equation (2-7) can be expressed in cylindrical coordinates as:

$$V_{av}\alpha\left[\beta-\left(\frac{r}{R}\right)^w\right]\frac{\partial H}{\partial Z} = \frac{1}{r}\frac{\partial}{\partial r}\left(r\cdot D\frac{\partial H}{\partial r}\right) + \frac{1}{r}\frac{\partial}{\partial \theta}\left(D\frac{\partial H}{\partial \theta}\right) \quad (2-12)$$

with boundary conditions:

$$\left\{ \begin{array}{l} H(r, \theta = 0, z) = H(r, \theta = 2\pi, z), \\ \frac{\partial H}{\partial \theta} \Big|_{\theta=0} = \frac{\partial H}{\partial \theta} \Big|_{\theta=2\pi}, \\ H(r = 0, \theta, z) \text{ is finited}, \\ \frac{\partial H}{\partial r} \Big|_{r=R-\delta} = 0. \end{array} \right. \quad (2-13)$$

initial condition: $H = H_0(r, \theta)$. (2-14)

$H_0(r, \theta)$ is determined by the mapping technique.

Equation (2-12), boundary conditions and initial condition are normalized by introducing the dimensionless variables:

$$(\beta - \xi^\omega) \frac{\partial H}{\partial \eta} = \frac{1}{\text{Pe}} \left(\frac{1}{\xi} \frac{\partial}{\partial \xi} \left(\xi^2 \frac{\partial H}{\partial \xi} \right) + \frac{1}{\xi} \frac{\partial^2 H}{\partial \theta^2} \right) \quad (2-15)$$

The normalized boundary conditions are:

$$\left\{ \begin{array}{l} H(\xi, \theta = 0, \eta) = H(\xi, \theta = 2\pi, \eta), \\ \frac{\partial H}{\partial \theta} \Big|_{\theta=0} = \frac{\partial H}{\partial \theta} \Big|_{\theta=2\pi}, \\ H(\xi = 0, \theta, \eta) \text{ is finited}, \\ \frac{\partial H}{\partial \xi} \Big|_{\xi=1-\delta} = 0. \end{array} \right. \quad (2-16)$$

The normalized initial condition: $H = H_0(\xi, \theta)$. (2-17)

Where ξ is the dimensionless radial coordinate, $\xi = \frac{r}{R}$, and $0 < \xi < 1 - \delta$; η is the dimensionless axial coordinate, $\eta = \frac{z}{R}$, and $\eta > 0$; θ is the angular coordinate and $0 < \theta < 2\pi$; δ is the dimensionless plasma layer width, $\delta = \frac{g}{R}$.

The Peclet number, Pe, is defined as:

$$\text{Pe} = \alpha \left(\frac{R}{a} \right)^2 \frac{1}{0.6H(1-H)^{0.8}} \quad (2-18)$$

The finite differencing method is used to solve equation (2-15). The tube center ($\xi=0$) is singular to equation (2-15). To eliminate the singular point, L'Hopital's rule was used to take the limit of each term of equation(2-15) as ξ goes to zero[51]. This gives the new equation for the centerline ($\xi = 0$):

$$\left\{ \beta \frac{\partial H}{\partial \eta} = \frac{1}{\text{Pe}} \left(2 \frac{\partial H}{\partial \xi} + \frac{\partial}{\partial \xi} \frac{\partial^2 H}{\partial \theta^2} \right), \right. \quad (2-19)$$

at $\xi=0$.

The alternating-direction-implicit (ADI) method [52] was used.

At $\xi=0$,

$$\frac{H_{1,j}^{k+\frac{1}{2}} - H_{1,j}^k}{\frac{\Delta \eta}{2}} = \frac{1}{\beta \text{Pe}} \left(2 \cdot \frac{H_{2,j}^k - H_{1,j}^k}{\Delta \xi} + \frac{H_{2,j+1}^k + H_{2,j-1}^k - 2H_{2,j}^k}{\Delta \xi (\Delta \theta)^2} \right) \quad (2-20)$$

for r direction, where $j=0, \text{NJ}-1$ and

$$\frac{H_{1,j}^{k+1} - H_{1,j}^{k+\frac{1}{2}}}{\frac{\Delta \eta}{2}} = \frac{1}{\beta \text{Pe}} \left(2 \cdot \frac{H_{2,j}^{k+\frac{1}{2}} - H_{1,j}^{k+\frac{1}{2}}}{\Delta \xi} + \frac{H_{2,j+1}^{k+\frac{1}{2}} + H_{2,j-1}^{k+\frac{1}{2}} - 2H_{2,j}^{k+\frac{1}{2}}}{\Delta \xi (\Delta \theta)^2} \right) \quad (2-21)$$

for θ direction,

For $\xi \neq 0$,

$$(\beta - \xi^\omega) \frac{\partial H}{\partial \eta} = \frac{1}{\text{Pe}} \left(\frac{1}{\xi} \frac{\partial}{\partial \xi} \xi^2 \frac{\partial H}{\partial \xi} + \frac{1}{\xi} \frac{\partial^2 H}{\partial \theta^2} \right) = \frac{1}{\text{Pe}} \left(2 \frac{\partial H}{\partial \xi} + \xi \frac{\partial^2 H}{\partial \xi^2} + \frac{1}{\xi} \frac{\partial^2 H}{\partial \theta^2} \right) \quad (2-22)$$

in radial direction:

$$(\beta - \xi_i^\omega) \frac{H_{i,j}^{k+\frac{1}{2}} - H_{i,j}^k}{\frac{\Delta\eta}{2}} = \frac{1}{\text{Pe}} \left[\xi_i \frac{H_{i-1,j}^{k+\frac{1}{2}} - 2H_{i,j}^{k+\frac{1}{2}} + H_{i+1,j}^{k+\frac{1}{2}}}{(\Delta\xi)^2} + 2 \frac{H_{i+1,j}^{k+\frac{1}{2}} - H_{i-1,j}^{k+\frac{1}{2}}}{2\Delta\xi} + \frac{1}{\xi_i} \frac{H_{i,j+1}^k - 2H_{i,j}^k + H_{i,j-1}^k}{(\Delta\theta)^2} \right] \quad (2-23)$$

in angular direction:

$$(\beta - \xi_i^\omega) \frac{H_{i,j}^{k+1} - H_{i,j}^{k+\frac{1}{2}}}{\frac{\Delta\eta}{2}} = \frac{1}{\text{Pe}} \left[\xi_i \frac{H_{i-1,j}^{k+\frac{1}{2}} - 2H_{i,j}^{k+\frac{1}{2}} + H_{i+1,j}^{k+\frac{1}{2}}}{(\Delta\xi)^2} + 2 \frac{H_{i+1,j}^{k+\frac{1}{2}} - H_{i-1,j}^{k+\frac{1}{2}}}{2\Delta\xi} + \frac{1}{\xi_i} \frac{H_{i,j-1}^{k+1} - 2H_{i,j}^{k+1} + H_{i,j+1}^{k+1}}{(\Delta\theta)^2} \right] \quad (2-24)$$

Where $\xi_i = (i-1)\Delta\xi$, and i, j, k are indices in ξ -, θ -, η -directions respectively.

Indices scheme is shown in Figure 2-3 for discretization in ξ -, θ - directions.

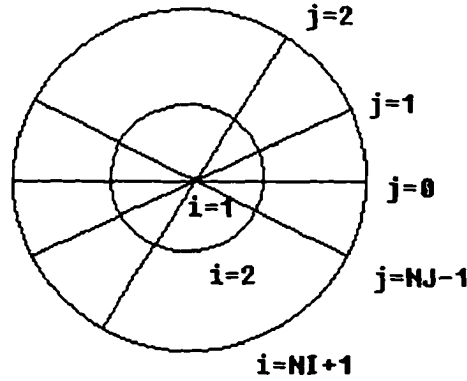


Figure 2-3. Indices Scheme

Combining the similar terms the equations become, in radial direction:

$$\begin{aligned} H_{i-1,j}^{k+\frac{1}{2}} \left[\frac{1}{\Delta\xi} - \frac{\xi_i}{(\Delta\xi)^2} \right] + H_{i,j}^{k+\frac{1}{2}} \left[\frac{\xi_i}{(\Delta\xi)^2} + \frac{2\text{Pe}(\beta - \xi_i^\omega)}{\Delta\eta} \right] - H_{i+1,j}^{k+\frac{1}{2}} \left[\frac{\xi_i}{(\Delta\xi)^2} + \frac{1}{\Delta\xi} \right] \\ = \frac{H_{i,j+1}^k - 2H_{i,j}^k + H_{i,j-1}^k}{\xi_i (\Delta\theta)^2} + H_{i,j}^k \frac{2\text{Pe}(\beta - \xi_i^\omega)}{\Delta\eta} \end{aligned} \quad (2-25)$$

$$\begin{cases} i = 2, NI + 1 \\ j = 0, NJ - 1 \end{cases}$$

in angular direction:

$$\begin{aligned} & H_{i,j-1}^{k+1} \left[\frac{-1}{\xi_i (\Delta\theta)^2} \right] + H_{i,j}^{k+1} \left[\frac{2}{\xi_i (\Delta\theta)^2} + \frac{2Pe(\beta - \xi_i^\omega)}{\Delta\eta} \right] - H_{i,j+1}^{k+1} \left[\frac{1}{\xi_i (\Delta\theta)^2} \right] \\ &= \frac{\xi_i}{(\Delta\xi)^2} \left[H_{i-1,j}^{k+\frac{1}{2}} - 2H_{i,j}^{k+\frac{1}{2}} + H_{i+1,j}^{k+\frac{1}{2}} \right] + \frac{1}{\Delta\xi} \left(H_{i+1,j}^{k+\frac{1}{2}} - H_{i-1,j}^{k+\frac{1}{2}} \right) + H_{i,j}^{k+\frac{1}{2}} \frac{2Pe(\beta - \xi_i^\omega)}{\Delta\eta} \end{aligned} \quad (2-26)$$

$$\begin{cases} i = 2, NI + 1 \\ j = 0, NJ - 1 \end{cases}$$

The boundary condition, $\left. \frac{\partial H}{\partial \xi} \right|_{\xi=1-\delta} = 0$ becomes:

$$H_{NI+2,j} = H_{NI,j} \quad (2-27)$$

Substituting the above equation into equations (2-25) and (2-26) gives:

radial direction

$$\begin{aligned} & H_{NI,j}^{k+\frac{1}{2}} \left[\frac{-2\xi_{NI+1}}{(\Delta\xi)^2} \right] + H_{NI+1,j}^{k+\frac{1}{2}} \left[\frac{2\xi_{NI+1}}{(\Delta\xi)^2} + \frac{2Pe(\beta - \xi_{NI+1}^\omega)}{\Delta\eta} \right] \\ &= \frac{H_{NI+1,j-1}^k - 2H_{NI+1,j}^k + H_{NI+1,j+1}^k}{\xi_{NI+1} (\Delta\theta)^2} + H_{NI+1,j}^k \frac{2Pe(\beta - \xi_{NI+1}^\omega)}{\Delta\eta} \end{aligned} \quad (2-28)$$

angular direction

$$\begin{aligned} & H_{NI+1,j-1}^{k+1} \left[\frac{-1}{\xi_{NI+1} (\Delta\theta)^2} \right] + H_{NI+1,j}^{k+1} \left[\frac{2}{\xi_{NI+1} (\Delta\theta)^2} + \frac{2Pe(\beta - \xi_{NI+1}^\omega)}{\Delta\eta} \right] - H_{NI+1,j+1}^{k+1} \left[\frac{1}{\xi_{NI+1} (\Delta\theta)^2} \right] \\ &= \frac{2\xi_{NI+1}}{(\Delta\xi)^2} \left[H_{NI,j}^{k+\frac{1}{2}} - H_{NI+1,j}^{k+\frac{1}{2}} \right] + H_{NI+1,j}^{k+\frac{1}{2}} \frac{2Pe(\beta - \xi_{NI+1}^\omega)}{\Delta\eta} \end{aligned} \quad (2-29)$$

Where $j = 0, 1, 2, \dots, NJ-1$.

Periodic boundary condition $H(\xi, \theta = 0, \eta) = H(\xi, \theta = 2\pi, \eta)$ gives:

$$H_{i,0} = H_{i,NJ}, \quad H_{i,-1} = H_{i,NJ-1} \quad (2-30)$$

for radial direction:

$j = 0$:

$$\begin{aligned} & H_{i-1,0}^{k+\frac{1}{2}} \left[\frac{2}{\Delta\xi} - \frac{\xi_i}{(\Delta\xi)^2} \right] + H_{i,0}^{k+\frac{1}{2}} \left[\frac{2}{(\Delta\xi)^2} + \frac{2Pe(\beta - \xi_i^\omega)}{\Delta\eta} \right] - H_{i+1,0}^{k+\frac{1}{2}} \left[\frac{\xi_i}{(\Delta\xi)^2} + \frac{2}{\Delta\xi} \right] \\ &= \frac{H_{i,1}^k - 2H_{i,0}^k + H_{i,NJ-1}^k}{\xi_i(\Delta\theta)^2} + H_{i,0}^k \frac{2Pe(\beta - \xi_i^\omega)}{\Delta\eta} \end{aligned} \quad (2-31)$$

($i = 2, 3, \dots, NI+1$).

$j = NJ-1$:

$$\begin{aligned} & H_{i-1,NJ-1}^{k+\frac{1}{2}} \left[\frac{2}{\Delta\xi} - \frac{\xi_i}{(\Delta\xi)^2} \right] + H_{i,NJ-1}^{k+\frac{1}{2}} \left[\frac{2}{(\Delta\xi)^2} + \frac{2Pe(\beta - \xi_i^\omega)}{\Delta\eta} \right] - H_{i+1,NJ-1}^{k+\frac{1}{2}} \left[\frac{\xi_i}{(\Delta\xi)^2} + \frac{2}{\Delta\xi} \right] \\ &= \frac{H_{i,0}^k - 2H_{i,NJ-1}^k + H_{i,NJ-2}^k}{\xi_i(\Delta\theta)^2} + H_{i,NJ-1}^k \frac{2Pe(\beta - \xi_i^\omega)}{\Delta\eta} \end{aligned} \quad (2-32)$$

($i = 2, 3, \dots, NI+1$).

for angular direction:

$j = 0$:

$$\begin{aligned}
& H_{i,Nj-1}^{k+1} \left[\frac{-1}{\xi_i (\Delta\theta)^2} \right] + H_{i,0}^{k+1} \left[\frac{2}{\xi_i (\Delta\theta)^2} + \frac{2Pe(\beta - \xi_i^w)}{\Delta\eta} \right] + H_{i,1}^{k+1} \left[\frac{-1}{\xi_i (\Delta\theta)^2} \right] \\
& = \frac{\xi_i}{(\Delta\xi)^2} \left[H_{i-1,0}^{k+\frac{1}{2}} - 2H_{i,0}^{k+\frac{1}{2}} + H_{i+1,0}^{k+\frac{1}{2}} \right] + \frac{2}{\Delta\xi} \left(H_{i+1,0}^{k+\frac{1}{2}} - H_{i-1,0}^{k+\frac{1}{2}} \right) + H_{i,0}^{k+\frac{1}{2}} \frac{2Pe(\beta - \xi_{NI+1}^w)}{\Delta\eta}
\end{aligned} \tag{2-33}$$

(i = 2, 3,, NI + 1).

j = NJ-1:

$$\begin{aligned}
& H_{i,Nj-2}^{k+1} \left[\frac{-1}{\xi_i (\Delta\theta)^2} \right] + H_{i,Nj-1}^{k+1} \left[\frac{2}{\xi_i (\Delta\theta)^2} + \frac{2Pe(\beta - \xi_i^w)}{\Delta\eta} \right] + H_{i,0}^{k+1} \left[\frac{-1}{\xi_i (\Delta\theta)^2} \right] \\
& = \frac{\xi_i}{(\Delta\xi)^2} \left[H_{i-1,Nj-1}^{k+\frac{1}{2}} - 2H_{i,Nj-1}^{k+\frac{1}{2}} + H_{i+1,Nj-1}^{k+\frac{1}{2}} \right] + \frac{2}{\Delta\xi} \left(H_{i+1,Nj-1}^{k+\frac{1}{2}} - H_{i-1,Nj-1}^{k+\frac{1}{2}} \right) + H_{i,Nj-1}^{k+\frac{1}{2}} \frac{2Pe(\beta - \xi_i^w)}{\Delta\eta}
\end{aligned} \tag{2-34}$$

(i = 2, 3,, NI + 1).

Let i = 2 in equation (2-25) to obtain:

$$\begin{aligned}
& H_{2,j}^{k+\frac{1}{2}} \left[\frac{2\xi_{2i}}{(\Delta\xi)^2} + \frac{2Pe(\beta - \xi_{2i}^w)}{\Delta\eta} \right] - H_{3,j}^{k+\frac{1}{2}} \left[\frac{\xi_2}{(\Delta\xi)^2} + \frac{1}{\Delta\xi} \right] \\
& = \frac{H_{2,j+1}^k - 2H_{2,j}^k + H_{2,j-1}^k}{\xi_2 (\Delta\theta)^2} + H_{2,j}^k \frac{2Pe(\beta - \xi_2^w)}{\Delta\eta} + H_{1,j}^{k+\frac{1}{2}} \left[\frac{1}{\Delta\xi} - \frac{\xi_2}{(\Delta\xi)^2} \right]
\end{aligned} \tag{2-35}$$

$H_{1,j}^{k+\frac{1}{2}}$ in the above equation can be obtained from equation (2-20).

If we assign the notation $A_1(i)$, $A_2(i)$, and $A_3(i)$ to the coefficients corresponding to unknown variables $H_{i-1,j}^{k+\frac{1}{2}}$, $H_{i,j}^{k+\frac{1}{2}}$, $H_{i+1,j}^{k+\frac{1}{2}}$ respectively in equations (2-25), (2-28) and (2-34), and we assign the notation $B(i,j)$ to the right hand side of

equations (2-25), (2-28) and (2-34). The linear equations can be expressed in a matrix form as follows:

$$\begin{bmatrix} A_2(2) & A_3(2) & 0 & \dots & \dots & \dots \\ A_1(3) & A_2(3) & A_3(3) & 0 & \dots & \dots \\ 0 & A_1(4) & A_2(4) & A_3(4) & 0 & \dots \\ \vdots & 0 & & & & \vdots \\ \vdots & & & \ddots & & \vdots \\ & & & & 0 & \vdots \\ & \dots & 0 & A_1(NI) & A_2(NI) & A_3(NI) \\ & \dots & \dots & 0 & A_1(NI+1) & A_2(NI+1) \end{bmatrix} \begin{bmatrix} H_{2,j}^{k+\frac{1}{2}} \\ H_{3,j}^{k+\frac{1}{2}} \\ H_{4,j}^{k+\frac{1}{2}} \\ \vdots \\ \vdots \\ H_{NI,j}^{k+\frac{1}{2}} \\ H_{NI+1,j}^{k+\frac{1}{2}} \end{bmatrix} = \begin{bmatrix} B(2,j) \\ B(3,j) \\ B(4,j) \\ \vdots \\ \vdots \\ B(NI,j) \\ B(NI+1,j) \end{bmatrix} \quad (2-36)$$

When $j = 0$, or $NJ-1$, equation (2-31) and (2-32) were used to account for periodic boundary condition.

The Computed $H_{i-1,j}^{k+\frac{1}{2}}$, $H_{i,j}^{k+\frac{1}{2}}$ are substituted into equation (2-26) to solve for $H_{i,j-1}^{k+1}$, $H_{i,j}^{k+1}$, $H_{i,j+1}^{k+1}$. Similarly $A_1'(j)$, $A_2'(j)$, $A_3'(j)$ and $B'(i,j)$ denote the coefficients in equations (2-26), (2-27)

$$\begin{bmatrix} A_1'(1) & A_2'(1) & 0 & \dots & \dots & A_3'(1) \\ A_1'(2) & A_2'(2) & A_3'(2) & 0 & \dots & 0 \\ 0 & A_1'(3) & A_2'(3) & A_3'(3) & 0 & \vdots \\ \vdots & 0 & & & & \vdots \\ \vdots & & & \ddots & & \vdots \\ & & & & 0 & \vdots \\ 0 & \dots & 0 & A_1'(NI-2) & A_2'(NI-2) & A_3'(NI-2) \\ A_1'(NI-1) & 0 & \dots & 0 & A_2'(NI-1) & A_3'(NI-1) \end{bmatrix} \begin{bmatrix} H_{i,2}^{k+1} \\ H_{i,3}^{k+1} \\ H_{i,4}^{k+1} \\ \vdots \\ \vdots \\ \vdots \\ H_{i,NJ-2}^{k+1} \\ H_{i,NJ-1}^{k+1} \end{bmatrix} = \begin{bmatrix} B'(i,2) \\ B'(i,3) \\ B'(i,4) \\ \vdots \\ \vdots \\ \vdots \\ B'(i,NJ-2) \\ B'(i,NJ-1) \end{bmatrix} \quad (2-37)$$

In finite differencing equations, moving a full step in η - direction will require the solution of two systems of linear algebraic equations. Solving systems of linear equation

in radial direction will move the first half step. The second half step is moved by solving the systems of linear equation in angular direction. The matrix in radial direction is a tridiagonal matrix. It can be solved by simple eliminations and back substitutions. The matrix in angular direction is a symmetric matrix. One typical FORTRAN program used is listed in Appendix A. The ADI method is unconditionally stable in rectangular coordinates, but this is not true in cylindrical coordinates. It becomes unstable as $\Delta\eta$ increases. By trial and error the solution is found to be stable when $\Delta\eta$ is less than 0.05. The numerical solution was checked by comparing to an analytical solution using the following initial condition

$$H(\xi, \theta, \eta = 0) = \begin{cases} 1, & 0 < \theta < \pi/2 \\ 0, & \pi/2 < \theta < 3\pi/2 \\ 1, & 3\pi/2 < \theta < 2\pi \end{cases} \quad (2-38)$$

The analytical solution can be obtained using separation of variables and the method of Frobenius.

$$H(\xi, \theta, \eta) = \sum_{n=0}^{\infty} \sum_{m=0}^{\infty} \exp\left(-\lambda_{mn}^2 \frac{\eta}{Pe}\right) \sum_{p=0}^{\infty} R_{mnp} \left(\frac{\xi}{1-\delta}\right)^{p + \frac{\sqrt{1+4m^2}-1}{2}} \left[A_{mn} \cos(m\theta) + B_{mn} \sin(m\theta) \right] \quad (2-39)$$

The constant R_{mnp} is computed as follows:

$$R_{mnp} = \begin{cases} 1 & p = 0 \\ \frac{-\beta \lambda_{mn}^2 (1-\delta)^2 R_{mnp-1}}{p(p + \sqrt{1+4m^2})} & 1 \leq p \leq \omega \\ \frac{\lambda_{mn}^2 (1-\delta)^2 [(1-\delta)^\omega R_{mnp-\omega-1} - \beta R_{mnp-1}]}{p(p + \sqrt{1+4m^2})} & \omega + 1 \leq p \end{cases} \quad (2-40)$$

The eigen values λ_{mn} are found from the boundary condition:

$$\left. \frac{\partial H}{\partial \xi} \right|_{\xi=1-\delta} = 0. \quad (2-41)$$

The constants A_{mn} and B_{mn} are found from Sturm Liouville theory.

Figure 2-4 and 2-5 show the absolute difference between the analytical solution and numerical calculation obtained by the method of finite difference for the red blood cell concentration. The absolute differences decrease as the solution distance moves to further downstream. At 500 diameter downstream position the absolute differences are less than 0.003.

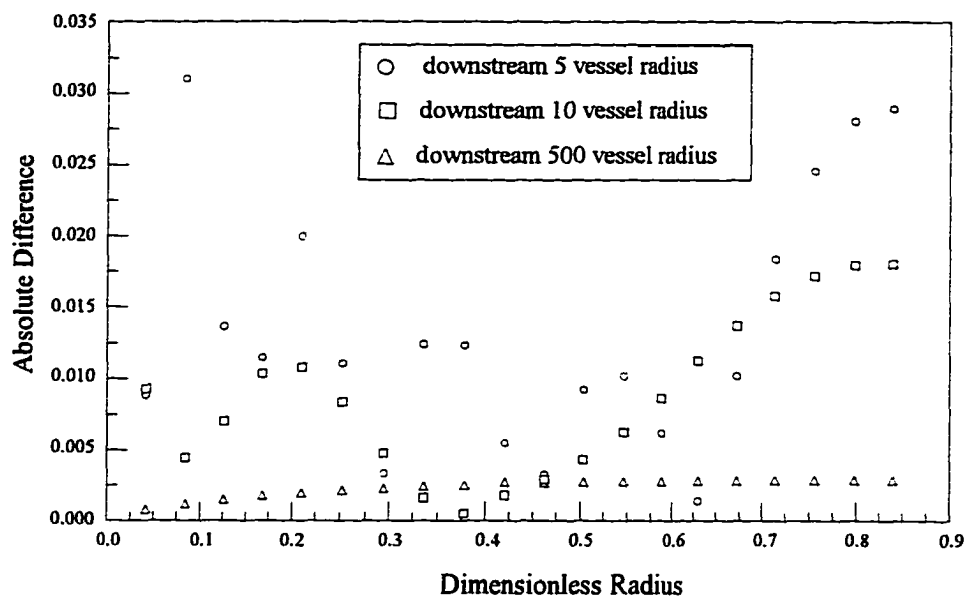


Figure 2-4 Absolute difference between analytical solution and numerical calculation for different dimensionless radii at the angle 54°

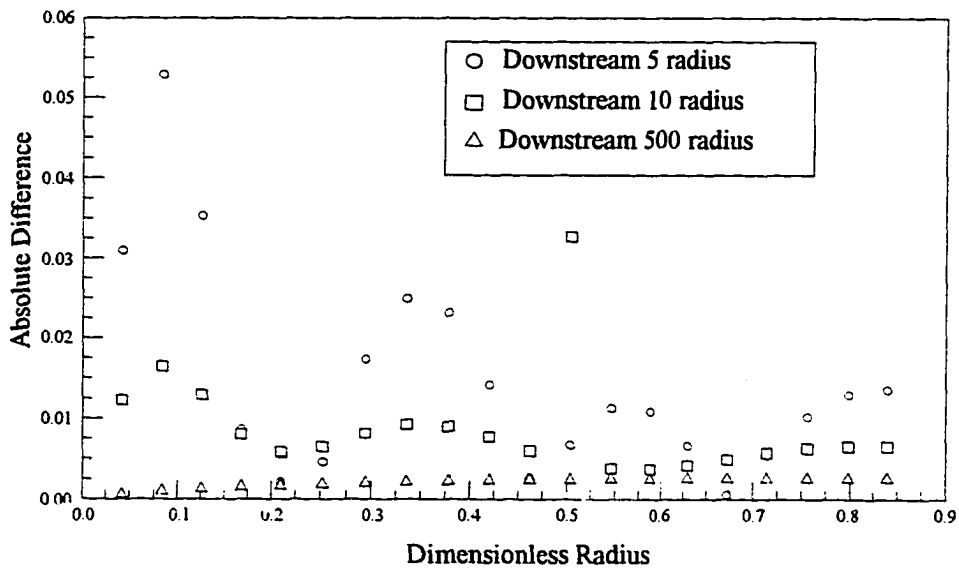


Figure 2-5 Absolute difference between analytical solution and numerical calculation for different dimensionless radii at the angle 126°

A red blood cell flow mass balance check was conducted to make sure the finite differencing calculation does not lose any red blood cell mass. The total red blood cell mass at any cross section of the tube is computed by numerical integration.

$$F_{RBC} = \int_0^{2\pi} \int_0^{1-\delta} H(\xi, \theta, \eta) (\beta - \xi^w) \xi d\xi d\theta. \quad (2-42)$$

$H(\xi, \theta, \eta)$ is calculated by the ADI finite difference method. The results (Table 2-1) shows that the loss of red blood cell mass by the ADI finite difference method is less than 0.01%.

Table 2-1 The total red blood cell mass of various distances downstream of the bifurcation

η	0.05	5	10	400	500
F_{RBC}	1.26189552	1.26189562	1.26189571	1.2618923	1.2618914

The stability of the ADI finite difference program was tested by varying mesh sizes in radial and angular directions. The change of the mesh size in angular directions has little effect on the stability of the program. Forty-eight nodes in both radial and angular directions have given satisfactory results.

2.5 Comparison of Numerical Solution to Experimental Data

The computational results were compared to the *in vitro* experimental data in serial bifurcations. These data were obtained in a straight tube with two bifurcations located in opposite sides of the parent branch as shown in Figure 2-5. Both straight tube and side branches had the same diameter, 50 μ m.

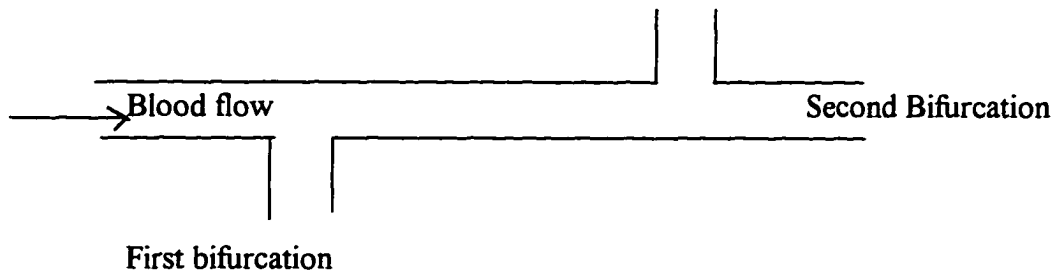


Figure 2-6. Schematic of a serial bifurcation

The distances between two bifurcations range from 0.08 mm to 12.0 mm. The variables used to report experimental data are Q_1^* , the volumetric flow fraction into first bifurcation; Q_2^* , the volumetric flow fraction in the second bifurcation; $(F_2^*)_{exp}$, the red blood cell flux fraction into the second bifurcation. The computational results, $(F_2^*)_{cal}$, were obtained by running the computer program. In the computer program the flat separation surfaces were used because all of the branches have the same diameters. The experimentally measured Q_1^* , Q_2^* were used as inputs in the program to calculate the location of the separation surface in each bifurcation. There exist several possible models to account for the dispersion process of red blood cells between junctions. The mathematical model for cell dispersion in this study is called the variable dispersion model. The constant dispersion model was considered in a previous dissertation[40]. The difference between these two models is that in the constant dispersion model the diffusivity is evaluated as a global constant and independent of local shear rate; in variable dispersion model, the diffusivity varies linearly with local shear rate. Both models assumed that the dispersion process of red blood cells between junctions has impacts on the plasma skimming of downstream bifurcation. Two other models are also

considered in this study. One assumes the dispersion process of red blood cells is rapid, the skewed concentration profile after each bifurcation will always recover axisymmetry before the blood reaches next junction downstream. This model is called the symmetric profile model. The other model considered that the radial diffusivity of red blood cells in the microvasculature is very small. Goldsmith [8] recorded the radial position of tracer red blood cells with time in ghost cell suspensions. He calculated the dispersion coefficient ranged from 3×10^{-8} cm²/sec near the tube axis to 1.5×10^{-7} cm²/sec near the tube wall. So the change of red blood cell concentration profile along the axis of any vessel in the microcirculation could be small, perhaps even negligible. This model is called the no dispersion model. The computational results, $(F_2^*)_{cal}$ of variable dispersion model, constant dispersion model, symmetric profile model and no dispersion model were compared to the experimental measured $(F_2^*)_{exp}$ in effort to determine which model best describes the experimental data. The best model is the one which gives the smallest sum of the squares of residuals between $(F_2^*)_{exp}$ and $(F_2^*)_{cal}$, and the residuals have a normal distribution. Fu [40] has shown that the flat red blood cell concentration profile has a smaller sum of the squares of residuals than the parabolic concentration profile. In this study only flat red cell concentration profile is considered.

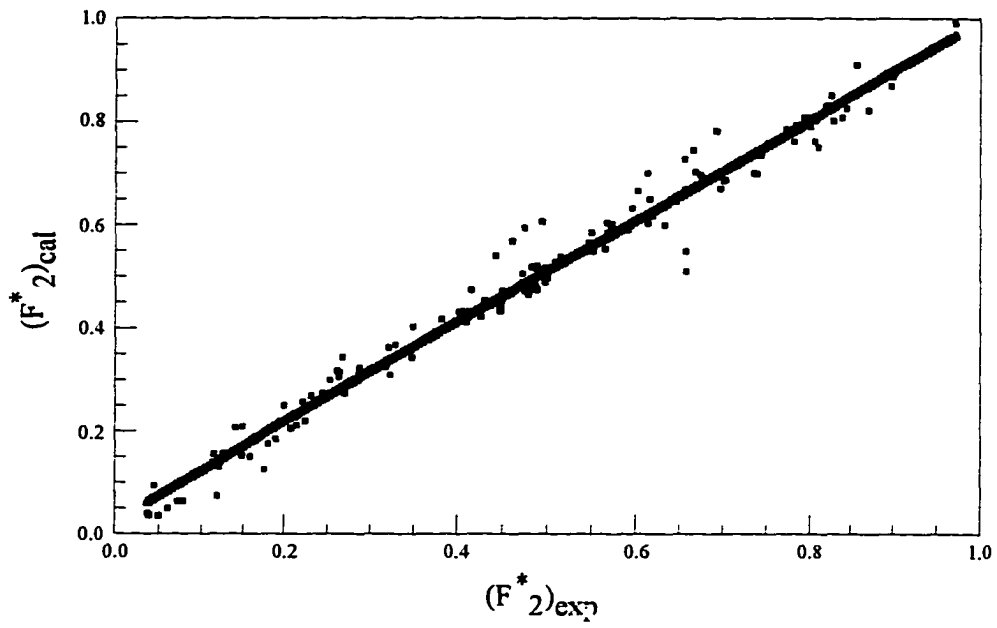


Figure 2-7. The parity plot for velocity profile $\omega = 2$ model

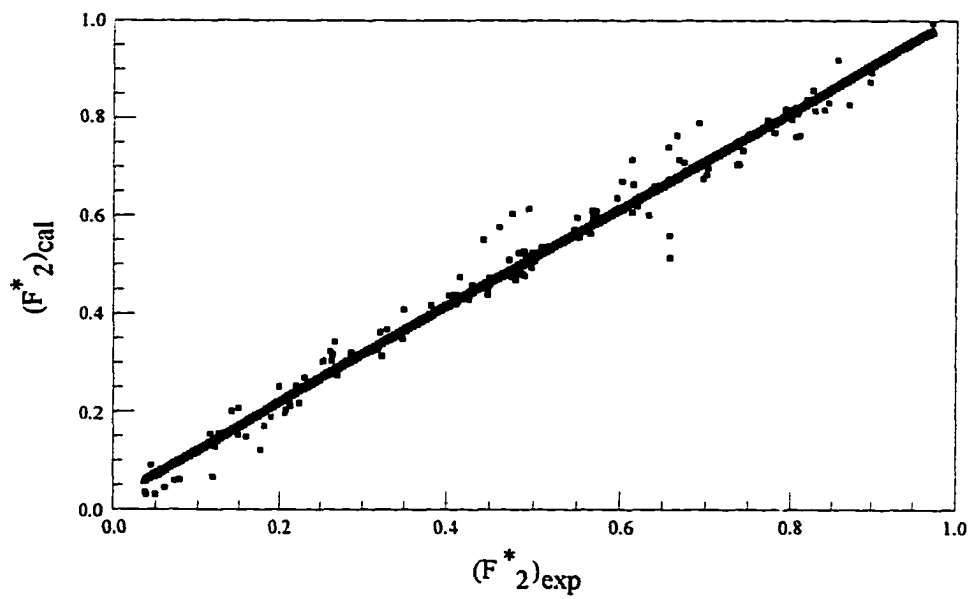


Figure 2-8. The parity plot for velocity profile $\omega = 4$ model

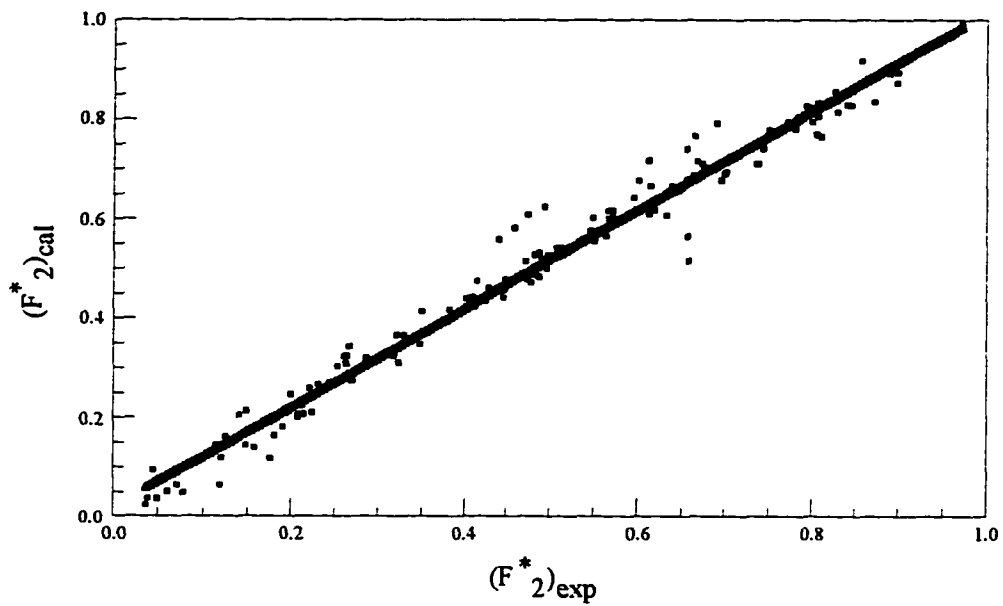


Figure 2-9. The parity plot for velocity profile $\omega=6$ model

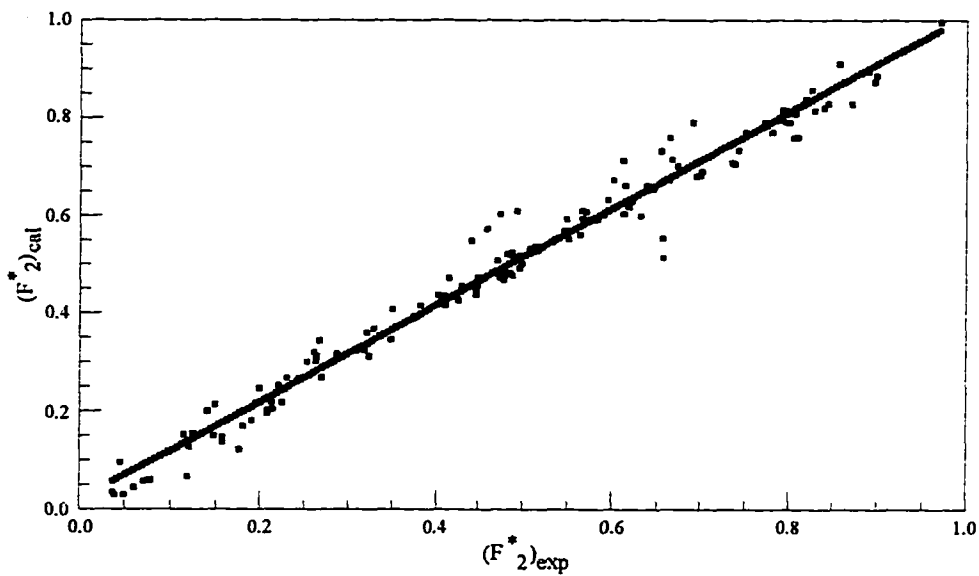


Figure 2-10. The parity plot for constant dispersion model

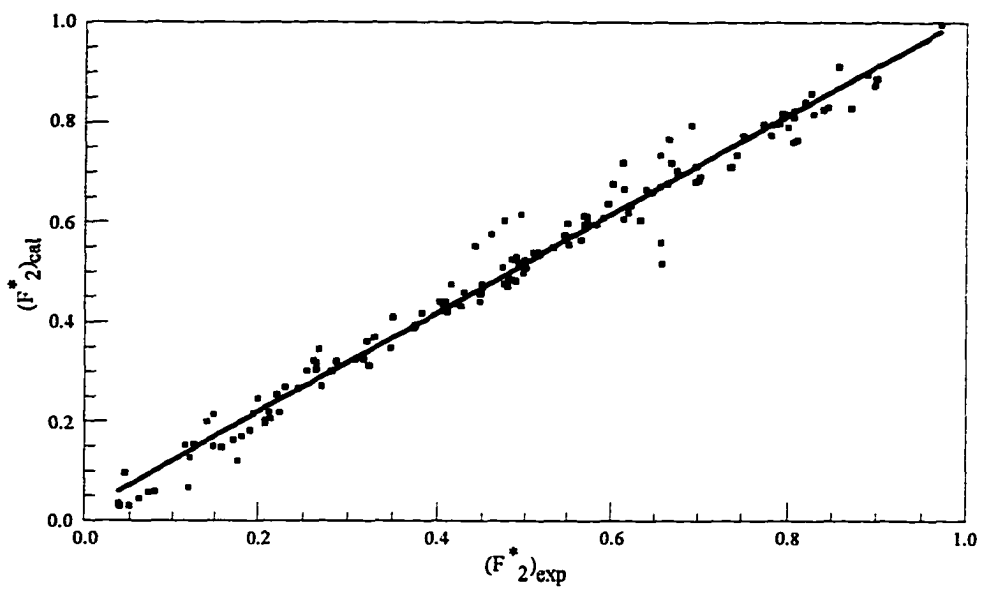


Figure 2-11. The parity plot for variable dispersion model

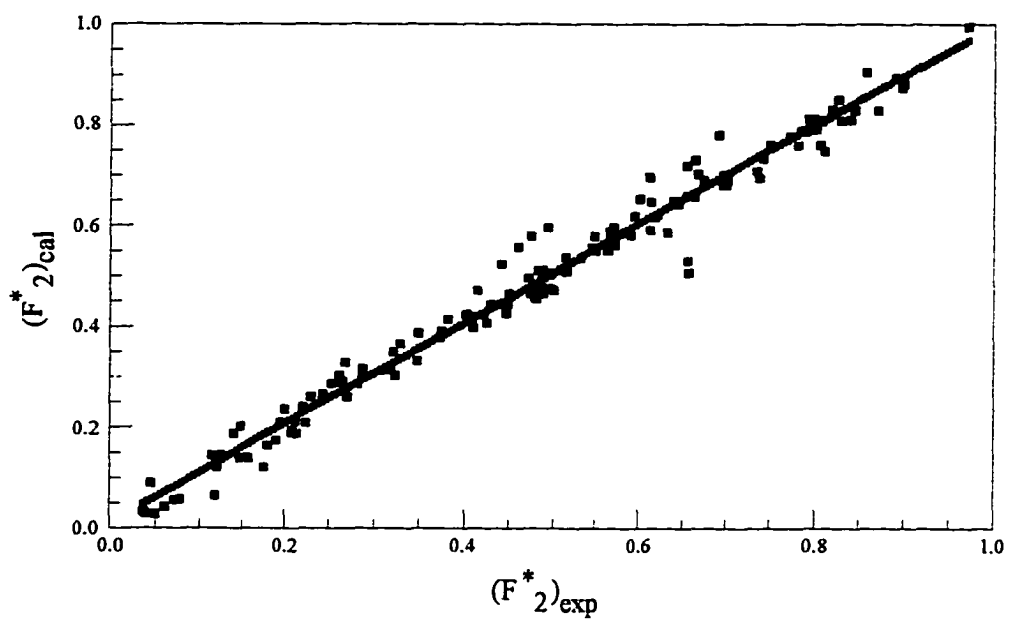


Figure 2-12. The parity plot for symmetric profile model

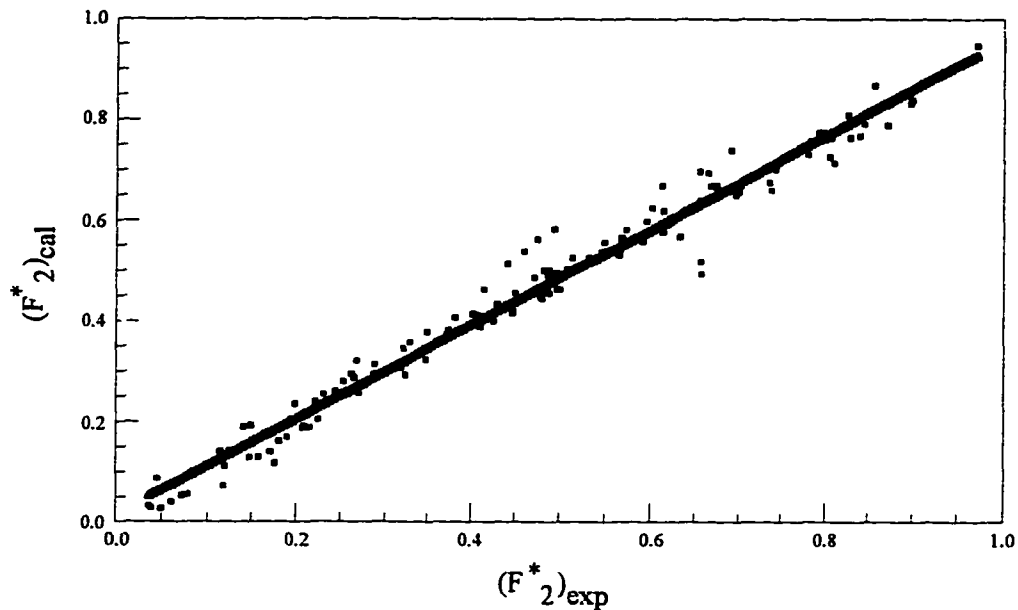


Figure 2-13. The parity plot for no RBC dispersion model

To find out which velocity profile gives the best description of experimental data, $(F_2^*)_{cal}$ were plotted against $(F_2^*)_{exp}$. Table 2-2 shows the results of the curves for different velocity profiles. As the value of ω increases, the slopes of the curves are closer to 1. That means the blunt velocity profile has better description of experimental data than the parabolic velocity profile ($\omega=2$). This result agreed with *in vivo* measurement of red blood cell velocity profiles. The two-phase velocity profile gave almost the same description result as the case of $\omega=6$ velocity profile. But the two-phase velocity profile depends on hematocrit, $\omega=6$ velocity profile does not depend on hematocrit. When hematocrit in microvascular network changes much, the two-phase velocity profile is expected to give the best description. As a result, only the two-phase velocity profile is considered in the rest of the study.

Table 2-2 The linear regression results for different velocity profiles

Model	Parity line	Sum of squares of deviations
Two-phase velocity profile	$(F_2^*)_{cal}=0.9889(F_2^*)_{exp}+0.0222$	0.19556
$\omega=2$ velocity profile	$(F_2^*)_{cal}=0.9710(F_2^*)_{exp}+0.0265$	0.17915
$\omega=4$ velocity profile	$(F_2^*)_{cal}=0.9847(F_2^*)_{exp}+0.0239$	0.19345
$\omega=6$ velocity profile	$(F_2^*)_{cal}=0.9924(F_2^*)_{exp}+0.0229$	0.20270

Once the two-phase velocity profile was chosen, the different dispersion models (variable dispersion, constant dispersion, symmetric profile and no RBC dispersion) were compared to select the model which best describes the experimental data. Again, $(F_2^*)_{cal}$ computed from various models were plotted against $(F_2^*)_{exp}$. The results of these plots were shown in Table 2-3.

Table 2-3. The linear regression results for different dispersion models

Model	Parity line	Sum of squares of deviations
Variation dispersion	$(F_2^*)_{cal}=0.9889(F_2^*)_{exp}+0.0222$	0.19556
No RBC dispersion	$(F_2^*)_{cal}=0.9652(F_2^*)_{exp}+0.0199$	0.16460
Symmetric profile	$(F_2^*)_{cal}=0.9862(F_2^*)_{exp}+0.0112$	0.17325
Constant dispersion	$(F_2^*)_{cal}=0.9886(F_2^*)_{exp}+0.0192$	0.19896

From Table 2-3 the slope of parity line for no red blood cell dispersion model has the biggest difference from one. It means that no red blood cell dispersion model is not the best model to describe the experimental data. This model can be eliminated from further consideration. The other three models have no obvious difference. But the constant dispersion model needed a smaller step in computation to avoid numerical instability. So it was also not considered in the rest of this study.

Notice that as η increases the red blood cell concentration from the variable dispersion model will become axisymmetric. This is the concept of symmetry recovery

length discussed later. It means that no difference between the variable dispersion model and symmetric model in describing the experimental data with large η . It is necessary to select the experimental data for which the downstream branch segment distances are less than the symmetry recovery length defined in the next chapter. Table 2-4 showed the comparison result of the variable dispersion model and symmetric model with the “short distance” experimental data.

Table 2-4. The linear regression results for variable dispersion and symmetric profile models

Model	Parity Line Equation	Sum of squares of deviations
Variable Dispersion	$(F^*_2)_{cal}=0.968(F^*_2)_{exp}+0.0369$	0.0403
Symmetric Profile	$(F^*_2)_{cal}=0.952(F^*_2)_{exp}+0.021$	0.0389

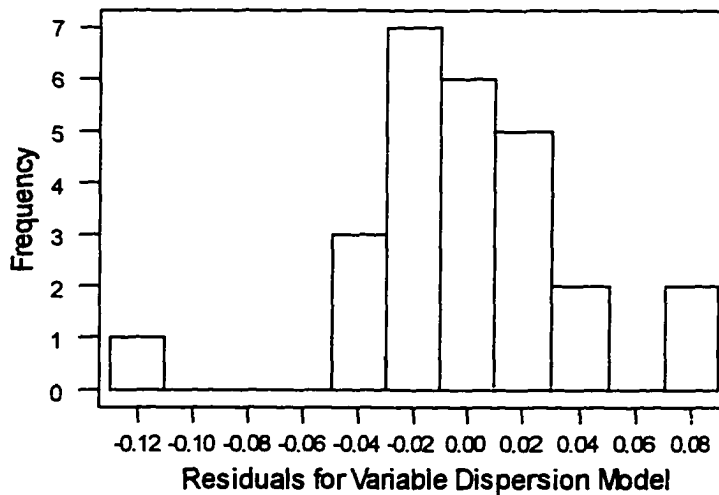


Figure 2-14. Residual histogram for variable dispersion model.

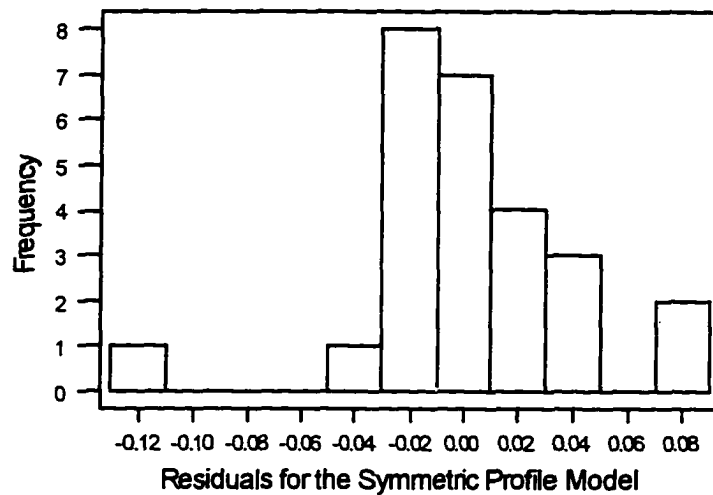


Figure 2-15. Residual histogram for symmetric profile model.

Figure 2-14 and Figure 2-15 showed the residual histograms for variable dispersion model and symmetric profile model, respectively. An Anderson-Darling test[53] for normality showed that the residuals for the variable dispersion model were normal distribution ($p=0.061$), but the residuals for the symmetric profile model were not normal distribution ($p=0.032$). The level of significance for this test is 0.05. Because the least squares regression assumes that the resulting residuals are normal distribution, the variable dispersion model is superior to the symmetric profile model in describing the experimental data.

The variable dispersion model with the two-phase velocity profile and a flat asymptotic red blood cell concentration profile gave the best description of the experimental data of plasma skimming in serial bifurcations.

CHAPTER III

THE SYMMETRIC RECOVERY LENGTH

3.1 The Calculation of the Symmetric Recovery Length

In the last chapter, a flat red blood cell concentration profile, with the two-phase velocity profile and variable dispersion model gave the best description of experimental plasma skimming data. It means that the dispersion process of red blood cells between bifurcations has an significant effect on the plasma skimming on the downstream bifurcation. But if the distance between two bifurcations is long enough, the red blood cell concentration profile will eventually become axisymmetric due to radial diffusion. The knowledge of the distance between bifurcations in that red cell concentration profile turns axisymmetric will allow us to establish more accurate mathematical models for microcirculation. The symmetric recovery length is defined as the distance downstream from the bifurcation at which the maximum absolute deviation of computed F_{2C}^* from the symmetric profile F_{sym}^* is less than 0.02 for all possible values of Q_1^* , i.e.

$$\max |F_{2C}^* - F_{sym}^*| < 0.02. \quad (3-1)$$

Obviously, the symmetric recovery length is a function of both Q_1^* , the volumetric flow fraction into the first bifurcation, and the plasma layer width, δ . The value of Q_1^* will determine the magnitude of the shift in the concentration profile over

the bifurcation. The larger value of Q_1^* causes the concentration profile more skewed. It needs a longer distance for the concentration profile becomes axisymmetric. The size of the plasma layer width δ , also influences the magnitude of the shift of the concentration profile. For smaller δ , the concentration profile only shifts very slightly away from the symmetric profile even for a large Q_1^* , and the symmetric length will be short. When δ is near one, which means the red blood cells only occupy very small portion of the center of the vessel, the red blood cells cannot be shifted very far away from the center of the vessel because of the presence of the vessel wall. The vessel wall will exert a strong exclusion effect on the red blood cells. That forces the red blood cells shift back to the center of the vessel soon. Then the symmetric recovery length should not be long. It can be expected that between these extreme situations there exists a maximum recovery length.

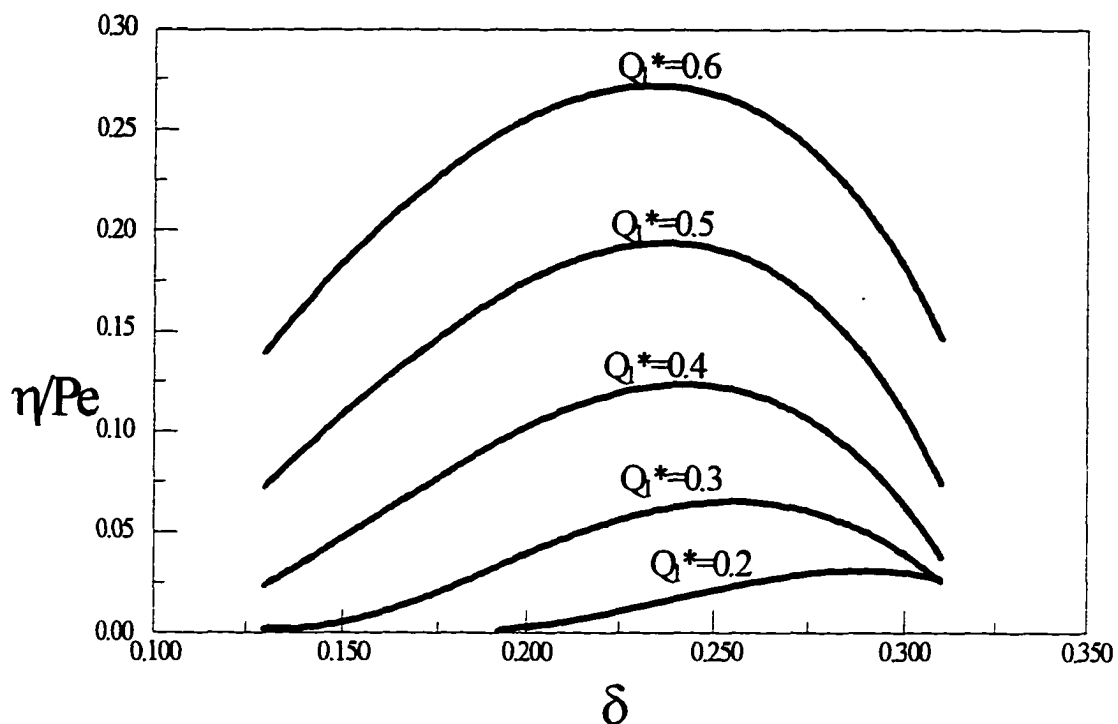


Figure 3-1. Dimensionless symmetry recovery length for flat separation surface

Figure 3-1 shows the dimensionless symmetric recovery length, η/Pe , as a function of Q_1^* and δ . The flat separation surface was used in the computation. The maximum of symmetric recovery length locates in the value of δ between 0.23 to 0.25. When δ is larger than 0.3, the symmetric recovery length decreases quickly. As stated in the introduction, the value of δ ranges from 0.05 to 0.38 from *in vivo* and *in vitro* experimental data. That suggests the maximum of symmetric recovery length can happen in *in vivo* condition.

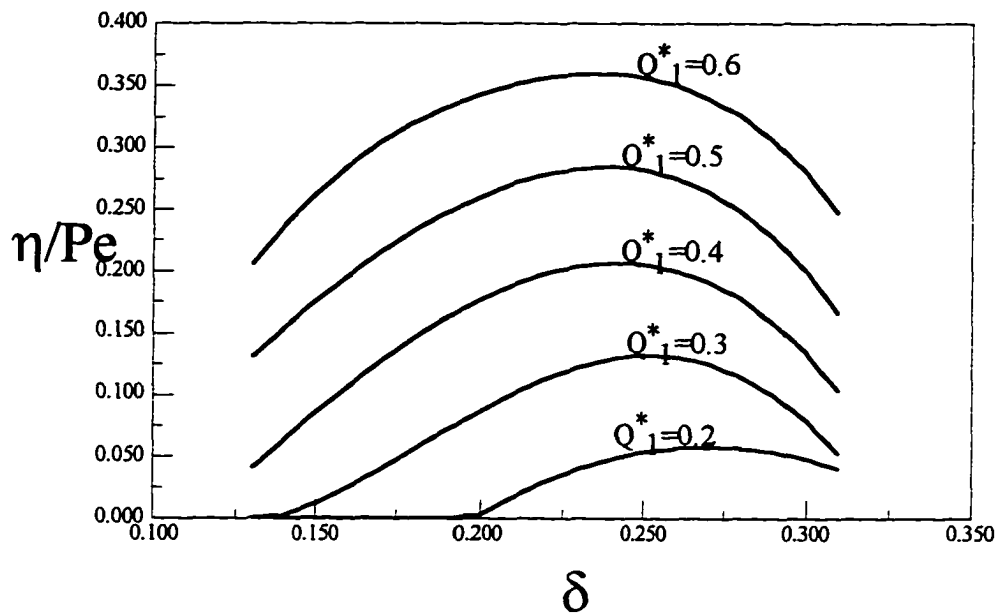


Figure 3-2. Dimensionless symmetry recovery length for curved separation surface

Figure 3-2 shows the dimensionless symmetric recovery length for curved separation surface. The curved separation surface expressed the plasma skimming in the branches which have different diameters. The Perkkio and Keskinen's [42] model is used to describe the curved separation surface plasma skimming. A maximum of symmetric recovery length locates in the value of δ between 0.25 to 0.27. For the same Q_1^* , the magnitude of symmetric recovery length for curved separation surface is larger than one for flat separation surface.

It is helpful to translate the dimensionless result into a dimensional result in order to compare the symmetry recovery length to the experimental data. Carr [54] estimated the plasma gap width from plasma skimming experimental data for branches with

diameters ranging from 20 to 100 μm . A plasma gap width was suggested to correlate the experimental data. Here the same width of a plasma gap (4 μm) is assumed:

$$g = 4 \mu\text{m} \quad (3-2)$$

The dimensionless plasma gap width is converted into the expression of vessel diameter.

$$\delta = g / R_t \quad \Rightarrow \quad R_t = 4 / \delta \quad (3-3)$$

The dimensionless segment distance is changed into the downstream distance.

$$\eta = Z / R_t \quad \Rightarrow \quad Z = \eta R_t = \eta \cdot 4 / \delta = \text{Pe} (\eta / \text{Pe}) \cdot 4 / \delta \quad (3-4)$$

$$\text{where } \text{Pe} = \alpha (R_t / R_c)^2 \{ 1 / [0.6H (1-H)^{0.8}] \} \quad (3-5)$$

From the two concentric Newtonian phases velocity profile, α is:

$$\alpha = \frac{2}{\phi + (1 - \delta)(1 - \phi)} \quad (3-6)$$

In equation 3-5, R_c is the radius of red blood cell (= 4 μm). H is hematocrit. Its value is assumed to be 0.45. In equation 3-6, ϕ is the ratio of core to gap viscosity determined by equation 2-4.

$$\phi = \exp (4.2H / u^{1.2}) \quad (2-4)$$

u is the average velocity divided by the tube diameter.

$$U = V_{av} / d_t \quad (3-7)$$

The value of α depends on the averaged velocity V_{av} .

Figure 3-3 shows the results for $V_{av} = 1000 \mu\text{m} / \text{sec}$. (light curves) and $V_{av} = 30000 \mu\text{m} / \text{sec}$. (dark curves) for flat separation surface.

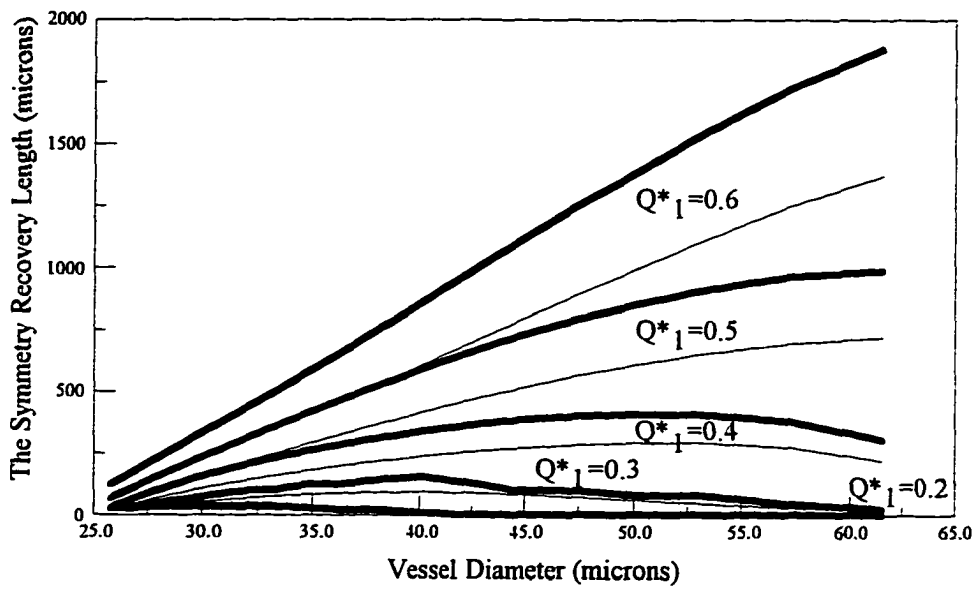


Figure 3-3. Dimensional symmetry recovery length for flat separation surface

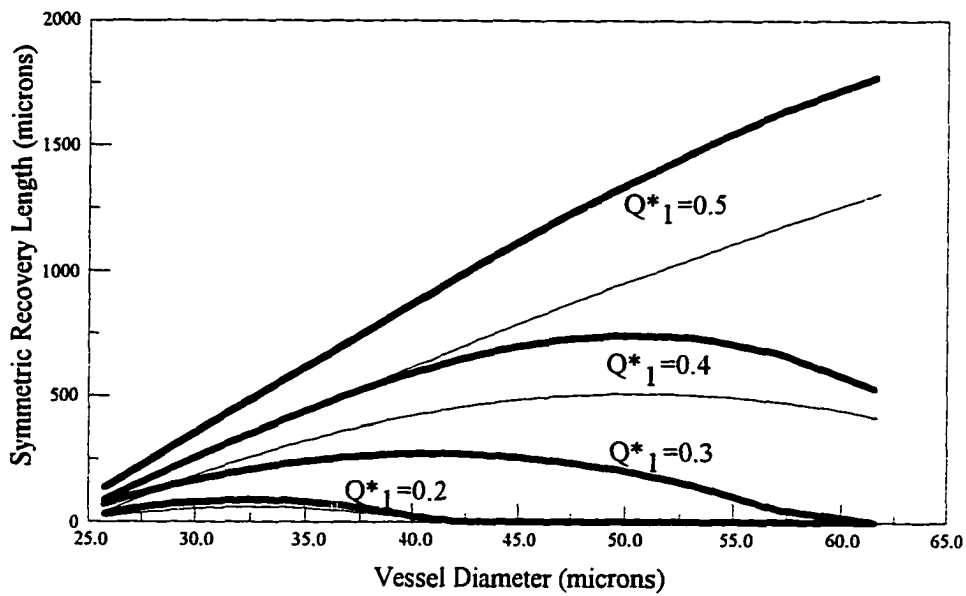


Figure 3-4. Dimensional symmetry recovery length for curved separation surface

Figure 3-4 shows the results for curved separation surface. The lower average velocity results in a blunter velocity profile produces in a shorter symmetry recovery length.

The dimensional symmetry recovery length increases as the volumetric flow fraction Q_1^* increases for a given tube diameter. It can be explained as follows. As the volumetric flow fraction increases, the streamlines bend more, the red blood cells follow the streamlines through the bifurcation, the red blood cell concentration profile shifts in a greater extent. Then the symmetry recovery length is longer.

For a constant volumetric flow fraction Q_1^* , the dimensional symmetry recovery length increases with the tube diameter, reaches a maximum value, then decreases with the tube diameter. This phenomena can be explained as follows. In a very small tube, the red blood cells cannot be shifted very far away from the tube centerline because of the tube geometry. Then the red blood cell concentration profile gets very slightly skewed and is almost symmetric, the symmetric recovery length is short. As the tube diameters increase, the red blood cell concentration profile gets more skewed. But in a big diameter tube, the plasma gap is relatively small. A relative small plasma gap width means the inlet red blood cell concentration profile is almost uniform across the entire section of the tube. After the bifurcation the concentration profile still remains nearly uniform. It needs a shorter distance to get back to an axisymmetric red blood cell concentration profile. Again a shorter symmetry recovery length results. Between these two extreme situations, there is a maximum in the symmetry recovery length. The maximum value depends on the volumetric flow fraction and the tube diameter.

3.2 Comparison to *In Vivo* Experimental Data

One of the purposes in this study is to answer the following questions. Is it necessary to consider the influence of asymmetry of the concentration profile after the first bifurcation on the plasma skimming at the second bifurcation? Or is the concentration profile symmetric when it gets to the second bifurcation? To answer the questions, we need to compare the calculated symmetry recovery lengths to experimentally measured lengths between bifurcations in microvascular network. Frame and Sarelius [55] reported anatomical data on microvascular tree structures in hamster cremaster muscles. Frame [56] provided us with raw data on 68 different arteriolar bifurcations. Sarelius [57] measured red blood cell velocity at branches of microvascular trees which have the same structure as those reported in reference [55]. The diameters of feeding vessels reported by Sarelius [57] ranged from 24 to 43 μm .

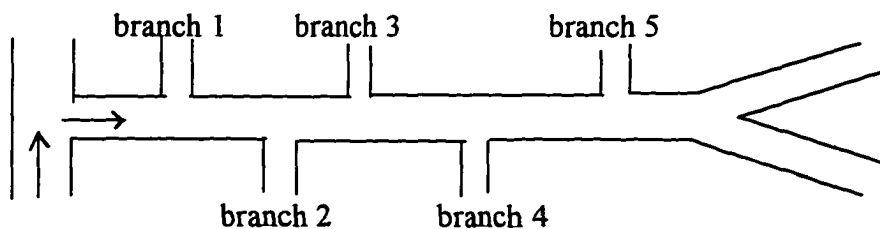


Figure 3-5. Schematic of a microvascular tree structure in Hamster cremaster muscles (provided by Frame [55]).

Table 3-1. The range of volumetric flow fraction from Sarelius's [54] data

	Control vessels	Dilated vessels with O_2	Constricted vessels with Adenosine
Q^* at branch 2	0.24	0.38	0.28
Q^* at branch 3	0.39	0.34	0.15

Table 3-1 shows the volumetric flow fraction Q^* estimated from Sarelius's [57] data. The average volumetric flow fraction Q^* is 0.29, with a range of 0.15 ~ 0.39. Figure 3-6 and 3-7 showed the *in vivo* lengths and computed recovery lengths when average velocity is 30, 1000 $\mu\text{m}/\text{sec}$, respectively. When $Q_1^*=0.2$, concentration profile asymmetries occur between vessel diameters of 25 and 41 μm . If the vessel diameter is larger than 41 μm , the concentration profile becomes symmetric when the blood reaches the second bifurcation. But for vessel diameters between 27 and 41 μm , the concentration profile is asymmetric when the blood arrives the second bifurcation for all of bifurcations. When the average velocity is 1000 $\mu\text{m}/\text{sec}$, 67% of the bifurcations in the experimental data set are affected by concentration profile asymmetries. When average velocity is 30 $\mu\text{m}/\text{sec}$, 72% of the bifurcations in experimental group are influenced by concentration profile asymmetries.

When $Q_1^*=0.3$, concentration profile asymmetries occur between vessel diameters of 25 and 61 μm . If the vessel diameter is larger than 61 μm the concentration profile become symmetric again when the blood reached the second bifurcation. But for vessel diameters between 25 and 61 μm , the concentration profile is still asymmetric when the blood flow into the second bifurcation for all of bifurcations. When average velocity is 1000 or 30 $\mu\text{m}/\text{sec}$, all of bifurcations in the experimental data set are affected by concentration profile asymmetries.

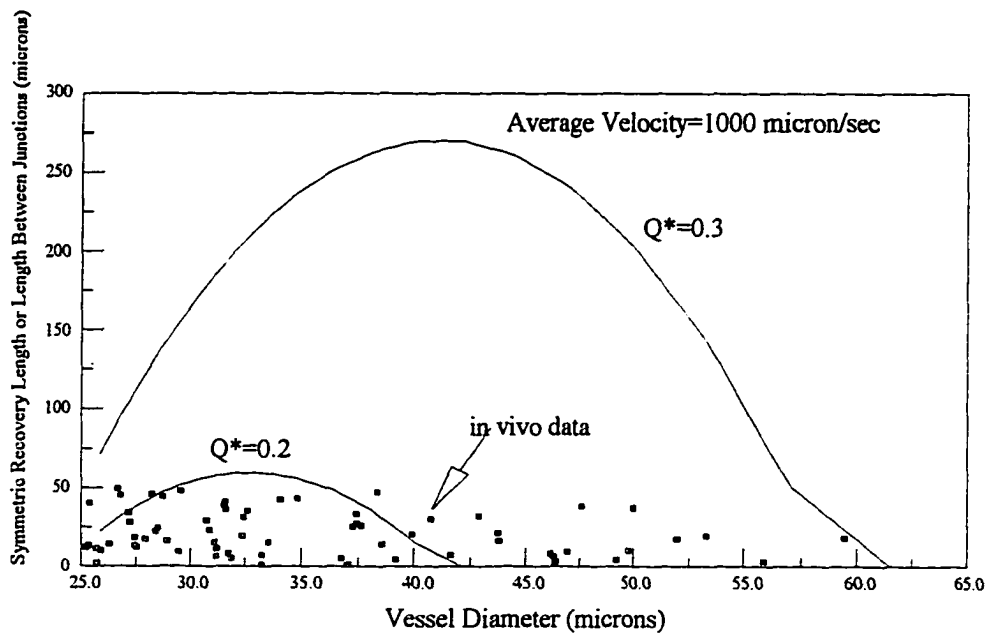


Figure 3-6. Comparison of symmetric recovery length and *in vivo* data for average velocity 1000 μ m/sec.

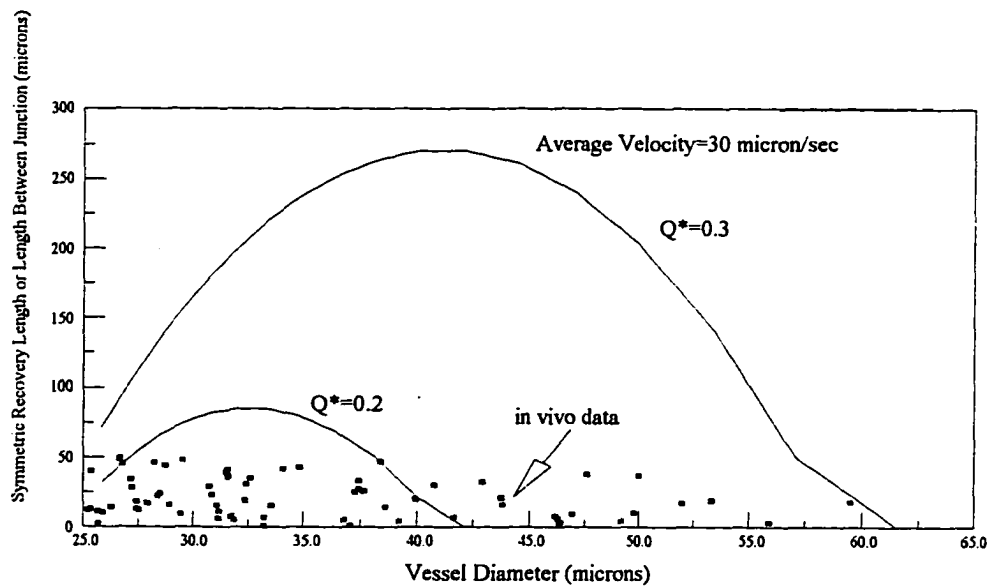


Figure 3-7. Comparison of symmetric recovery length and *in vivo* data for average velocity 30 μ m/sec.

CHAPTER IV

HETEROGENEITY OF BLOOD FLOW IN MICROVASCULAR NETWORK

4.1 Introduction

The most obvious feature of the microcirculation to the person who looks it through a microscope, is the large variability of microvascular structure (diameter, length, departure angle from the main branch). And the person will notice the fact that there is a great variability in red blood cell perfusion among individual microvascular vessels. Some arteriolar vessels appear to have few red blood cells traveling at high velocities, whereas other vessels have more red blood cells traveling at low velocities. This situation gets further complicated by the fact that red blood cells flow is not steady but fluctuates with time within each vessel.

Some studies[58-60] have been attempted to quantify this heterogeneity of perfusion and its physiological effects. The effect of hematocrit and red cell flow variation on oxygenation of different organs have been extensively studied. oxygen transport rate has been described either as being constant for a large range of hematocrits (as for myocardium), or as presenting an optimum for a given value of hematocrit depending on the organ considered. Even if total red cell flow arriving at the organ is constant in a large range of hematocrits as for myocardium, distribution of red cell flows into the organ can differ under the effect of rheological changes associated

with hematocrit changes. Large heterogeneity of red cell flow in the microvascular network suggests that consequences of hematocrit variations cannot be discussed solely in terms of total red cell flow or total oxygen arriving to the organ. Kanzow *et al.* [61] measured the hematocrit distribution in mesenteric microvascular network. For a given systemic hematocrit, a large heterogeneity of capillary discharge hematocrits has been reported. The heterogeneity is frequently reported to be the consequence of both a biologically controlled process (based on vascular tone) as well as a physical phenomena resulting from the unequal red cell partitioning at the bifurcations. Thus, it is apparent that a clear understanding of the amount of microvascular flow heterogeneity and its control in the microcirculation is essential to explain the interaction between tissue function and vascular perfusion.

The intrinsic heterogeneity of microcirculation perfusion can be described as spatial and temporal, respectively. The variability of perfusion among vessels at a given time has been termed as spatial heterogeneity, and temporal heterogeneity refers to the variability with time in a given vessel. The heterogeneity of perfusion can also change along a given vessel at a point in time. The physiological significance of spatial heterogeneity has been related to the efficiency of tissue oxygenation and capillary exchange of diffusible solutes[62]. Thus, one would expect that spatial heterogeneity should be under some kind of regulatory control on response to changes in metabolic demand or oxygen delivery to the microvasculature. The physiological significance of temporal heterogeneity , usually linked with vasomotion, has been less clear, although it likely affects the efficiency of microvascular exchange.

To understand how the heterogeneity of perfusion in microvasculature might be regulated or changed, one needs to consider the possible sources of this heterogeneity. Krogh [27] considered the capillary as the smallest independent controller of capillary perfusion. But Sweeney and Sarelius [63] showed the perfusion of large numbers of capillaries arising from a common arteriolar feed is coordinated. The control of capillary blood flow lies entirely within the arteriolar tree. Pries *et al* [64] reported the distribution of perfusion among the arteriolar feeding groups of capillaries reflected the level of perfusion within these capillaries. And temporal heterogeneity has been associated with arteriolar vasomotion. Thus, the arteriolar tree appears to be a major component in determining both spatial and temporal heterogeneity of capillary perfusion. Plasma skimming has been considered as a potential source of heterogeneity of perfusion within the arteriolar tree.

Another potential source of heterogeneity in microvasculature may be the capillary network. The capillary bed is made up of networks of interconnected diverging and converging capillary segments. This structure provides numerous alternate routes for red blood cells flow to follow. As a result, the level of flow in individual capillary segment must be quite different. This type of spatial heterogeneity has been called as the longitudinal heterogeneity in capillary segment flow [65]. The heterogeneity of microvascular flow also depends on tissue metabolism.

Up to the present, our understanding the properties of the microvasculature that lead to flow heterogeneity and how these properties might be regulated is far from complete. Research into this area has yielded contradictory results. Damon and Duling [66] reported the heterogeneity of capillary perfusion in striated muscle is constant and

independent of muscle blood flow and /or O₂ demand. Tyml and Mikulash [67] showed that the heterogeneity of red blood cells flow increased with reduced average flow rate. And many studies of spatial heterogeneity have depended on pooled *in vivo* data from randomly sampled capillaries in different animals. Tyml [68] pointed out that this sample method can result in a mixture of spatial and temporal heterogeneity.

4.2 Definition of Heterogeneity

Flow heterogeneity means that total flow is not distributed evenly among the perfused vessels. In opposition to heterogeneity, completely homogeneous perfusion is that all vessels receive $1/n$ of the total inflow, where n is the number of vessels arranged in parallel. If some vessels receive more and some less flow than their appropriate fraction of the total, the flow is judged to be heterogeneous.

The coefficient of variation or relative dispersion is widely used to quantify the extent of heterogeneity. The coefficient of variation is the quotient of the standard deviation and the mean. A common method to assess flow heterogeneity is to use tissue deposition indicators (e. g. tritiated water, antipyrine, and microspheres). Those indicators are deposited in the tissue in proportion to the rate at which they are convected into a region by the inflowing blood. The tissue will be dissected into small samples and the flow in each pieces of tissue will be estimated from the quantity of indicator trapped. Although these techniques give a way to measure flow heterogeneity, they have some limits. The accuracy of these methods is inversely proportional to the organ sample size. And the size of organ in which heterogeneity will be detected

depends on the specific activity of the indicator and the amount of indicator that can be deposited in the organ. Using microspheres as indicator just can detect flow heterogeneity in arterioles. Bassingthwaighte *et al.* [69] have shown that the coefficient of variation depends on the size of the pieces of the sample to be divided into. The coefficient of variation is zero for completely homogeneous perfusion. But this index of heterogeneity has no upper bound. It causes problem in comparing heterogeneity between different microvascular networks, tissues, organs and animal species. Bassingthwaighte has therefore adopted a fractal approach to describe heterogeneity.

A fractal structure is a shape composed of smaller parts which are similar to the whole. Mandelbrot [70] showed that the diameters of successive branches of the bronchial tree and of the arteries of an organ have fractal structure. A heterogeneous distribution of blood flow could be one consequence of the passive architecture of the fractal vasculature. Glenny and Robertson [71] showed that the heterogeneity of pulmonary blood flow has a fractal dimension of ~ 1.1 . Bassingthwaighte *et al.* [69] obtained a fractal dimension of 1.17-1.25 for the dispersion of myocardial blood flow by using the following method. Assume $RD(m)$ is the coefficient of variation in the blood flow distribution for a sample size m . The dependence of $RD(m)$ on the sample size m has the following relation.

$$RD(m) = RD(m_0) \left(\frac{m}{m_0} \right)^{1-D} \quad (4-1)$$

where m_0 is an arbitrary reference size, $RD(m_0)$ is the coefficient of variation for sample size of m_0 , and D is the spatial fractal dimension. Bassingthwaighte concluded that when $D=1$, a lower limit is reached, the coefficient of variation keeps the same for all of

the sample size. That represents a uniform or completely homogeneous blood flow distribution. When $D=1.5$, the upper limit is obtained that indicates the distribution of blood flow in the network is completely random or completely heterogeneous.

In this study a new method to measure the extent of heterogeneity of blood, red blood cell flows and hematocrit in network is proposed. This method is based on the concepts from vector algebra. In order to carry out a network analysis, it is necessary to specify the network topology. The Horton scheme may be useful in identifying functionally homogeneous groups of vessels. It is not suitable for study of the distribution of microvascular blood flow, red cell flow or/and hematocrit. Gaetgens[72] proposed the complete flow cross-section scheme for such study. A complete flow cross-section has one inflow and several outflows. Conservation of mass in any complete cross-section under steady state requires the sum of the outflow blood and red blood cells equals the inflow blood and red blood cells. The advantage of this scheme is that it can trace the whole inflow into a network through its microvessel segments and find the distributions of blood, red blood cell and hematocrit among the network.

A useful value of heterogeneity should be bounded by lower and upper limits. The lower limit is the completely homogeneous distribution. A homogeneous distribution for blood volumetric flow is all of outflows have the same volumetric flow value. If the blood inflow is 1, then volumetric flow for all of outflows are $1/n$, assuming the complete flow cross-section has n outflows. A homogeneous red blood cell flow distribution is that the red blood cell flow in each outflow has the same value. If the red blood cell inflow is 1, then the red blood cell flow in each outflow branch is equal to $1/n$,

assumed the network considered has n outflows. A homogeneous hematocrit distribution happens when the hematocrit in each outflow branch is equal. If the hematocrit in feeding blood is H , then the hematocrit in each outflow branch is H too.

The opposing case to a homogeneous distribution is called a completely heterogeneous distribution. A completely heterogeneous blood flow and red blood cell distribution occurs when one of the outflow branch receives all of the inflow (volumetric or red blood cell) and the other outflow branches receive nothing. The completely heterogeneous hematocrit distribution depends on the structure of the complete flow cross-section network to be considered. If the network is a serial tree type, a completely heterogeneous hematocrit distribution happens when the outflow branch which is the farthest away from the inflow branch receives all of feeding hematocrit and the other outflow branches receive nothing. If the network is a parallel tree type, a completely heterogeneous hematocrit distribution happens when one of the outflow branch receives all of the feeding hematocrit and the other outflow branches receive nothing. This definition of completely heterogeneous distribution is based on conservation of mass over the complete flow cross-section. It represent a natural upper limit for heterogeneity of spatial network.

A complete flow cross-section network is considered by vector algebra. A vector is defined by the value and direction of its each component . It means not only the value in each branch is important, but also the ordering of these values. Assume in a given complete flow cross-section network there are n outflow branches. Each branch is given an ordering number. The spatial distribution of blood flow, hematocrit and red blood cell flow are represented by three n dimensional vectors \mathbf{Q} , \mathbf{H} , and \mathbf{R} . \mathbf{Q} is the vector of

blood flow. \mathbf{H} is the vector of hematocrit and \mathbf{R} is the vector of red blood cell flow. The components of each vector are the value of blood flow, hematocrit and red blood cell flow in each ordering outflow branch. The components in each vector have the following relation.

$$R_i = Q_i \times H_i \quad (4-2)$$

The degree of heterogeneity for a given complete flow cross-section network is determined by comparing the vector which describe that distribution with the homogeneous vector. One way to compare the vectors is to compute the magnitude of the difference between those two vectors. Because this difference magnitude depends on the dimension of vector space, it is convenient to normalize this difference magnitude by the magnitude of the homogeneous vector. The normalized magnitude of the vector difference is called the “magnitude of heterogeneity”. Assume V_i is the components of a n -dimensional vector and V_0 is the components of corresponding homogeneous vector. Then the magnitude of heterogeneity is:

$$M_v = \frac{\sqrt{\sum (V_i - V_0)^2}}{V_0 \sqrt{n}} \quad (4-3)$$

The summation includes all of the outflow branches in the complete flow cross-section network. For a completely homogeneous distribution the magnitude of heterogeneity is zero. Completely heterogeneous distributions for blood flow and red blood cell flow have the magnitudes of heterogeneous of $\sqrt{(n-1)}$. For a completely heterogeneous distribution for hematocrit in a serial tree network the magnitude of heterogeneity is given as follows.

$$(M_H)_{\max} = e^{0.05727n} \quad (4-4)$$

where n is the number of the outflow branches in a serial tree network. Equation 4-4 is empirical curve fit for a completely heterogeneity of hematocrit. For a serial tree network a completely heterogeneous distribution for hematocrit happens when all of the branches except the last one receive only plasma and the last branch get all of the feeding hematocrit. For a parallel tree type network a completely heterogeneous distribution for hematocrit has the magnitude of heterogeneity calculated from equation 4-4. In equation 4-4 n is the number of the outflow branches of the largest serial tree inside the parallel tree. Because the magnitude of heterogeneity has both upper and lower limits, it can be scaled to range from 0 for a completely homogeneous distribution to 1 for a completely heterogeneous distribution.

4.3 Complete Flow Cross-Section Network

The configuration of the complete flow cross-section network to be considered includes both serial and parallel tree branching arrangement. For a serial tree network, the parent and daughter branches have the same diameters. The diameters used are 28, 35, or 40 μ m. The branch junction segment is assumed to have the same length in any one numerical calculation. The departure angles which are the angles around the main branch axis between the spatial direction of each successive side branch are 60°, 90°, 180°, 360°. Network topologies with the different departure angles are shown in Figures 4-1 to 4-6. The networks shown in Figure 4-1 and 4-2 have 2 dimension structure. And the networks shown in Figure 4-3 and 4-4 have 3 dimension structure. In this study,

these networks will be used to investigate how the network topology effect the heterogeneties of blood flow, red blood cell flow or/and hematocrit.

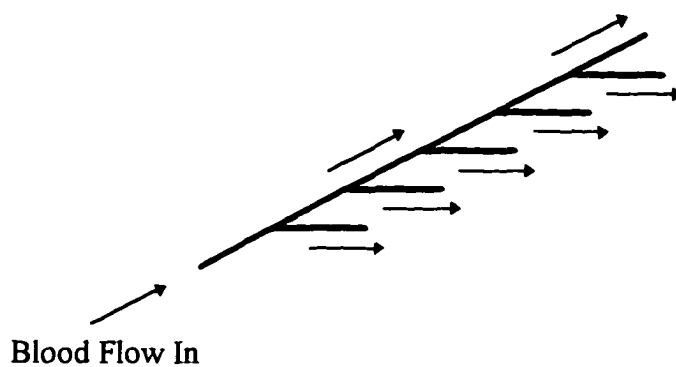


Figure 4-1. Microvascular Network Structure: Branches at the same side

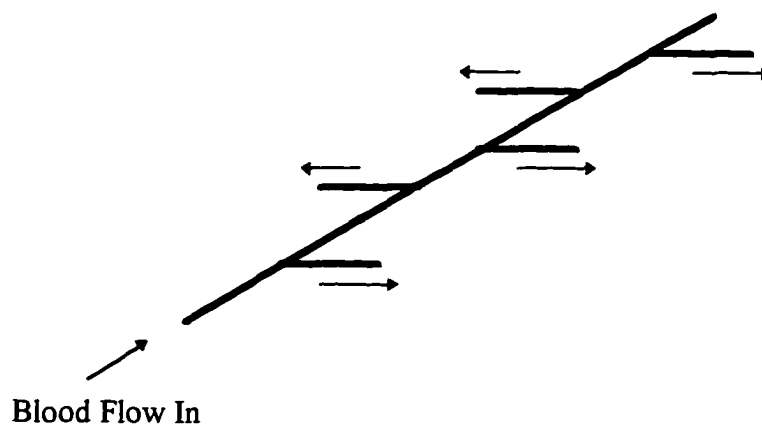


Figure 4-2. Microvascular Network Structure: Branches alternating or rotating 180°

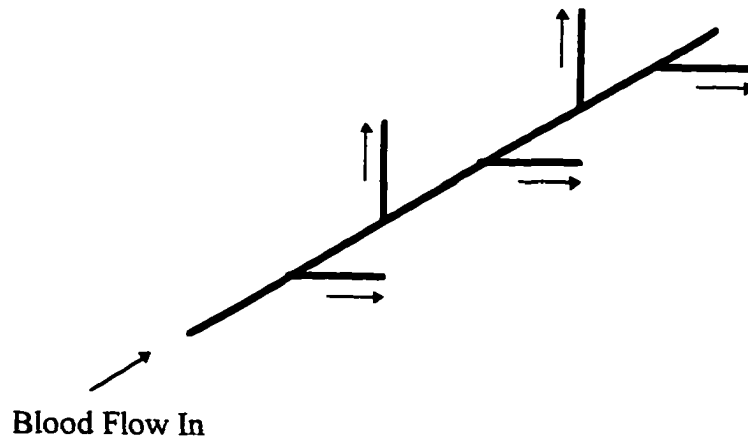


Figure 4-3. Microvascular Network Structure: Branches alternating 90°

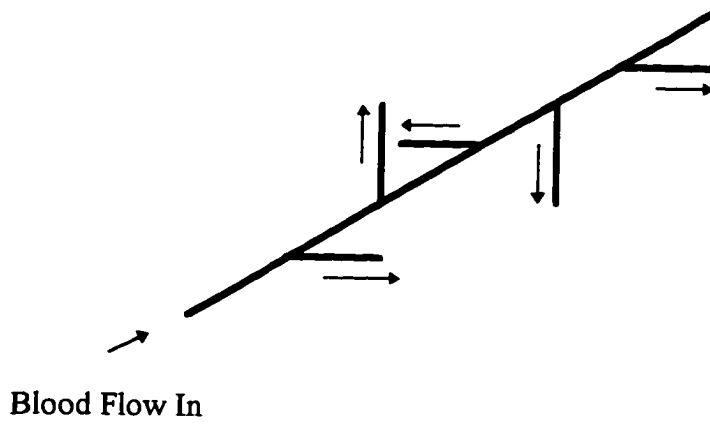


Figure 4-4. Microvascular Network Structure: Branches rotating 90°

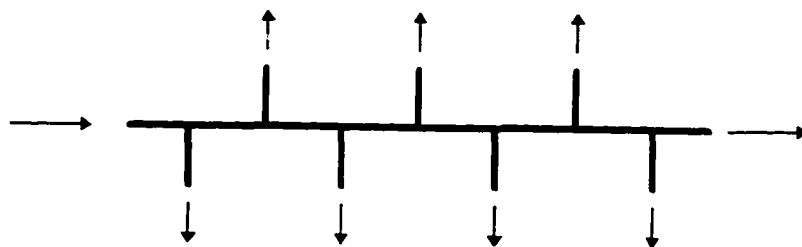


Figure 4-5. Microvascular Network Structure: Serial Tree

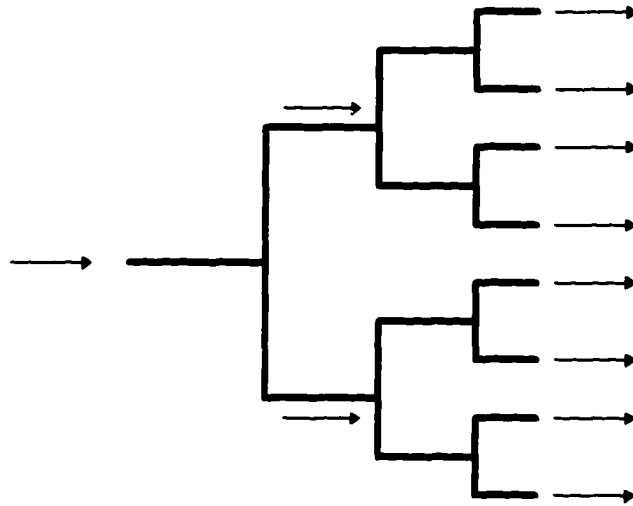


Figure 4-6. Microvascular Network Structure: Parallel Tree

4.4 Computational Results

The mathematical models described in the previous chapters are applied to complete flow cross-section microvascular networks to investigate the heterogeneity of hematocrit and red blood cell flow. The discharge hematocrit and red blood cell flow in each branch of the microvascular network for different geometry parameters and topological arrangement are computed when the different distribution of blood flow in branches of a given vascular tree are used as initial inputs. The distribution of blood flow which satisfy the mass conservation is randomly generated. The computation take account of the plasma skimming at each branch, or red blood cell concentration profile shifts at each branch and red blood cell dispersion process in junction segment.

The first question to be answered is whether there is a correlation between the heterogeneity of hematocrit and the heterogeneity of blood flow, between the heterogeneity of red blood cell and the heterogeneity of blood flow for a given

microvascular network. For this purpose the branch alternating 180° serial tree is selected. The symmetric profile model is used as the dispersion model for the dispersion of red blood cell between junctions. The symmetric profile model decreased the computational time. 2000 different distribution of blood flow are randomly generated to be the input of the computation. The results are shown in Figures 4-7 and 4-8. No correlation between the magnitude of hematocrit heterogeneity and blood flow heterogeneity exists. A minimum point of the magnitude of hematocrit heterogeneity is observed when the magnitude of blood flow is around 0.4 to 0.6. For a given value of the magnitude of blood flow a minimum value for the magnitude of hematocrit heterogeneity can be found. But the maximum value for the magnitude of hematocrit heterogeneity is undefined. Figure 4-8 is the plot of the magnitude of red blood cell heterogeneity verse the magnitude of blood flow.

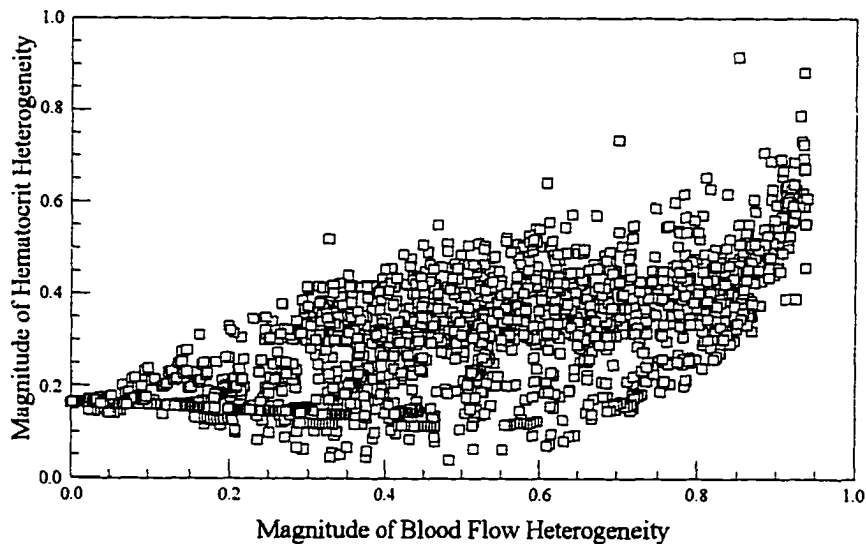


Figure 4-7 The heterogeneity of hematocrit for a serial tree with six branches. The symmetric dispersion model was used in calculation.

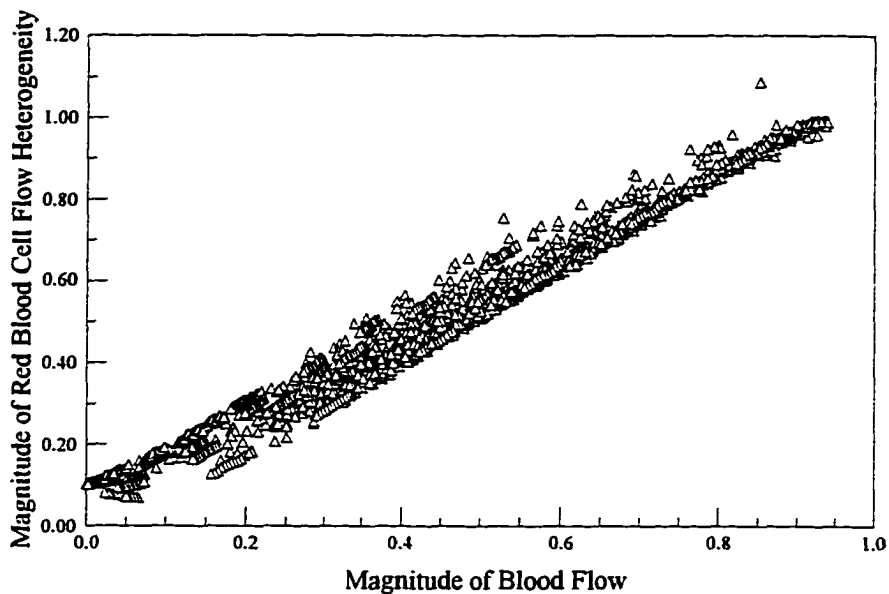


Figure 4-8. The heterogeneity of red blood cell flow for a serial tree with six branches. The symmetric dispersion model was used in calculation

A strong correlation between the magnitude of red blood cell heterogeneity and the magnitude of blood flow heterogeneity is observed (see Figure 4-8). The magnitude of red blood cell heterogeneity increases as the increase of the magnitude of blood flow heterogeneity.

The next question to be answered is how the vascular tree spatial geometry influences the heterogeneity of hematocrit, red blood cell and blood flow. This influence includes two major factors. One of factors is plasma skimming at bifurcations. The thickness of plasma layer plays an important role in plasma skimming. The role played by the plasma layer can be expressed by the ratio of the cell to parent vessel diameter, D_c/D_p . In this study the parent vessel diameter is changed to investigate the role of plasma skimming on the heterogeneity of hematocrit, red blood cell and blood flow. The

other factor is the rheology of vascular trees. Can the disturbance of red blood cell profile caused by plasma skimming at a bifurcation propagate to the downstream in a network and then affect the distribution of hematocrit and red cell flow? The concentration profile is shifted when blood pass through a bifurcation. In the previous chapters the symmetry recovery length is obtained under different conditions. If the distances between bifurcations are greater than the symmetry recovery length, then the shifting red blood cell concentration profile become axisymmetry before the blood reaches the next bifurcation. In this case, the disturbance does not propagate to the downstream bifurcation. There is no communication between the bifurcations. So the plasma skimming at each bifurcation determine the distribution of hematocrit and red blood cell flow. If the distances between bifurcations are less than the symmetry recovery length. The disturbance can propagate to the downstream network and influence the distribution of hematocrit and red blood cell flow. The spatial arrangement of branches can influence the distribution of hematocrit and red blood cell flow. In this study the departure angle is changed to consider the effect of the spatial arrangement of branches. Also the branch arrangement (serial or parallel) can affect the distribution of hematocrit and red blood cell flow.

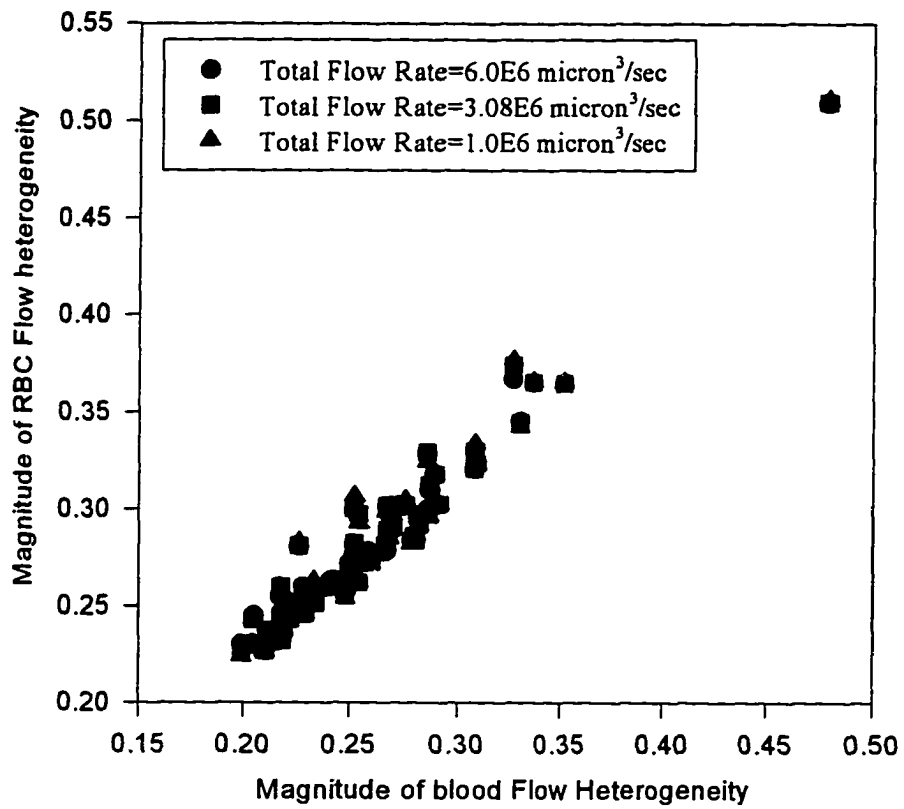


Figure 4-9. Magnitude of RBC flow heterogeneity as a function of magnitude of blood flow heterogeneity at different total flow rates

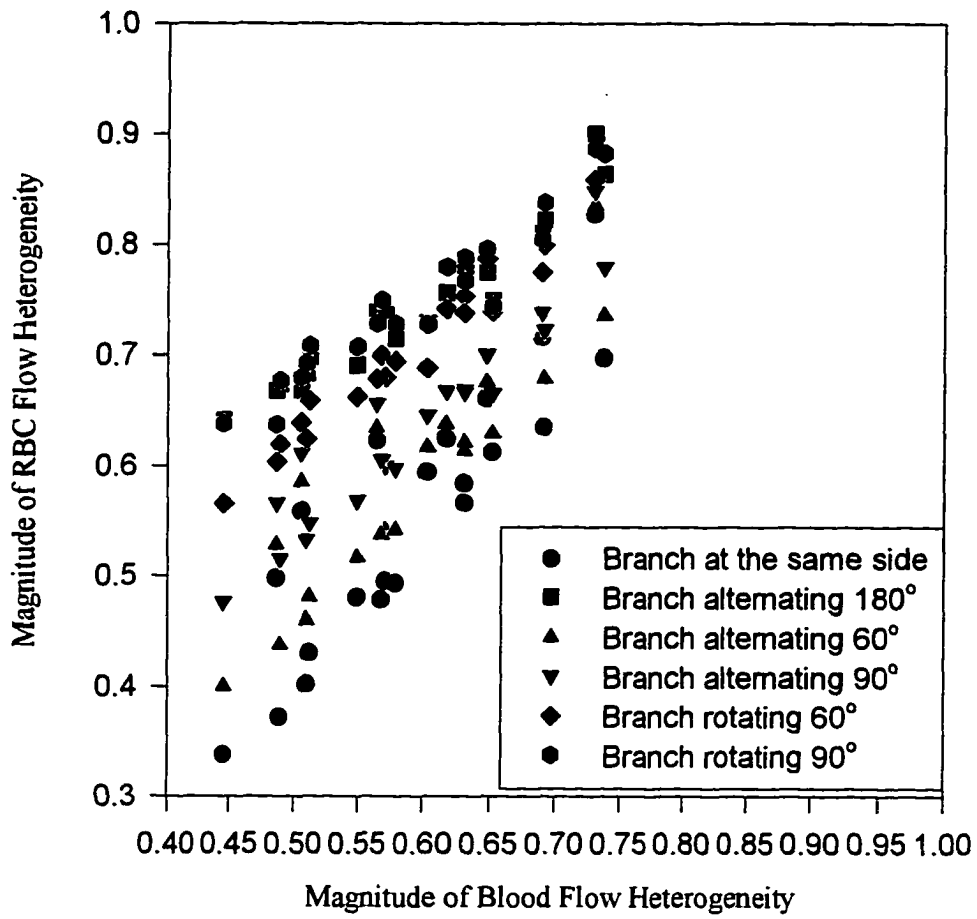


Figure 4-10 Magnitude of RBC heterogeneity as a function of magnitude of blood flow heterogeneity for different departure angles

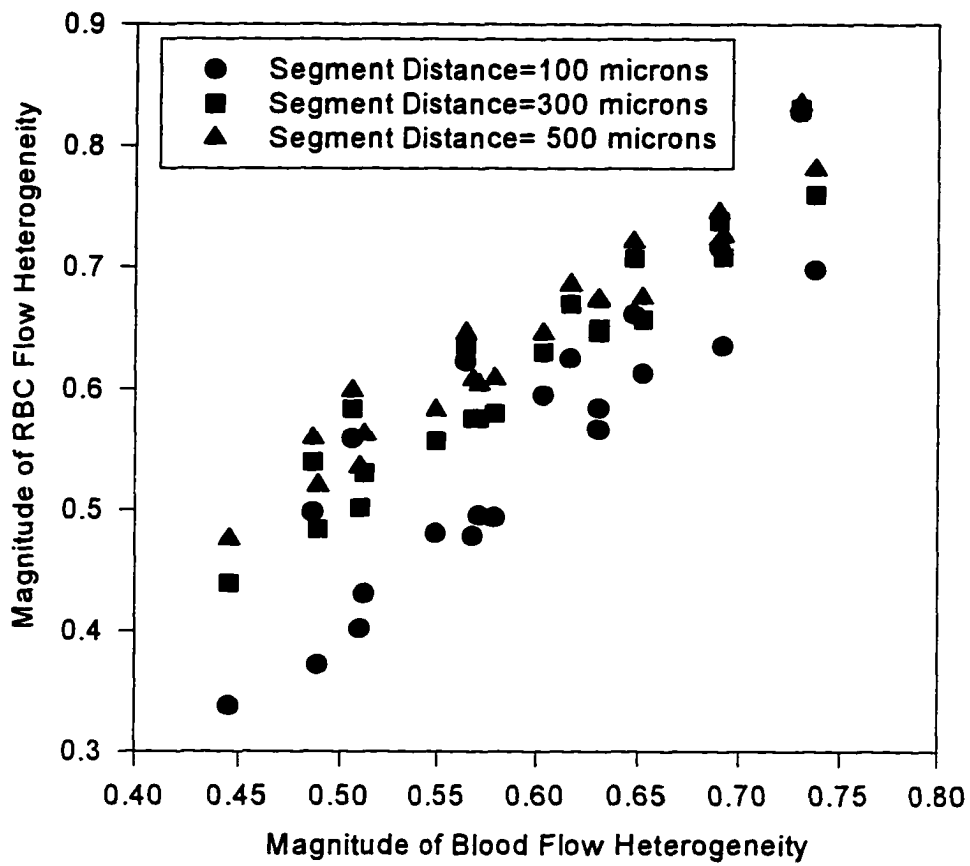


Figure 4-11 Magnitude of RBC heterogeneity as a function of magnitude of blood flow heterogeneity at different segment distances for branches at the same side

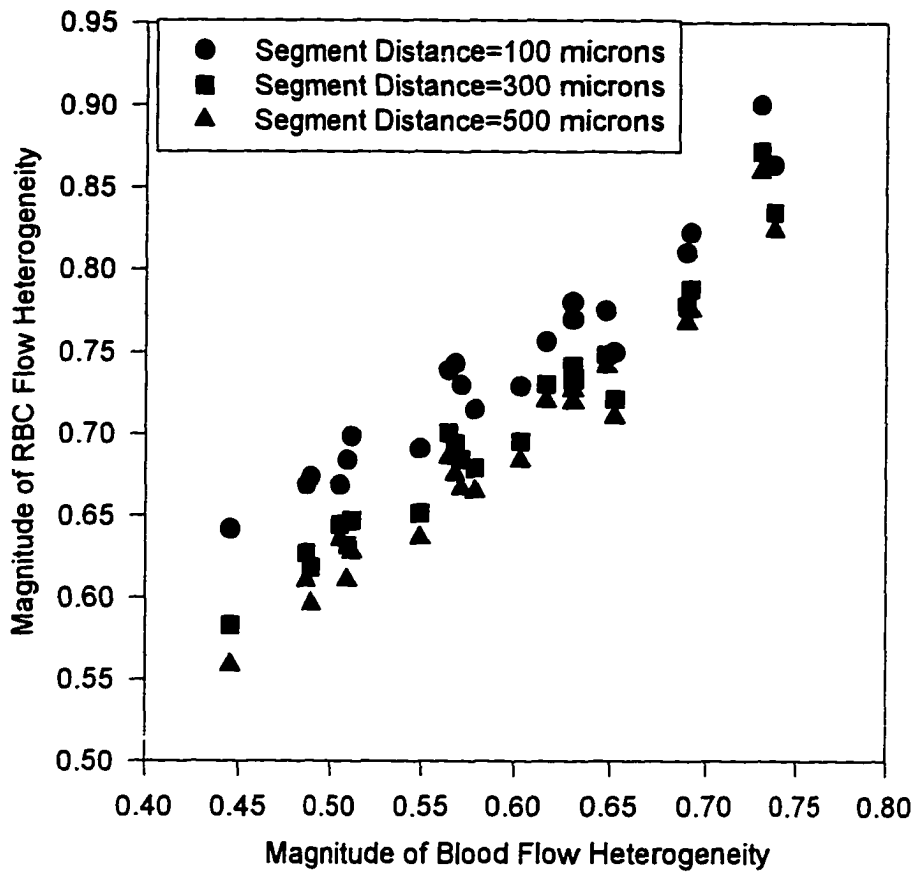


Figure 4-12 Magnitude of RBC flow heterogeneity as a function of magnitude of blood flow heterogeneity at different segment distances for alternating 180° branch.

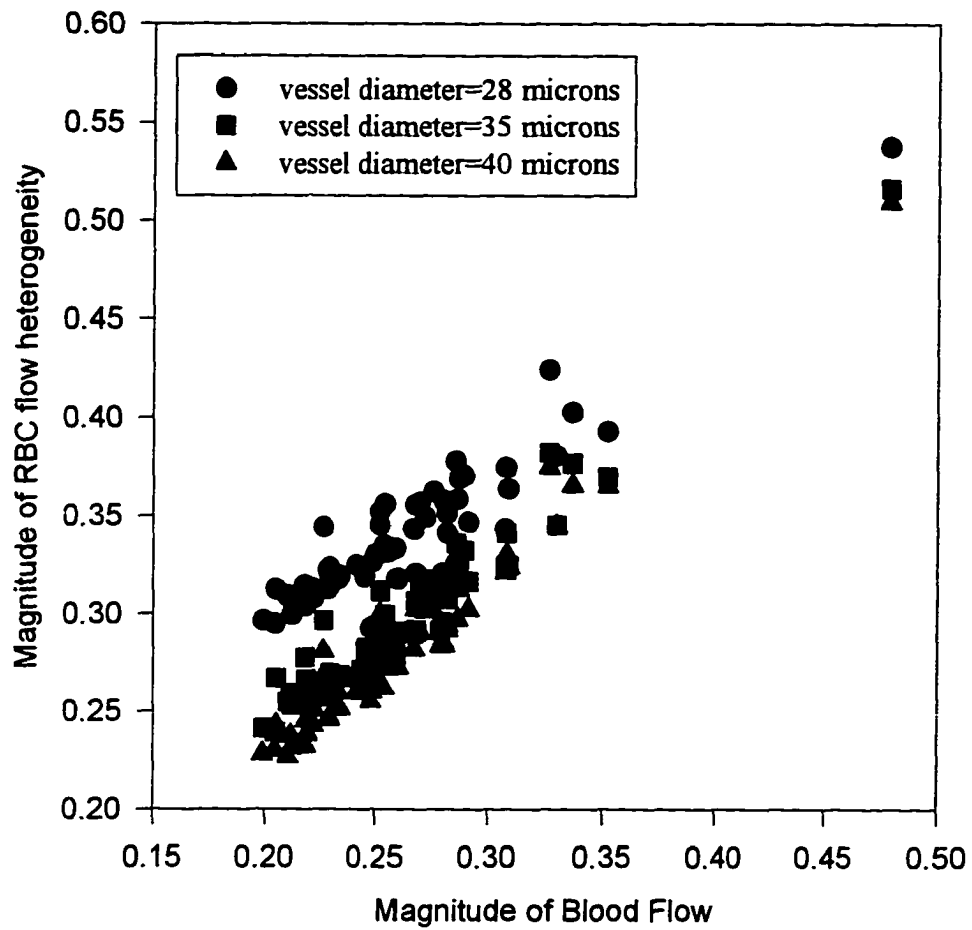


Figure 4-13. Magnitude of RBC flow heterogeneity as a function of magnitude of blood flow heterogeneity for different vessel diameters for a serial tree with branches at the same side.

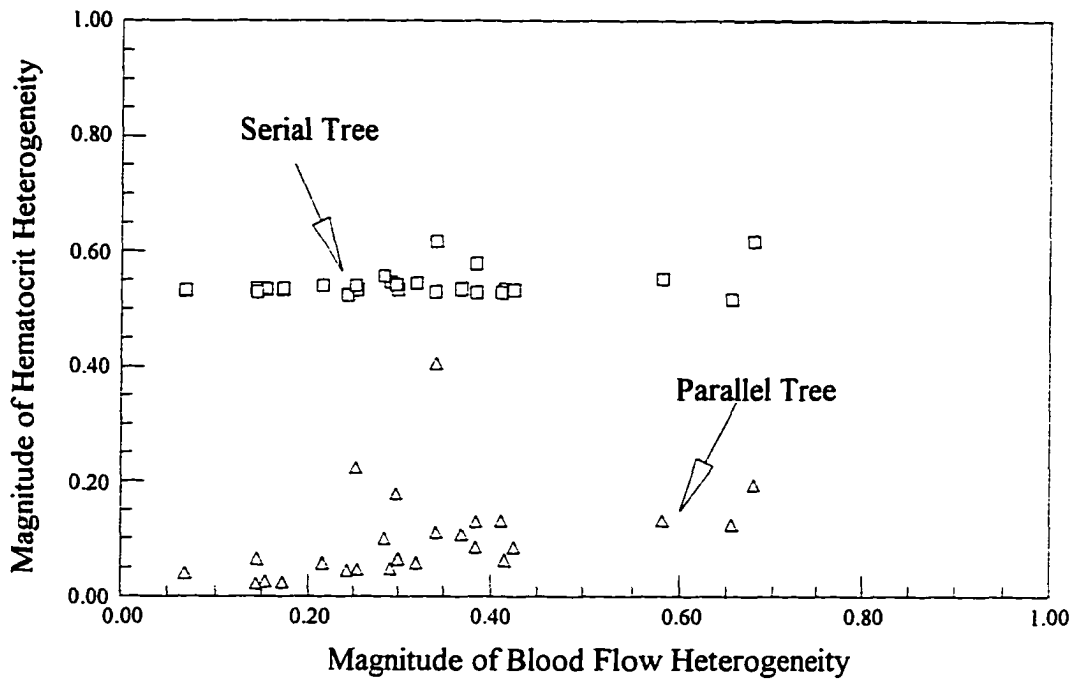


Figure 4-14. Comparison of hematocrit heterogeneity for serial and parallel trees.

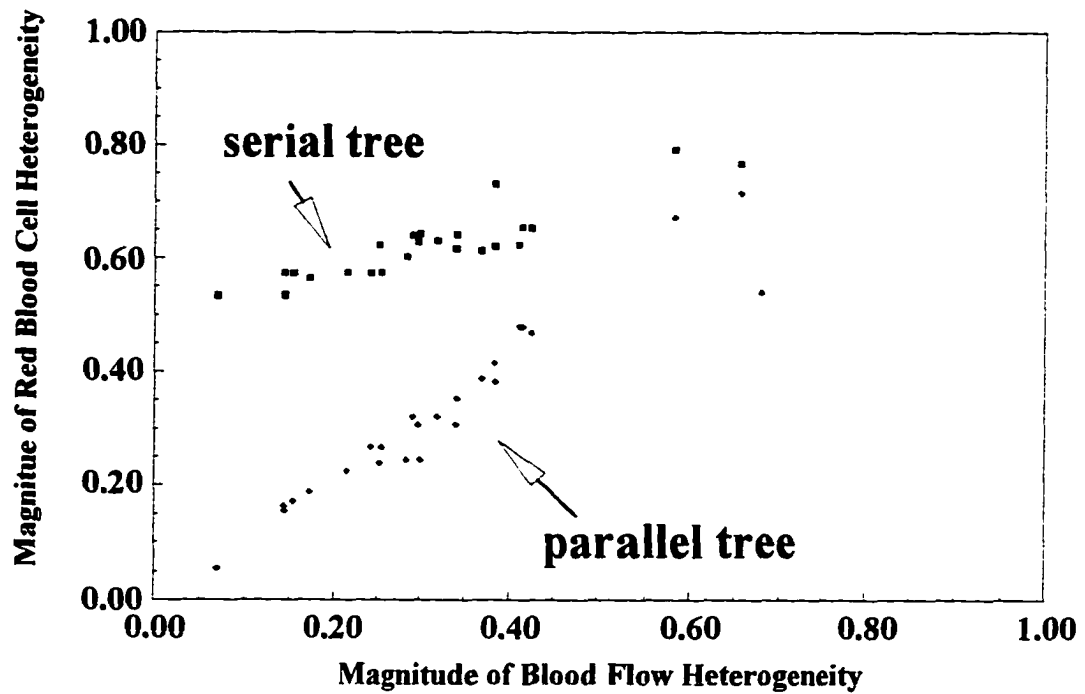


Figure 4-15. Comparison of red blood cell flow heterogeneity for serial and parallel trees.

Figure 4-9 showed the change of magnitude of red blood cell heterogeneity as a function of magnitude of blood flow heterogeneity at different total feeding flow rates. The complete flow cross-section network considered is that all of the branches are at the same sides of the parent vessel on one plane. The network was shown as Figure 4-1. The diameters for all of segments in the network are 28 μm . As the total feeding flow rate changed from 1.0×10^6 to 6.0×10^6 $\mu\text{m}^3/\text{sec}$, the relationship between magnitude of red blood cell heterogeneity and magnitude of blood flow heterogeneity did not change. It means that the total feeding flow rate has not influence on the magnitude of red blood cell heterogeneity.

Figure 4-10 shows the influence of departure angles on the magnitude of red blood flow heterogeneity. The complete flow cross-section network considered is a serial tree with six flow outlets. All of the branch segment distance are set the same. They are 100 μm . The diameter is 28 μm . The serial tree with branches at the same sides has the lowest red blood cell heterogeneity. The serial tree with an alternating 180° departure angle for the branches showed in Figure 4-10 has the highest red blood flow heterogeneity. The serial tree with a rotating 90° departure angle for the branches showed in Figure 4-10 has almost the same red blood flow heterogeneity as the one with a alternating 180° departure angle. The magnitude of red blood flow heterogeneity for serial trees with branches alternating 60° , 90° and rotating 90° is located in the middle of magnitudes of red blood flow heterogeneity for serial trees with branches alternating 180° and at the same side. Notice that the serial trees with branches rotating 60° and 90° have 3 dimensional structures, and the serial trees with branches alternating 180° and at

the same side have 2 dimensional structures. It means that the range of the magnitude of red blood flow heterogeneity for serial trees which have 2 dimensional structures can cover the magnitude of red blood flow heterogeneity for serial trees which have 3 dimensional structures. This result can be interpreted that the computational results for microvascular networks which have 2 dimensional structures can be used to represent the results for microvascular network which have 3 dimensional structures. Comparing the results of magnitudes of red blood flow heterogeneity for the networks with branches rotating 90° and alternating 90° shows the departure angle has some influence on the magnitude of red blood flow heterogeneity.

Figure 4-11 shows the influence of branch segment distance on the magnitude of red blood cell flow heterogeneity. Branches of the serial tree considered are at the same sides. The diameter is $28\ \mu\text{m}$. Notice that as the distance increases the magnitude of red blood cell flow heterogeneity increases. The red blood cell concentration profile becomes more axisymmetry as the branch segment distance increases. The more axisymmetric red blood cell concentration profile in each branch segment results in higher magnitude of red blood cell flow heterogeneity. This result can be explained by the plasma skimming at the bifurcations. If more plasma is withdrawn out at each bifurcation, the higher the magnitude of red blood cell flow heterogeneity. For the serial tree with branches at the same sides the more axisymmetric concentration profile allows more plasma skimming at the bifurcations. So the higher magnitude of red blood cell flow heterogeneity means the same side microvascular network has more axisymmetric concentration profile. A similar plot is given in Figure 4-12 for the alternating side

branch microvascular network. In contrast to the same side microvascular network, the magnitude of red blood cell heterogeneity decreases as the branch segment distance increases. When the blood flows through a bifurcation, the concentration profile will be shifted off axisymmetric. If the next downstream bifurcation is in the opposite direction, more plasma without red blood cells can be drawn into this bifurcation when the branch segment distance is shorter. It will let the last branch has almost all of the feeding red blood cells. It will results in the higher magnitude of red blood cell heterogeneity.

Figure 4-13 shows the influence of vessel diameter on the magnitude of red blood cell flow heterogeneity. The result is for the same side network with vessel diameters of 28, 35 and 40 μm . As the vessel diameter increases the magnitude of red blood cell flow heterogeneity decreases. It is usually considered that the plasma layer plays an important role in the red blood cell flow heterogeneity. But in larger microvascular vessels the importance of plasma layer becomes less.

The results for comparing the serial branching and parallel branching trees were shown in Figure 4-14 and 4-15. Both serial and parallel trees have eight flow outlets. The same blood flow distributions were used in the computations. The computational results show that the serial microvascular tree has a higher heterogeneity of red blood cell distribution than the parallel microvascular tree.

CHAPTER V

CONCLUSIONS AND RECOMMENDATIONS

The conclusions of this study are as follows:

1. A mathematical model using the variable dispersion model, two-phase velocity profile and the asymptotic flat red blood cell concentration best described the in vitro experimental data.
2. The model predicts that asymmetric red blood cell concentration profiles can exist in microvascular vessels with 25 μm or larger diameters.
3. A method to measure the heterogeneity of blood flow distribution in microvascular network is proposed. This method is based on vector algebra and mass of conservation in a complete flow cross-section network. It can be used to compare the experimental data from different species and laboratories.
4. Combining the mathematical models for plasma skimming at bifurcations and red blood cell dispersion process between junctions, the distribution of hematocrit and red blood cell concentration can be obtained over a serial or parallel type of microvascular tree.
5. A strong correlation exists between the heterogeneity of red blood cell flow and the heterogeneity of blood flow. No obvious correlation between the heterogeneity of hematocrit and the heterogeneity of blood flow is observed.

6. The feeding blood flow rate has no impact on the heterogeneity of red blood cell distribution in microvascular networks.
7. The heterogeneity of red blood cell flow in three dimensional microvascular networks is bounded by the heterogeneity in two dimensional microvascular networks.
8. A serial microvascular tree has higher heterogeneity of red blood cell flow than a parallel tree.

Based on the results obtained in this study the following recommendations are made:

1. Asymmetric red blood cell profile should be considered in modeling the blood flow in large microvascular networks.
2. A correlation between the width of plasma layer and shear rate, the ratio of cell diameter to the vessel diameter needs to be developed.

BIBLIOGRAPHY

1. Cokelet, G.R., *The rheology of human blood*, in *Biomechanics, Its Foundations and Objectives*, Y. C. Fung, N. Perrone, and M. Anliker, Editors. 1972, Prentice-Hall: N. J. p. 63-103.
2. Poiseuille, J.L.M., *Recherches experimentales sur le mouvement des liquides dans les tubes de tres petits diametres*. C. R. Acad. Sci., 1840. **11**: p. 961-967.
3. Chien, S., *Shear dependence of effective cell volume as a determinant of blood viscosity*. Science, 1970. **168**: p. 977.
4. Caro, C.G., *et al.*, *The mechanics of the circulation*. 1978: Oxford.
5. Williams, D.A. and S.S. Segal, *Microvascular Architecture in Rat Soleus and Extensor Digitorum Longus Muscles*. Micro. Res., 1992. **43**: p. 192-204.
6. Fenton, B.M. and B.W. Zweifach, *Microcirculatory model relating geometrical variation to change in pressure and flow rate*. Annals Biomed. Eng., 1981. **9**: p. 303-312.
7. Popel, A.S., *Network models of peripheral circulation.*, in *Handbook of Bioengineering*, R. Skalak and S. Chien, Editors. 1987, McGraw Hill: New York.
8. Goldsmith, H.L., *Red cell motions and wall interactions in tube flow*. Federation Proceedings, 1971. **30**: p. 1578-1588.
9. Schmid-Schonbein, G.W. and B.W. Zweifach, *RBC velocity profiles in arterioles and venules of the rabbit omentum*. Microvasc. Res., 1975. **10**: p. 153-164.
10. Tangelder, G.J., *et al.*, *Velocity profiles of blood platelets and red blood cells flowing in arterioles of the rabbit mesentery*. Circulation Research, 1986. **59**(5): p. 505-514.
11. Baker, M. and H. Wayland, *On-line volumetric flow rate and velocity profile measurement for blood microvessels*. Microvasc. Res., 1974. **7**: p. 131-143.
12. Sato, M. and N. Ohshima, *Velocity profiles of blood flow in microvessels measured by ten channels' dual-sensor method*. Biorheology, 1988. **25**: p. 279-287.

13. Goldsmith, H.L. and S.G. Mason, *The microrheology of dispersions*, in *Rheology theory and applications*, F.R. Eirich, Editor. 1967, Academic.
14. Thomas, H.W., *The wall effect in capillary instruments: an improved analysis suitable for application to blood and other particulate suspensions*. *Biorheology*, 1962. 1: p. 41-56.
15. Bugliarello, G. and J. Sevilla, *Velocity distribution and other characteristics of steady and pulsatile blood flow in fine glass tubes*. *Biorheology*, 1970. 7: p. 85-107.
16. Tateishi, N., *et al.*, *Flow dynamics of erythrocytes in microvessels of isolated rabbit mesentery: cell-free layer and flow resistance*. *J. Biomechanics*, 1994. 27(9): p. 1119-1125.
17. Lipowsky, H.H. and B.W. Zweifach, *Network analysis of microcirculation of cat mesentery*. *Microvasc. Res.*, 1974. 7: p. 73-83.
18. Larsen, O.A. and N.A. Lassen, *Cerebral hematocrit in normal man*. *J. Applied Physiol.*, 1976. 19: p. 571-574.
19. Oldendorf, W.H., *et al.*, *Hematocrit of the human cranial blood pool*. *Circ. Res.*, 1965. 17: p. 532-539.
20. Pappenheimer, J.R. and W.B. Kinter, *Hematocrit ratio of blood within mammalian kidney and its significance for renal hemodynamics*. *Am. J. Physiol.*, 1956. 185: p. 377-390.
21. Bloch, E.H., *Quantitative study of the hemodynamics in the living microvascular system*. *Am. J. Anat.*, 1962. 110: p. 125-146.
22. Newcomb, S.L. and G.G. Power, *Hematocrit of the fetal rabbit placenta*. *Am. J. Physiol.*, 1975. 215: p. 486-495.
23. Barbee, J.H. and G.R. Cokelet, *Prediction of blood flow in tubes with diameters as small as 29 μm* . *Microvasc. Res.*, 1971. 3: p. 17-21.
24. Cokelet, G.R., *Blood rheology interpreted through the flow properties of the red cell.*, in *Microcirculation*, J. Grayson and W. Zingg, Editors. 1976, Plenum: New York. p. 9-23.
25. Pries, A.R., K. Ley, and P. Gaehtgens, *Generalization of the Fahraeus principle for microvessel networks*. *Am. J. Physiol.*, 1986. 251: p. H1324-H1332.
26. Krogh, A., *The Anatomy and Physiology of Capillaries*. 1922, Yale University, New Haven, CT.

27. Krogh, A., *Effect of oxygen supply to the tissue and the regulation to the capillary circulation*. J. Physiol (London), 1919. **52**: p. 457-474.
28. Svanes, S.R. and B.W. Zweifach, *Variation in small blood vessel hematocrits produced in hypothermic rats by micro-occlusion*. Microvasc. Res., 1968. **1**: p. 210-221.
29. Johnson, P.C., *Red cell separation in the mesenteric capillary network*. Am. J. Physiol., 1971. **221**: p. 99-104.
30. Schmid-Schonbein, G.W., *et al.*, *Cell distribution in capillary networks*. Microvasc. Res., 1980. **19**: p. 18-44.
31. Bugliarello, G. and C.C. Hsiao, *Phase separation in suspensions flowing through bifurcations: A simplified hemodynamic model*. Science, 1964. **143**: p. 469-471.
32. Yen, R.T. and Y.C. Fung, *Effect of velocity distribution on red cell distribution in capillary blood vessels*. Am. J. Physiol., 1978. **235**: p. H251-H257.
33. Palmer, A.A., *Axial drift of cells and partial plasma skimming in blood flowing through glass slits*. Am. J. Physiol., 1965. **209**: p. 1115-1122.
34. Fenton, B.M., R.T. Carr, and G.R. Cokelet, *Nonuniform red cell distribution in 20 to 100 μm bifurcations*. Microvasc. Res., 1985. **29**: p. 103-126.
35. Carr, R.T. and L.L. Wickham, *Plasma skimming in serial microvascular bifurcations*. Microvasc. Res., 1990. **40**: p. 179-190.
36. Klitzman, B. and P.C. Johnson, *Capillary network geometry and red cell distribution in hamster cremaster muscle*. Am. J. Physiol., 1982. **242**: p. H211-H219.
37. Pries, A.R., K.H. Albrecht, and P. Gaehtgens, *Model studies on phase separations at a capillary orifice*. Biorheology, 1981. **18**: p. 355-367.
38. Carr, R.T. and S.L. Kotha, *Separation Surfaces for Laminar Flow in Branching Tubes—Effect of Reynolds Number and Geometry*. J. of Biomech. Eng., 1995. **117**: p. 442-447.
39. Goldsmith, H.L., *The flow of model particles and blood cells and its relation to thrombogenesis*, in *Progress in Hemostasis and Thrombosis*, A.S. Grune and L.W. Stratton, Editors. 1972. p. 178-230.

40. Fu, W.-R., *Computational Study of Red Cell Distribution in Simple Networks*. PhD dissertation, in *Chemical Engineering*, 1990, University of New Hampshire: Durham.
41. Barbee, J.H., *The flow of human blood through capillary tubes with inside diameters between 8.7 and 2.21 microns*. Ph. D. dissertation, 1971, California Institute of Technology.
42. Perkkio, J. and R. Keskinen, *Hematocrit reduction in bifurcations due to plasma skimming*. *Bull. Math. Biol.*, 1983. **45**: p. 41-50.
43. Rong, F.W. and R.T. Carr, *Dye studies on flow through branching tubes*. *Microvasc. Res.*, 1990. **26**: p. 907-920.
44. Enden, G. and A.S. Popel, *A numerical Study of plasma skimming in small vascular bifurcations*. *J. Biomech. Eng.*, 1994. **116**: p. 79-88.
45. Segre, G. and A. Silberberg, *Behavior of macroscopic rigid spheres in Poiseuille flow*. *J. Fluid Mech.*, 1962. **14**: p. 115-136.
46. Eckstein, E.C., D.C. Bailey, and A.H. Shapiro, *Self-diffusion of particles in shear flow of a suspension*. *J. Fluid Mech.*, 1977. **79**: p. 191-208.
47. Leighton, D. and A. Acrivos, *Measurement of shear-induced self-diffusion in concentrated suspensions of spheres*. *J. Fluid Mech.*, 1987. **177**: p. 109-131.
48. Abbott, J.R., *et al.*, *Experimental observations of particle migration in concentrated suspensions: Couette flow*. *J. Rheol.*, 1991. **35**: p. 773-789.
49. Leighton, D. and A. Acrivos, *The shear-induced migration of particles in concentrated suspensions*. *J. Fluid Mech.*, 1987. **181**: p. 415-439.
50. Zydney, A.L. and C.K. Colton, *Augmented solute transport in the shear flow on a concentrated suspension*. *PhysicoChem. Hydrodyn.*, 1988. **10**(1): p. 77-96.
51. Byrne, G.D., *The solution of a copolymerization model with VODE*, in *Recent Developments in Numerical Methods and Software for ODEs/DAEs/PDEs*, G.D. Byrne and W.E. Schiesser, Editors. 1992, World Scientific: Singapore. p. 137-197.
52. Richtmeyer, R.D. and K.W. Morton, *Difference Methods for Initial Problems*. 2nd. ed. 1967, New York: Interscience Publishers.
53. D'Augustino, R.B. and M.A. Stevens, *Goodness-of-Fit Techniques*. 1986: Marcel Dekker.

54. Carr, R.T., *Plasma skimming in replicas of microvascular bifurcations*, Ph. D. dissertation. 1984, University of Rochester.
55. Frame, M.D. and I.H. Sarelius, *Arteriolar bifurcation angles vary with position and when flows is changed*. *Microvasc. Res.*, 1993. **46**: p. 190-205.
56. Frame, M.D., *The in vivo data for diameter and length (Personal Communication)*.
57. Sarelius, I.H., *Cell and oxygen flow in arterioles controlling capillary perfusion*. *Am. J. Physiol.*, 1993. **265**: p. H1682-H1637.
58. Duling, B.R., *Is red cell flow heterogeneity a critical variable in the regulation and limitation of oxygen transport to tissue?*, in *Oxygen Transport to Tissue XVI*, M.C. Hogan, *et al.*, Editors. 1994, Plenum Press: New York.
59. Ellsworth, M.L., A.S. Popel, and R.N. Pittman, *Assessment and impact of heterogeneities of convective oxygen transport parameters in capillaries of striated muscle: experimental and theoretical*. *Microvascular Research*, 1988. **35**: p. 341-362.
60. Popel, A.S. and J.F. Gross, *Analysis of oxygen diffusion from arteriolar networks*. *Am J Physiol*, 1979. **237**: p. H681-H689.
61. Kanzow, G., A.R. Pries, and P. Gaehtgens, *Analysis of the hematocrit distribution in the mesenteric microcirculation*. *Int. J. Microcirc. Clin. Exp.*, 1982. **1**: p. 67-69.
62. Weibel, E.R., *The Pathway for Oxygen*. 1984, Cambridge, MA: Harvard University Press.
63. Sweeney, T.E. and I.H. Sarelius, *Arteriolar control of capillary cell flow in striated muscle*. *Circulation Research*, 1989. **64**(1): p. 112-120.
64. Pries, A.R., *et al.*, *Redistribution of red blood cell flow in microcirculatory networks by hemodilution*. *Circulation Research*, 1992. **70**(6): p. 1113-1121.
65. Duling, B.R. and D.H. Damon, *An examination of the measurement of flow heterogeneity in striated muscle*. *Circulation Research*, 1987. **60**: p. 1-13.
66. Damon, D.H. and B.R. Duling, *Evidence that capillary perfusion heterogeneity is not controlled in striated muscle*. *Am. J. Physiol.*, 1986. **248**: p. H386-H392.
67. Tyml, K. and K. Mikulash, *Evidence for increased perfusion heterogeneity in skeletal muscle during reduced flow*. *Microvasc. Res.*, 1988. **35**: p. 316-324.

68. Tymk, K., *Red cell perfusion in skeletal muscle at rest and after mild and severe contractions*. Am. J. Physiol., 1987. **252**: p. H485-H493.
69. Bassingthwaite, J.B., L.S. Liebovitch, and B.J. West, *Fractal Physiology*. 1994, New York: Oxford University Press.
70. Mandelbrot, B.B., *The Fractal Geometry of Nature*. 1982, San Francisco: Freeman.
71. Glenny, R. and H.T. Robertson, *Fractal properties of pulmonary blood flow: characterization of spatial heterogeneity*. J. Applied Physiol., 1990. **69**: p. 532-545.
72. Gaehtgens, P., K. Ley, and A.R. Pries, *Topological approach to the analysis of microvessel structure and hematocrit distribution*, in *Microvascular Networks: Experimental and Theoretical Studies*, A.S. Popel and P.C. Johnson, Editors. 1986, Karger: Basel. p. 52-60.

NOMENCLATURE

a: The particle radius.

D: The effective particle dispersion coefficient, or fractal dimension.

d: Vessel diameter.

g: The plasma gap thickness.

H: Hematocrit.

H_c : core hematocrit.

H_{mv} : Hematocrit in microvessel.

H_T : The tube hematocrit.

H_F : The feeding hematocrit.

H_D : The discharge hematocrit.

$(R_b)_\alpha$: The bifurcation ratio of order α .

L_α : The length of order α .

D_α : The diameter of order α .

F^* : The ratio of side branch to main vessel red blood cell flux.

Q^* : The ratio of side branch to main vessel volumetric flow.

R: The vessel radius.

L: The vessel length.

R_c : The red blood cell radius.

P_e : The Peclet number.

F_{RBC} : The total red blood cell mass.

Q: The volumetric flow rate.

ΔP : The pressure drop.

Q: The vector of blood flow.

H: The vector of hematocrit.

R: The vector of red blood cell flow.

M_v : The magnitude of heterogeneity.

RD(m): The coefficient of variation for sample m.

V: The blood velocity profile.

Z: The axial coordinate.

$\overline{\Delta R^2}$: The mean square displacement.

Δt : The time between observations.

m: The fictitious body force.

u: The average blood velocity divided by the vessel diameter.

Greek letter:

γ : Shear rate.

θ : The angular coordinate.

η : The dimensionless axial coordinate.

ξ : The dimensionless radial coordinate.

δ : The dimensionless plasma gap thickness.

ϕ : The ratio of core viscosity to gap viscosity.

ω : The parameter in velocity profile expression.

μ_p : The plasma viscosity.

α : The parameter in velocity profile expression.

β : The parameter in velocity profile expression.

APPENDIX A

COMPUTER PROGRAM

The following FORTRAN 77 program is used to F^* , the ratio of red blood cell flux in the side branch to that in the parent vessel, in variable dispersion model.

```
c      variable diffusivity coefficient, two-phase velocity profile.
      program main
      implicit double precision (a-h,o-z)
      parameter (ni=48,nj=48,dz=0.05)
      dimension h(ni+1,-1:nj),hd(ni+1,-1:nj),r(ni+1),theta(nj+1)
      dimension h1(ni+1,-1:nj)
      common beta,delta,pi,d,k
      pi=4.0*atan(1.0)
      d=0.02
      dc=8.0
      coef=0.15
      exx=0.8
c      open (unit=10,file='d10.dat',status='old')
c      read (10,*) ind,k,delta
c      close (10)
      ind=2
      k=2
      sumf=0.0
      kk=k
      open (unit=7,file='both10.dat',status='new')
      open (unit=9,file='exper.dat',status='old')
2     read (9,*) bl1,a1,t1,h1,bl2,a2,t2,h2,bl3,a3,t3,h3,dt,hf,z
      t1=100.*t1-40.*aint(t1)
      t2=100.*t2-40.*aint(t2)
      t3=100.*t3-40.*aint(t3)
      q1=(bl1*a1/t1)/(bl1*a1/t1+bl2*a2/t2+bl3*a3/t3)
      q2=(bl2*a2/t2)/(bl2*a2/t2+bl3*a3/t3)
      fe2=(h2*bl2*a2/t2)/(h2*bl2*a2/t2+h3*bl3*a3/t3)
      hf=(h2*bl2*a2/t2+h3*bl3*a3/t3)/(bl2*a2/t2+bl3*a3/t3)
      delta=dc/dt
```

```

if (ind .eq. 2) then
  delta=dc/dt
  ubar=4.d09*(bl2*a2/t2+bl3*a3/t3)/(pi*dt**3.)
  fld=visrat(delta,hf,ubar)
  beta=(1.-delta)**2.+(1.-(1.-delta)**2)*fld
  alpha=2./(fld+(1.-fld)*(1.-delta)**4.)
  else
  beta=1.
  alpha=float(k+2)/float(k)
  end if
  pe=alpha*(dt/dc)**2./(4.*coef*hf*(1.-hf)**exx)
  dr=(1.0-delta)/float(ni)
  dtheta=2.0*pi/float(nj)
  z=z/dt*2000.

  do 100 i=1,ni+1
    r(l)=float(i-1)*dr
    continue
  do 200 j=0,nj
    theta(j+1)=float(j)*dtheta
    continue
  do 300 i=1,ni+1
    do 400 j=0,nj-1
      h(i,j)=1.0
    continue
  continue
  epsilon=coord(q1)
  do 500 i=1,ni+1
    rr=r(i)
    do 600 j=0,nj-1
      the=theta(j+1)
      call map(rr,the,epsilon,r1,theta1)
      if (r1 .gt. 1.-delta) then
        hh=0.0
        goto 550
      end if
      if (r1 .le. dR) then
        kkk=1
        goto 530
      end if
      call locate(r,ni+1,r1,kkk)
530    call locate(theta,nj+1,theta1,jj)
      call bilineaR(h,kkk,jj,r,theta,r1,theta1,hh)
550    hd(i,j)=hh

```

```

600     continue
500     continue
c      *****
c      The range of calculation
c      *****
      ka=0
10     zend=dz*ka
      if (zend .gt. z) goto 1200
      call adi(hd,ni,nj,delta,dz,dr,pe,beta,kk,dtheta)
      ka=ka+1
      goto 10
1200    continue
      call rot(hd,180,nj,ni,h1)
      do 650 i=1,ni+1
      do 680 j=0,nj-1
      h(i,j+1)=h1(i,j)
680    continue
650    continue
      epsilon2=coord(q2)
      fstart=fnum(epsilon2,beta,delta,k,h,nj,ni+1)
      sumf=sumf+(fstart-fe2)**2
      if (bl1 .eq. 35.56) then
      close (7)
      goto 1300
      else
      write (7,*) fstart,fe2
      goto 2
      end if
1300   open (unit=8,file='compare10.dat',status='new')
      write (8,*) sumf,fstart,fe2
      close (8)
      end

      subroutine bilinear(h,k,j,rd,thetad,r1,theta1,hH)
      double precision h(49,-1:48),rd(49),thetad(49)
      double precision r1,theta1,t,U,hh
      integer k,j
      nj=48
      t=(theta1-thetad(j))/(thetad(j+1)-thetad(j))
      u=(r1-rd(k))/(rd(k+1)-rd(k))
      if (j .eq. nj) then
      h(k,nj)=h(k,0)
      h(k+1,nj)=h(k+1,0)
      end if

```

```

    if (k .eq. 1) then
      hh=(1.-t)*h(k,j-1)+t*(1.-u)*h(k,j)+t*u*h(k+1,j)
    else
      hH=(1.-t)*(1.-u)*h(k,j-1)+t*(1.-u)*h(k,j)+t*u*
& h(k+1,j)+(1.-t)*u*h(k+1,j-1)
    end if
    return
  end

```

```

subroutine locate(xx,n,x,j)
double precision xx(n),x
integer n,j
jl=0
ju=n+1
10  if(ju-jl.gt.1)then
    jm=(ju+jl)/2
    if((xx(n).gt.xx(1)).eqv.(x.gt.xx(jm)))then
      jl=jm
    else
      ju=jm
    endif
    go to 10
  endif
  j=jl
  return
end

```

```

function visrat (delta,hfeed,u)
double precision delta, hfeed, fld, fld1
double precision a, g, visrat, qtot, ftot, hcore, u, c
c=0.12
if (u .lt. 50.) c=0.13
if (u .lt. 30.) c=0.14
if (u .lt. 17.) c=0.15
if (u .lt. 3.) c=0.14
if (u .lt. 1.) c=0.16
fld1=1.
fld=0.
g=1.0-delta
60  if (dabs(1.-fld/fld1) .gt. 0.001) then
    fld=fld1
    a=g*g+(1-g*g)*fld
    ftot=a*g*g/2.-g**4./4.
    qtot=ftot+fld*(0.25-(g*g/2.-g**4./4.))
    hcore=hfeed*qtot/ftot

```

```

fld1=exp(4.2*hcore/(u**c))
go to 60.
endif
visrat=fld
return
end

```

```

subroutine MAP (R, THETA, epsilon, r1, theta1)
double precision theta, r, theta1, r1, x, y
double precision epsilon, qstar, dx, dy, dqxc, dqyk
double precision qx, qy, x1, y1, x2, y2, q, qyc
double precision qxc, qyk, f1, f2, f3, y3, x3, arg, pi
integer knx, kny
external qstar, partq, qyc
pi=4d0*datan(1d0)
y=r*sin(theta)
x=r*cos(theta)
qx=1.-qstar(x)
q=1.-qstar(epsilon)
knx=0
x2=(epsilon-1.00)/2.000
x1=2000.
900 if (abs(x1-x2) .gt. 1d-05) then
knx=knx+1
if (knx .le. 10) then
x1=x2
qxc=(1.-qstar(x1))/q
dx=x1+1d-03
dqxc=((1.-qstar(dx))/q-qxc)/1d-03
x2=x1+(qx-qxc)/dqxc
x3=x2
if (abs(x2) .gt. 1.) knx=11
goto 900
end if
end if
if (knx .gt. 10) then
x1=epsilon
x2=-1.
f1=(1.-qstar(x1))/q-qx
f2=(1.-qstar(x2))/q-qx
end if
800 x3=(x1+x2)/2.
f3=(1.-qstar(x3))/q-qx
if ((abs(x1-x3).lt.1d-05).or.(abs(x2-x3).lt.1d-05)) then
x1=x3

```

```

else
  knx=knx+1
  if (f3*f1 .lt. 0.) then
    x2=x3
    f2=f3
    go to 800
  else if (f2*f3 .lt. 0.) then
    x1=x3
    f1=f3
    go to 800
  end if
end if
if (dabs(y) .le. 1d-05) then
  y1=0d0
else
  qy=qstar(y)
  y1=1.00
  y2=0.
  kny=0
100  if (abs(y1-y2) .gt. 1d-05) then
      kny=kny+1
      if ( kny .le. 10) then
        y1=y2
        qyk=qyc(y1,epsilon)
        dy=y1+1d-03
        dqyk=(qyc(dy,epsilon)-qyk)/1d-03
        y2=y1+(qy-qyk)/dqyk
        if (abs(y2) .gt. 1.) y2=sign(.999d0,y2)
        goto 100
      end if
    end if
  if (kny .gt. 10) then
    y1=1.0
    y2=-1.0
    f1=qyc(y1,epsilon)
    f2=qyc(y2,epsilon)
  end if
801  y3=(y1+y2)/2.
      f3=qyc(y3,epsilon)
      if ((abs(y1-y3).lt.1d-05).or.(abs(y2-y3).lt.1d-05)) then
        y1=y3
      else
        kny=kny+1
        if((f3*f1) .lt. 0.) then
          y2=y3

```



```

    f2=f3
    go to 801
else if ((f3*f2) .lt. 0.) then
    y1=y3
    f1=f3
    go to 801
endif
endif
end if
arg=datan2(dabs(y1),dabs(x1))
if ((x1.gt.0) .and. (y1.gt.0)) theta1=arg
if ((x1.lt.0) .and. (y1.gt.0)) theta1=pi-arg
if ((x1.lt.0) .and. (y1.lt.0)) theta1=pi+arg
if ((x1.gt.0) .and. (y1.lt.0)) theta1=2*pi-arg
if ((x1.ge.0d0) .and. (y1.eq.0d0)) theta1=0.
if ((x1.lt.0d0) .and. (y1.eq.0d0)) theta1=pi
r1=dsqrt(x1*x1+y1*y1)
return
end

```

```

function QYC (y,epsilon)
real*8 qyc,y,epsilon,yc,partq
if (y .lt. 0) then
    yc=dabs(y)
    qyc=1.-partq(yc,epsilon)
else
    qyc=partq(y,epsilon)
endif
return
end

```

```

function partq (y,x)
double precision beta,delta,pi
double precision d,term
double precision x,y,r,theta1,theta2,hold,dr,rr,qq
double precision fld,qtot,p,partq,top,denom,qstar
integer nr,i,k
common beta,delta,pi,d,k
external qstar
if (y .lt. 1.d-05) then
    partq=0.5
else
if (delta .ne. 0.) then
fld=(beta-(1.-delta)**2.)/(1.-(1.-delta)**2.)
else

```

```

fld=1.
end if
p=1.-delta
qtot=(beta*p**2./2.-p**(k+2.)/(k+2.)+fld*(0.5-1./(k+2.)
$ -p**2./2.+p**(k+2.)/(k+2.)))*2.*pi
denom=1.-qstar(x)
qq=0.
top=qstar(y)
r=sqrt(x*x+y*y)
hold=0.
if (r .le. 1) then
if (r .le. 1.-delta) then
nr=(1.-delta-r)/d
nr=nr+nr+2
dr=(1.-delta-r)/nr
do 20 i=1,nr+1
rr=r+dr*(i-1)
if (x .gt. 0) then
theta1=atan2(y,sqrt(rr*rr-y*y))
theta2=atan2(sqrt(rr*rr-x*x),x)
else if ((x.eq.0.).and.(y.eq.0.)) then
theta1=0.
theta2=pi/2.
else if ((x.eq.0.).and.(y.ne.0.)) then
theta1=atan2(y,sqrt(rr*rr-y*y))
theta2=pi/2.
else
theta1=atan2(sqrt(rr*rr-x*x),x)
theta2=atan2(y,-sqrt(rr*rr-y*y))
end if
term=rr*(beta-rr**k)*(theta2-theta1)
if (mod(i,2) .eq. 0.) then
hold=hold+4.*term
else
hold=hold+2.*term
end if
if ((i .eq. 1) .or. (i .eq. nr+1)) then
hold=hold-term
end if
continue
qq=hold*dr/3.
r=1.-delta
endif
nr=(1.-r)/d
nr=nr+nr+2

```

20

```

dr=(1.-r)/nr
hold=0.
do 30 i=1,nr+1
rr=r+dr*(i-1)
if (x .gt. 0) then
  theta1=atan2(y,sqrt(rr*rr-y*y))
  theta2=atan2(sqrt(rr*rr-x*x),x)
else if ((x.eq.0.).and.(y.eq.0.)) then
  theta1=0.
  theta2=pi/2.
else if ((x.eq.0.).and.(y.ne.0.)) then
  theta1=atan2(y,sqrt(rr*rr-y*y))
  theta2=pi/2.
else
  theta1=atan2(sqrt(rr*rr-x*x),x)
  theta2=atan2(y,-sqrt(rr*rr-y*y))
end if
term=rr*fld*(1.-rr**k)*(theta2-theta1)
if (mod(i,2) .eq. 0.) then
  hold=hold+4.*term
else
  hold=hold+2.*term
end if
if ((i .eq. 1) .or. (i .eq. nr+1)) then
  hold=hold-term
end if
30 continue
qq=qq+hold*dr/3.
qq=qq/qtot
if (x .ge. 0.) then
  partq=(top-qq)/(denom)
else
  partq=qq/(denom)
end if
else if (x .lt. 0.) then
c write (6,*) 'there is no answer',x,y
else
  partq=(top)/denom
end if
end if
return
end

function qstar (epsilon)
double precision beta,delta,pi

```

```

double precision d, fld
double precision epsilon, x1, x2, x3, y1, y2, y3
double precision dx, qtot, qhold, startx, qstar, arccos
integer k, i, nx
common beta, delta, pi, d, k
external arccos
if (epsilon .ge. 1.) then
    qstar=0.0
    return
else if (epsilon .le. -1.) then
    qstar=1.0
    return
end if
if (delta .eq. 0) then
    fld=1.
else
    fld=(beta-(1.-delta)**2.)/(1.-(1.-delta)**2.)
endif
if (delta-1.-epsilon .gt. 0) then
    qhold=0.
    nx=(1.0-dabs(epsilon))/d
    nx=nx+nx+2
    dx=(1.0-dabs(epsilon))/nx
    startx=dabs(epsilon)
    goto 1000
endif
if (delta-1.+epsilon .gt. 0) then
    qhold=2*pi*(beta*(1.-delta)**2./2.-(1.-delta)**(k+2)/(k+2))
    qhold=qhold+fld*2.*pi*((epsilon**2.-(1.-delta)**2.)/2.)
    qhold=qhold-fld*2.*pi*((epsilon**(k+2)-(1.-delta)**(k+2))
%   /(k+2))
    nx=(1.0-dabs(epsilon))/d
    nx=nx+nx+2
    dx=(1.0-dabs(epsilon))/nx
    startx=dabs(epsilon)
    goto 1000
endif
if (epsilon .gt. 0 ) then
    qhold=2.*pi*(beta*epsilon**2./2.-epsilon**(k+2)/(k+2))
else
    qhold=0.
endif
nx=(1.0-delta-dabs(epsilon))/d
nx=nx+nx+2
dx=(1.0-delta-dabs(epsilon))/nx

```

```

do 700 i=1,nx,2
x1=dabs(epsilon)+(i-1)*dx
x2=x1+dx
x3=x2+dx
y1=(beta-x1**k)*x1*(2.*pi-2.*arccos(epsilon,x1))
y2=(beta-x2**k)*x2*(2.*pi-2.*arccos(epsilon,x2))
y3=(beta-x3**k)*x3*(2.*pi-2.*arccos(epsilon,x3))
qhold=qhold+(y1+4*y2+y3)*dx/3.
700  continue
nx=delta/d
nx=nx+nx+2
dx=delta/nx
startx=1.-delta
1000 continue
do 800 i=1,nx,2
x1=startx+(i-1)*dx
x2=x1+dx
x3=x2+dx
y1=fld*(1.-x1**k)*x1*(2.*pi-2.*arccos(epsilon,x1))
y2=fld*(1.-x2**k)*x2*(2.*pi-2.*arccos(epsilon,x2))
y3=fld*(1.-x3**k)*x3*(2.*pi-2.*arccos(epsilon,x3))
qhold=qhold+(y1+4*y2+y3)*dx/3.
800  continue
qtot=(beta*(1.-delta)**2./2.-(1.-delta)**(k+2.)/(k+2.))
qtot=(qtot+fld*(0.5-1./(k+2.)-(1.-delta)**2./2.+
% (1.-delta)**(k+2.)/(k+2.)))*2.*pi
qstar=1.-qhold/qtot
return
end
function arccos (epsilon,xsi)
double precision epsilon,xsi,pi,arccos
if (dabs(epsilon) .gt. xsi) then
stop
endif
pi=4.*datan(1.d0)
if ( (epsilon .eq. 0.) .and. (xsi .ge. 0.) ) then
arccos = pi/2.
return
endif
arccos=dacos(epsilon/xsi)
return
end

function coord (qx)
double precision beta,delta,pi

```

```

double precision d
double precision x,x2,qx,qh,qstar,coord,x1,qh1,qh2
integer k
common beta,delta,pi,d,k
external qstar
x1=1.d00
x2=-1.d00
x=0.0d00
qh1=0.-qx
qh2=1.0-qx
30 qh=qstar(x)-qx
if (abs(qh) .gt. 1d-05) then
if (dabs(x-x1) .ge. 1d-05) then
if (qh*qh1 .lt. 0.) then
x2=x
qh2=qh
else
x1=x
qh1=qh
end if
x=(x1+x2)/2.
go to 30
end if
end if
coord=x
return
end
c *****
subroutine adi(h,ni,nj,delta,dz,dr,pe,beta,kk,dtheta)
double precision h(49,-1:48),r(49),t(48,48),e(49)
double precision dd(49),bb(49),cc(49),ee(49)
double precision delta,dz,dr,pe,beta,hh,dtheta,hs
integer kpvt(49),info,kk
c *****
c radial direction for adi
c *****
do 10 j=0,nj-1
if (j .eq. 0) then
h(2,j-1)=h(2,nj-1)
end if
if (j .eq. nj-1) then
h(2,j+1)=h(2,0)
end if
h(1,j)=dz/beta/pe/2.0*(2.0*(h(2,j)-h(1,j))/dr+
& (h(2,j+1)+h(2,j-1)-

```

```

      &      2.0*h(2,j))/dr/dtheta**2)+h(1,j)
c      h(1,j)=dz/(pe*dtheta*dr*(beta-(dr/2.)**kk))*
c      &      (dtheta*(h(2,j)-h(1,j))+(h(1,j+1)-2.*h(1,j)
c      &      +h(1,j-1))*2./dtheta)+h(1,j)
10     continue
c      *****
c      r direction, assign the coeff.
      do 20 j=0,nj-1
      do 30 i=3,ni+1
      r(i)=float(i-1)*dr
      if (i .eq. ni+1) then
      bb(i-1)=-2.0*r(i)/dr**2
      else
      bb(i-1)=1.0/dr-r(i)/dr**2
      end if
30     continue

      do 35 i=2,ni+1
      r(i)=float(i-1)*dr
      cc(i-1)=2.0*r(i)/dr**2+2.0*pe*(beta-r(i)**kk)/dz
35     continue

      do 40 i=2,ni
      r(i)=float(i-1)*dr
      dd(i-1)=-(r(i)/dr**2+1.0/dr)
40     continue

      do 50 i=2,ni+1
      if (j .eq. 0) then
      h(i,j-1)=h(i,nj-1)
      end if
      if (j .eq. nj-1) then
      h(i,j+1)=h(i,0)
      end if
      r(i)=float(i-1)*dr
c      r(i)=(float(i)-0.5)*dr
      if (i .eq. 2) then
      ee(i-1)=(h(i,j+1)-2.0*h(i,j)+h(i,j-1))/r(i)/dtheta**2
      &      +h(i,j)*2.0*pe*(beta-r(i)**kk)/dz-h(i-1,j)*
      &      (1.0/dr-r(i)/dr**2)
      else
      ee(i-1)=(h(i,j+1)-2.0*h(i,j)+h(i,j-1))/r(i)/dtheta**2
      &      +h(i,j)*2.0*pe*(beta-r(i)**kk)/dz
      end if
50     continue

```

```

        call dgtsl(ni,bb,cc,dd,ee,info)
        do 60 i=2,ni+1
        h(i,j)=ee(i-1)
60      continue
20      continue
c      *****
c      theta direction for adi
        do 70 j=0,nj-1
        if (j .eq.0) then
        h(2,j-1)=h(2,nj-1)
        end if
        if (j .eq. nj-1) then
        h(2,j+1)=h(2,0)
        end if
        h(1,j)=dz/beta/pe/2.0*(2.0*(h(2,j)-h(1,j))/dr+
&          (h(2,j+1)+h(2,j-1)-
&          2.0*h(2,j))/dr/dtheta**2)+h(1,j)
c      h(1,j)=dz/(pe*dtheta*dr*(beta-(dr/2.)**kk))
c      &      *(dtheta*(h(2,j)-h(1,j))+(h(1,j+1)-2.*h(1,j)
c      &      +h(1,j-1))*2./dtheta)+h(1,j)
70      continue
        do 80 i=2,ni+1
        r(i)=float(i-1)*dr
c      r(i)=(float(i)-0.5)*dr
        do 90 jj=1,nj
        t(jj,jj)=2.0/r(i)/dtheta**2+2.0*pe*(beta-r(i)**kk)/dz
        if (jj .eq. nj) goto 90
        t(jj,jj+1)=-1.0/r(i)/dtheta**2
90      continue
        t(1,nj)=-1.0/r(i)/dtheta**2
        call dsifa(t,nj,nj,kpvt,info)
        do 110 jj=1,nj
        if (i .eq. ni+1) then
        e(jj)=r(i)*2.0/dr**2*(h(i-1,jj-1)-h(i,jj-1))
&          +h(i,jj-1)*2.0*pe*(beta-r(i)**kk)/dz
        else
        e(jj)=r(i)/dr**2*(h(i-1,jj-1)-
&          2.0*h(i,jj-1)+h(i+1,jj-1))+1.0/dr*
&          (h(i+1,jj-1)-h(i-1,jj-1))+
&          h(i,jj-1)*2.0*pe*(beta-r(i)**kk)/dz
        end if
110      continue
        call dsisl(t,nj,nj,kpvt,e)
        do 120 j=0,nj-1

```



```

        h(i,j)=e(j+1)
120      continue
80       continue
        hh=0.0
c        hs=0.0
        do 150 j=0,nj-1
        hh=hh+h(1,j)
c        hs=hs+h(2,j)
150      continue
        do 160 j=0,nj-1
        h(1,j)=hh/float(nj)
c        h(1,j)=(4.0*hh-hs)/3.0/float(nj)
160      continue
        return
        end

```

```

subroutine dgtsl(n,c,d,e,b,info)
integer n,info
double precision c(1),d(1),e(1),b(1)
integer k,kb,kp1,nm1,nm2
double precision t
info = 0
c(1) = d(1)
nm1 = n - 1
if (nm1 .lt. 1) go to 40
d(1) = e(1)
e(1) = 0.0d0
e(n) = 0.0d0
do 30 k = 1, nm1
kp1 = k + 1

if (dabs(c(kp1)) .lt. dabs(c(k))) go to 10
t = c(kp1)
c(kp1) = c(k)
c(k) = t
t = d(kp1)
d(kp1) = d(k)
d(k) = t
t = e(kp1)
e(kp1) = e(k)
e(k) = t
t = b(kp1)
b(kp1) = b(k)
b(k) = t
10      continue

```

```

        if (c(k) .ne. 0.0d0) go to 20
        info = k
20      go to 100
        continue
        t = -c(kp1)/c(k)
        c(kp1) = d(kp1) + t*d(k)
        d(kp1) = e(kp1) + t*e(k)
        e(kp1) = 0.0d0
        b(kp1) = b(kp1) + t*b(k)
30      continue
40      continue
        if (c(n) .ne. 0.0d0) go to 50
        info = n
        go to 90
50      continue

        nm2 = n - 2
        b(n) = b(n)/c(n)
        if (n .eq. 1) go to 80
        b(nm1) = (b(nm1) - d(nm1)*b(n))/c(nm1)
        if (nm2 .lt. 1) go to 70
        do 60 kb = 1, nm2
            k = nm2 - kb + 1
            b(k) = (b(k) - d(k)*b(k+1) - e(k)*b(k+2))/c(k)
60      continue
70      continue
80      continue
90      continue
100     continue
        return
        end

subroutine dsifa(a,lda,n,kpvt,info)
integer lda,n,kpvt(1),info
double precision a(lda,1)
double precision ak,akm1,bk,bkm1,denom,mulk,mulkm1,t
double precision absakk,alpha,colmax,rowmax
integer imax,imaxp1,j,jj,jmax,k,km1,km2,kstep,idamax
logical swap

alpha = (1.0d0 + dsqrt(17.0d0))/8.0d0
info = 0
k = n
10     continue

```

```

if (k .eq. 0) go to 200
  if (k .gt. 1) go to 20
  kpvt(1) = 1
  if (a(1,1) .eq. 0.0d0) info = 1

  go to 200
20  continue
  km1 = k - 1
  absakk = dabs(a(k,k))
  imax = idamax(k-1,a(1,k),1)
  colmax = dabs(a(imax,k))
  if (absakk .lt. alpha*colmax) go to 30
  kstep = 1
  swap = .false.
  go to 90
30  continue
  rowmax = 0.0d0
  imaxp1 = imax + 1
  do 40 j = imaxp1, k
    rowmax = dmax1(rowmax,dabs(a(imax,j)))
40  continue
  if (imax .eq. 1) go to 50
  jmax = idamax(imax-1,a(1,imax),1)
  rowmax = dmax1(rowmax,dabs(a(jmax,imax)))
50  continue
  if (dabs(a(imax,imax)) .lt. alpha*rowmax) go to 60
  kstep = 1
  swap = .true.
  go to 80
60  continue
  if (absakk .lt. alpha*colmax*(colmax/rowmax)) go to 70
  kstep = 1
  swap = .false.
  go to 80
70  continue
  kstep = 2
  swap = imax .ne. km1
80  continue
90  continue
  if (dmax1(absakk,colmax) .ne. 0.0d0) go to 100
c
c  column k is zero. set info and iterate the loop.
c
  kpvt(k) = k
  info = k

```

```

    go to 190
100  continue
    if (kstep .eq. 2) go to 140

    if (.not.swap) go to 120

        call dswap(imax,a(1,imax),1,a(1,k),1)
        do 110 jj = imax, k
            j = k + imax - jj
            t = a(j,k)
            a(j,k) = a(imax,j)
            a(imax,j) = t
110     continue
120     continue

        do 130 jj = 1, km1
            j = k - jj
            mulk = -a(j,k)/a(k,k)
            t = mulk
            call daxpy(j,t,a(1,k),1,a(1,j),1)
            a(j,k) = mulk
130     continue

        kpvt(k) = k
        if (swap) kpvt(k) = imax
        go to 190
140     continue
        if (.not.swap) go to 160

        call dswap(imax,a(1,imax),1,a(1,k-1),1)
        do 150 jj = imax, km1
            j = km1 + imax - jj
            t = a(j,k-1)
            a(j,k-1) = a(imax,j)
            a(imax,j) = t
150     continue
        t = a(k-1,k)
        a(k-1,k) = a(imax,k)
        a(imax,k) = t
160     continue

        km2 = k - 2
        if (km2 .eq. 0) go to 180
        ak = a(k,k)/a(k-1,k)
        akm1 = a(k-1,k-1)/a(k-1,k)
        denom = 1.0d0 - ak*akm1

```

```

do 170 jj = 1, km2
  j = km1 - jj
  bk = a(j,k)/a(k-1,k)
  bkm1 = a(j,k-1)/a(k-1,k)
  mulk = (akm1*bk - bkm1)/denom
  mulkm1 = (ak*bkm1 - bk)/denom
  t = mulk
  call daxpy(j,t,a(1,k),1,a(1,j),1)
  t = mulkm1
  call daxpy(j,t,a(1,k-1),1,a(1,j),1)
  a(j,k) = mulk
  a(j,k-1) = mulkm1
170  continue
180  continue

```

```

kpvt(k) = 1 - k
  if (swap) kpvt(k) = -imax
  kpvt(k-1) = kpvt(k)
190  continue
k = k - kstep
go to 10
200  continue
return
end

```

```

subroutine daxpy(n,da,dx,incx,dy,incy)
double precision dx(1),dy(1),da
integer i,incx,incy,ix,iy,m,mp1,n
if(n.le.0)return
if (da .eq. 0.0d0) return
if(incx.eq.1.and.incy.eq.1)go to 20

ix = 1
iy = 1
if(incx.lt.0)ix = (-n+1)*incx + 1
if(incy.lt.0)iy = (-n+1)*incy + 1
do 10 i = 1,n
  dy(iy) = dy(iy) + da*dx(ix)
  ix = ix + incx
  iy = iy + incy
10  continue
return

20  m = mod(n,4)
  if( m .eq. 0 ) go to 40

```

```

do 30 i = 1,m
dy(i) = dy(i) + da*dx(i)
30 continue
if( n .lt. 4 ) return
40 mp1 = m + 1
do 50 i = mp1,n,4
dy(i) = dy(i) + da*dx(i)
dy(i + 1) = dy(i + 1) + da*dx(i + 1)
dy(i + 2) = dy(i + 2) + da*dx(i + 2)
dy(i + 3) = dy(i + 3) + da*dx(i + 3)
50 continue
return
end

```

```

subroutine dswap (n,dx,incx,dy,incy)
double precision dx(1),dy(1),dtemp
integer i,incx,incy,ix,iy,m,mp1,n
if(n.le.0)return
if(incx.eq.1.and.incy.eq.1)go to 20

```

```

ix = 1
iy = 1
if(incx.lt.0)ix = (-n+1)*incx + 1
if(incy.lt.0)iy = (-n+1)*incy + 1
do 10 i = 1,n
dtemp = dx(ix)
dx(ix) = dy(iy)
dy(iy) = dtemp
ix = ix + incx
iy = iy + incy
10 continue
return
20 m = mod(n,3)
if( m .eq. 0 ) go to 40
do 30 i = 1,m
dtemp = dx(i)
dx(i) = dy(i)
dy(i) = dtemp
30 continue
if( n .lt. 3 ) return
40 mp1 = m + 1
do 50 i = mp1,n,3
dtemp = dx(i)
dx(i) = dy(i)
dy(i) = dtemp

```

```

    dtemp = dx(i + 1)
    dx(i + 1) = dy(i + 1)
    dy(i + 1) = dtemp
    dtemp = dx(i + 2)
    dx(i + 2) = dy(i + 2)
    dy(i + 2) = dtemp
50  continue
    return
    end

integer function idamax(n,dx,incx)
double precision dx(1),dmax
integer i,incx,ix,n
c
    idamax = 0
    if( n.lt.1 .or. incx.le.0 ) return
    idamax = 1
    if(n.eq.1)return
    if(incx.eq.1)go to 20
    ix = 1
    dmax = dabs(dx(1))
    ix = ix + incx
    do 10 i = 2,n
    if(dabs(dx(ix)).le.dmax) go to 5
    idamax = i
    dmax = dabs(dx(ix))
5    ix = ix + incx
10   continue
    return

20   dmax = dabs(dx(1))
    do 30 i = 2,n
    if(dabs(dx(i)).le.dmax) go to 30
    idamax = i
    dmax = dabs(dx(i))
30   continue
    return
    end

subroutine dsisl(a,lda,n,kpvt,b)
integer lda,n,kpvt(1)
double precision a(lda,1),b(1)
double precision ak,akm1,bk,bkm1,ddot,denom,temp
integer k,kp

```

```

k = n
10  if (k .eq. 0) go to 80
    if (kpvt(k) .lt. 0) go to 40

    if (k .eq. 1) go to 30
    kp = kpvt(k)
    if (kp .eq. k) go to 20

    temp = b(k)
    b(k) = b(kp)
    b(kp) = temp
20  continue

    call daxpy(k-1,b(k),a(1,k),1,b(1),1)
30  continue

    b(k) = b(k)/a(k,k)
    k = k - 1
    go to 70
40  continue
if (k .eq. 2) go to 60
    kp = iabs(kpvt(k))
    if (kp .eq. k - 1) go to 50
temp = b(k-1)
    b(k-1) = b(kp)
    b(kp) = temp
50  continue

    call daxpy(k-2,b(k),a(1,k),1,b(1),1)
    call daxpy(k-2,b(k-1),a(1,k-1),1,b(1),1)
60  continue

    ak = a(k,k)/a(k-1,k)
    akm1 = a(k-1,k-1)/a(k-1,k)
    bk = b(k)/a(k-1,k)
    bkm1 = b(k-1)/a(k-1,k)
    denom = ak*akm1 - 1.0d0
    b(k) = (akm1*bk - bkm1)/denom
    b(k-1) = (ak*bkm1 - bk)/denom
    k = k - 2
70  continue
    go to 10
80  continue

k = 1

```



```

90  if (k .gt. n) go to 160
    if (kpvt(k) .lt. 0) go to 120

    if (k .eq. 1) go to 110

    b(k) = b(k) + ddot(k-1,a(1,k),1,b(1),1)
    kp = kpvt(k)
    if (kp .eq. k) go to 100

    temp = b(k)
    b(k) = b(kp)
    b(kp) = temp
100  continue
110  continue
    k = k + 1
    go to 150
120  continue

    if (k .eq. 1) go to 140

    b(k) = b(k) + ddot(k-1,a(1,k),1,b(1),1)
    b(k+1) = b(k+1) + ddot(k-1,a(1,k+1),1,b(1),1)
    kp = iabs(kpvt(k))
    if (kp .eq. k) go to 130

    temp = b(k)
    b(k) = b(kp)
    b(kp) = temp
130  continue
140  continue
    k = k + 2
150  continue
    go to 90
160  continue
    return
    end

```

```

double precision function ddot(n,dx,incx,dy,incy)
double precision dx(1),dy(1),dtemp
integer i,incx,incy,ix,iy,m,mp1,n

```

c

```

ddot = 0.0d0
dtemp = 0.0d0
if(n.le.0)return

```

```

    iff(incx.eq.1.and.incy.eq.1)go to 20
    ix = 1
    iy = 1
    iff(incx.lt.0)ix = (-n+1)*incx + 1
    iff(incy.lt.0)iy = (-n+1)*incy + 1
    do 10 i = 1,n
        dtemp = dtemp + dx(ix)*dy(iy)
        ix = ix + incx
        iy = iy + incy
10    continue
    ddot = dtemp
    return
20    m = mod(n,5)
    iff( m .eq. 0 ) go to 40
    do 30 i = 1,m
        dtemp = dtemp + dx(i)*dy(i)
30    continue
    iff( n .lt. 5 ) go to 60
40    mp1 = m + 1
    do 50 i = mp1,n,5
        dtemp = dtemp + dx(i)*dy(i) + dx(i + 1)*dy(i + 1) +
*       dx(i + 2)*dy(i + 2) + dx(i + 3)*dy(i + 3) + dx(i + 4)*dy(i + 4)
50    continue
60    ddot = dtemp
    return
    end

```

```

function fnum (epsilon,beta,delta,k,h,NT,NR)
real*8 h(NR,NT),fpart,dt,dr,r,theta(100),pi,tstart
real*8 epsilon,beta,delta,r1,fin,ra,rb,rc,rd,theta0
real*8 fac,fact,t1,t2,ftot,fnum,tbreak
integer k,i,n,j,NT,NR,nstart,l1,l2,m
    if ((1.-delta)-abs(epsilon) .gt. 1d-05) then
        pi=4.*datan(1.d0)
        dr=(1.-delta)/(NR-1)
        dt=2.*pi/NT
        n=int(abs(epsilon)/dr)
        r=n*dr
        r1=(n+1)*dr
        fac=(abs(epsilon)-r)/(r1-r)
c    *** Integrate in theta direction first *****
c    ***** Take care of mismatch between epsilon and node *****
        theta0=0.
        if (epsilon .lt. 0.) then

```

```

do 22 j=1,NT,2
theta0=h(n+1,j)+fac*(h(n+2,j)-h(n+1,j))+
& 4*(h(n+1,j+1)+fac*(h(n+2,j+1)-h(n+1,j+1)))+
& h(n+1,j+2)+fac*(h(n+2,j+2)-h(n+1,j+2))+theta0
22 continue
theta0=theta0*dt/3.
endif

c *** Now integrate in theta direction on radial nodes *****
c *** from epsilon to 1. - delta *****

do 23 i=n+2,NR
tstart=acos(epsilon/((i-1)*dr))
m=int(tstart/dt)
theta(i)=0.
do 24 j=1,2*m,2
l=mod(NT-m+j,NT)
l1=l+1
l2=l+2
if (l .eq. 0) l=NT
if (l2 .eq. nt+1) l2=1
theta(i)=theta(i)+h(i,l)+4*h(i,l1)+h(i,l2)
24 continue
c *** Take care of mismatch in limits of theta and nodes ***
t1=m*dt
t2=(m+1)*dt
fact=(tstart-t1)/(t2-t1)
tbreak=(2*h(i,49-m)+fact*(h(i,48-m)-h(i,49-m))+2*h(i,m+1)+
& fact*(h(i,m+2)-h(i,m+1)))*dt*fact/2.
theta(i)=theta(i)*dt/3.+tbreak
23 continue
fpart=0.
if ( n+2 .le. NR-2) then
c ***** Use 3/8 simpson's rule for odd number of intervals *****
if (mod(NR-2-n,2) .eq. 1) then
ra=(n+1)*dr
rb=(n+2)*dr
rc=(n+3)*dr
rd=(n+4)*dr
nstart=n+5
fpart=(theta(n+1)*ra*(beta-ra**k)+3*theta(n+2)*rb*(beta-rb**k)
& +3*theta(n+3)*rc*(beta-rc**k)+theta(n+4)*rd*(beta-rb**k))
& *1.125
else

```

```

    fpart=0.
    nstart=n+2
    endif
    do 25 i=nstart,NR-2,2
    ra=(i-1)*dr
    rb=(i)*dr
    rc=(i+1)*dr
    fpart=fpart+theta(i)*ra*(beta-ra**k)+4*theta(i+1)*
&    (rb)*(beta-rb**k)+theta(i+2)*rc*(beta-rc**k)
25    continue
    fpart=fpart*dr/3.
    else if (n+2 .eq. NR-1) then
    ra=(n+1)*dr
    rb=(n+2)*dr
    fpart=(theta(n+3)*rb*(beta-rb**k)+theta(n+2)*ra*(beta*ra**k))
&    *dr/2.
    endif
    ra=(n+fac)*dr
    rb=(n+1)*dr
    fpart=fpart+(theta(n+2)*rb*(beta-rb**k)+theta0*ra*(beta-ra**k))
&    *(rb-ra)/2.
    fin=0.
    if (epsilon .lt. 0) then
    do 30 i=1,n
    theta(i)=0.
        do 31 j=1,NT,2
    theta(i)=2*h(i,j)+4*h(i,j+1)+theta(i)
31    continue
    theta(i)=theta(i)*dt/3.
30    continue
    if (n .ge. 2) then
    if (mod(NR-1-n,2) .eq. 1) then
    fin=(theta(2)*dr*(beta-(1*dr)**k)
&    +theta(3)*2*dr*(beta-(2*dr)**k)+theta(4)*
&    3*dr*(beta-(3*dr)**k))*1.125
    nstart=4
    else
    nstart=1
    endif
    do 35 i=nstart,n-1,2
    ra=(i-1)*dr
    rb=i*dr
    rc=(i+1)*dr
    fin=(theta(i)*ra*(beta-ra**k))+4.*(theta(i+1)*rb*(beta-rb**k))
&    +theta(i+2)*rc*(beta-rc**k)+fin

```

```

35  continue
    endif
    fin=fin*dr/3.+(theta(n+1)*n*dr*(beta-(n*dr)**k)+theta0*
&   (n+fac)*dr*(beta-((n+fac)*dr)**k))*(fac)*dr/2.
    endif
    fpart=fpart+fin
c   **** Compute total particle flow *****
    ftot=0.
    do 45 i=1,NR
    theta(i)=0.
    do 46 j=1,NT,2
    theta(i)=2*h(i,j)+4*h(i,j+1)+theta(i)
46  continue
    theta(i)=theta(i)*dt/3.
45  continue
    do 47 i=1,NR-1,2
    ra=(i-1)*dr
    rb=(i)*dr
    rc=(i+1)*dr
    ftot=theta(i)*ra*(beta-ra**k)+4*theta(i+1)*rb*(beta-rb**k)
&   +theta(i+2)*rc*(beta-rc**k)+ftot
47  continue
    ftot=ftot*dr/3.
    fnum=fpart/ftot
    else if (epsilon .lt. 0) then
    fnum=1.0
    else
    fnum=0.0
    endif
    return
    end

```

```

subroutine rot(h,ga,nj,ni,h1)
double precision h(49,-1:48),h1(49,-1:48)
integer nj,ga,ni,i,j,jn,jo,dth
do 1000 i=1,ni+1
do 1010 j=0,nj-1
dth=2*ga/15
if (j .lt. dth) then
jo=nj+j
else
jo=j
end if
jn=jo-dth
h1(i,jn)=h(i,j)

```

```

1010 continue
1000 continue
    return
    end

    subroutine rerot(h,ga,nj,ni,hd)
    double precision h(49,-1:48),hd(49,-1:48)
    integer nj,ni,ga,jn
    do 10 i=1,ni+1
    do 20 j=0,nj-1
    jn=j+2*ga/15
    if (jn .ge. nj) then
    jn=jn-nj
    end if
    hd(i,jn)=h(i,j)
20    continue
10    continue
    return
    end

```

APPENDIX B

IN VIVO DATA

The following *in vivo* data is provided by Frame [56].

Table B-1 The experimental data for vessel diameter and unbranched vessel segment.

Vessel Diameter (μm)	Unbranched Vessel Segment (μm)
22.66	152
23.01	533
33.25	114
46.35	667
46.41	114
39.21	324
36.77	171
46.28	333
41.65	105
46.14	257
29.47	714
25.91	190
31.2	886
25.22	76
25.37	171
38.57	390
33.55	714
43.77	321
51.98	221
21.41	238
59.46	286
53.31	429
39.94	905
21.99	714
43.74	57
28.43	238
30.88	543
28.54	124
37.26	171
37.65	333
37.44	267
27.24	57
21.82	152

22.72	105
30.75	457
40.78	257
32.43	95
42.89	67
37.42	429
27.19	114
24.62	86
32.62	457
31.63	381
50	210
47.61	638
31.55	257
25.38	219
31.59	705
34.09	571
34.83	381
28.75	152
26.78	552
28.24	152
38.36	248
29.56	152
26.66	124
37.04	321
25.71	221
55.92	286
49.19	429
20.05	286
22.37	238
21.1	333
21.64	619
31.89	124
31.17	600
20.18	48
20.73	171
33.25	114
31.75	210
46.92	667
49.78	114
25.69	324
27.54	333
27.44	743
26.28	171
22.05	714
21.35	267
23.12	114
23.89	86
31.1	457
28.94	381
27.94	210
27.45	181
32.37	57

APPENDIX C

IN VITRO DATA

The experimental data shown was collected by Carr and Wickham [35]. L_1 , L_2 and L_3 are the collection lengths, mm. A_1 , A_2 and A_3 are the collecting tube cross-section area, mm^2 . T_1 , T_2 and T_3 are the time for collecting blood in tube 1, 2, and 3, second. H_1 , H_2 and H_3 are the discharge hematocrit for branch 1, branch 2 and branch 3 respectively. D_t is vessel diameter, μm . H_f is the feeding hematocrit. Z is the distance between two bifurcations, mm. Figure c.1 shows the schematic of experiment for serial bifurcations.

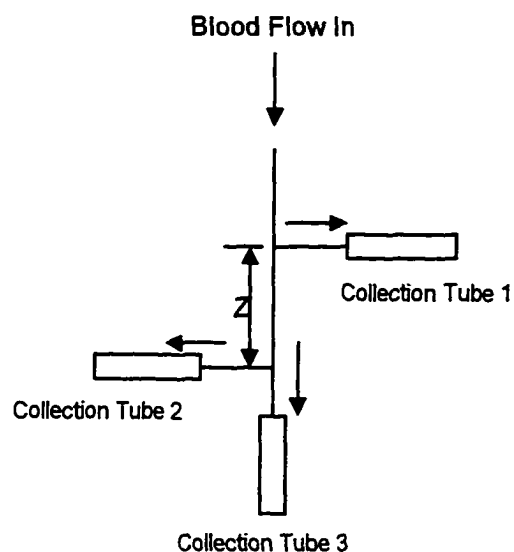


Figure C-1 The schematic of experiment for serial bifurcation.

Table C.1 The serial bifurcation experimental data.

L1	A1	T1	H1	L2	A2	T2	H2	L3	A3	T3	H3	Dt	Hf	Z
14.7	0.234	12.15	0.247	19.05	0.234	11.35	0.23	16.26	0.234	29.48	0.23	50	0.403	1.295
22.86	0.234	45.2	0.337	13.72	0.234	78.06	0.287	11.43	0.234	74.36	0.172	50	0.41	1.295
3.3	0.234	22.01	0.333	20.57	0.234	8.448	0.394	10.67	0.234	20.03	0.257	50	0.39	1.185
31.5	0.234	55.43	0.38	4.32	0.234	24.23	0.277	19.56	0.234	54.25	0.339	50	0.383	1.185
13.21	0.234	45.03	0.365	16.51	0.234	45.15	0.321	10.67	0.234	44.5	0.368	50	0.432	1.185
32	0.234	109.42	0.287	19.3	0.234	108.13	0.271	8.89	0.234	110.07	0.378	50	0.418	1.185
27.43	0.234	64.203	0.225	9.91	0.234	32.061	0.217	13.21	0.234	65.411	0.341	50	0.435	1.185
17.27	0.234	39.471	0.319	12.7	0.234	35.284	0.475	4.83	0.234	38.432	0.319	50	0.435	1.185
10.92	0.234	32.316	0.456	10.16	0.234	32.221	0.435	5.59	0.234	32.119	0.431	50	0.438	1.358
20.32	0.234	61.479	0.448	15.75	0.234	61.503	0.46	7.11	0.234	60.494	0.355	50	0.439	1.358
19.81	0.234	46.585	0.483	15.49	0.234	47.553	0.288	4.06	0.234	48.329	0.212	50	0.392	1.358
8.13	0.234	34.206	0.4	9.14	0.234	31.083	0.383	5.59	0.234	31.501	0.389	50	0.435	1.358
12.95	0.234	16.096	0.395	3.05	0.234	6.1606	0.379	9.4	0.234	15.207	0.447	50	0.434	1.358
26.16	0.234	16.43	0.365	18.29	0.234	17.029	0.369	12.45	0.234	17.079	0.316	50	0.414	1.358
12.95	0.234	13.176	0.353	9.65	0.234	10.532	0.353	15.49	0.234	13.08	0.384	50	0.416	1.016
22.35	0.234	23.331	0.372	9.14	0.234	13.523	0.349	30.23	0.234	23.399	0.386	50	0.416	1.016
20.32	0.234	19.554	0.348	9.4	0.234	12.546	0.371	29.46	0.234	19.527	0.381	50	0.415	1.016
29.72	0.234	24.513	0.381	13.72	0.234	31.074	0.394	40.13	0.234	23.592	0.442	50	0.443	1.17
22.86	0.234	19.481	0.288	8.89	0.234	20.416	0.338	35.31	0.234	19.307	0.364	50	0.446	1.17
12.95	0.234	11.2403	0.308	11.18	0.234	12.339	0.349	12.7	0.234	11.271	0.346	50	0.443	1.17
34.29	0.234	8.204	0.352	15.24	0.234	20.4581	0.3	29.21	0.234	6.493	0.375	50	0.4	1.15
44.96	0.234	32.561	0.304	4.57	0.234	39.103	0.333	59.18	0.234	29.556	0.374	50	0.397	1.15
38.35	0.234	34.134	0.334	4.302	0.234	36.163	0.265	48.51	0.234	24.41	0.389	50	0.397	1.15
20.57	0.234	18.576	0.362	27.18	0.234	18.585	0.403	13.72	0.234	20.265	0.412	50	0.43	1.15
35.81	0.234	33.132	0.322	34.29	0.234	28.435	0.354	28.7	0.234	30.116	0.342	50	0.366	1.15
19.56	0.234	18.176	0.339	21.84	0.234	17.592	0.341	18.8	0.234	18.288	0.356	50	0.365	1.15

22.35	0.234	18.563	0.348	21.84	0.234	18.555	0.315	20.57	0.234	19.033	0.361	50	0.396	1.15
22.35	0.234	20.017	0.362	22.61	0.234	20.376	0.372	24.89	0.234	20.576	0.374	50	0.387	1.15
14.99	0.234	14.17	0.318	18.8	0.234	15.521	0.347	16.26	0.234	14.177	0.37	50	0.376	1.15
25.65	0.234	31.575	0.27	44.45	0.234	31.59	0.278	11.68	0.234	32.006	0.27	50	0.376	1.15
32.77	0.234	36.307	0.268	53.34	0.234	34.174	0.316	13.21	0.234	32.213	0.248	50	0.379	1.15
50.55	0.234	54.11	0.249	57.91	0.234	33.409	0.228	14.22	0.234	54.503	0.169	50	0.379	1.15
41.91	0.234	25.109	0.346	35.05	0.234	27.35	0.333	9.91	0.234	30.393	0.313	50	0.4	1.15
9.65	0.234	8.408	0.309	7.37	0.234	16.314	0.334	6.35	0.234	7.538	0.347	50	0.4	1.15
39.12	0.234	24.291	0.326	28.7	0.234	23.489	0.298	17.02	0.234	23.292	0.336	50	0.375	1.15
32	0.234	19.453	0.296	23.88	0.234	20.586	0.284	16.26	0.234	20.159	0.33	50	0.386	1.15
25.65	0.234	18.56	0.388	18.8	0.234	19.387	0.366	16.76	0.234	18.451	0.41	50	0.389	1.15
25.4	0.234	15.48	0.328	19.81	0.234	15.581	0.324	10.92	0.234	15.557	0.367	50	0.385	1.15
42.67	0.234	28.065	0.338	36.58	0.234	28.439	0.329	16	0.234	28.309	0.371	50	0.252	1.15
50.29	0.234	32.192	0.349	46.48	0.234	32.452	0.379	15.49	0.234	33.141	0.324	50	0.393	1.15
46.23	0.234	35.394	0.352	40.89	0.234	35.383	0.326	12.45	0.234	35.342	0.477	50	0.39	1.15
25.65	0.234	40.511	0.348	65.02	0.234	39.595	0.346	9.65	0.234	40.111	0.289	50	0.394	1.15
25.4	0.234	17.043	0.325	15.75	0.234	17.227	0.299	17.78	0.234	16.568	0.343	50	0.392	1.15
37.08	0.234	21.061	0.25	18.03	0.234	21.06	0.284	24.13	0.234	22.024	0.32	50	0.4	1.15
43.18	0.234	19.551	0.276	15.49	0.234	20.364	0.286	20.07	0.234	18.513	0.29	50	0.364	1.15
36.07	0.234	26.409	0.284	15.75	0.234	26.564	0.245	32.5	0.234	26.122	0.322	50	0.364	1.15
40.13	0.234	23.173	0.285	15.75	0.234	23.388	0.213	27.94	0.234	22.538	0.319	50	0.368	1.15
46.99	0.234	25.476	0.286	15.24	0.234	25.382	0.257	33.78	0.234	25.487	0.344	50	0.399	1.15
30.73	0.234	19.336	0.41	27.69	0.234	20.178	0.347	30.23	0.234	19.251	0.374	50	0.364	1.15
63.25	0.234	34.545	0.312	11.94	0.234	35.501	0.303	59.94	0.234	35.376	0.319	50	0.364	1.15
143.2	0.234	75.487	0.312	8.89	0.234	64.311	0.286	136.3	0.234	75.241	0.336	50	0.381	1.15
51.56	0.234	27.265	0.337	17.01	0.234	29.468	0.269	44.71	0.234	28.572	0.35	50	0.398	1.15
48.51	0.234	25.158	0.445	16	0.234	43.496	0.241	42.67	0.234	24.024	0.383	50	0.398	1.15
54.1	0.234	28.302	0.386	12.19	0.234	59.054	0.175	44.7	0.234	28.307	0.486	50	0.417	1.15

23.62	0.234	14.325	0.379	6.86	0.234	40.4878	0.38	24.13	0.234	12.215	0.386	50	0.423	1.15
24.89	0.234	19.574	0.306	11.94	0.234	19.3058	0.414	64.26	0.234	11.194	0.333	50	0.394	1.150
51.05	0.234	5.5346	0.383	35.31	0.234	6.1654	0.333	30.48	0.234	5.3873	0.349	50	0.397	1.15
51.82	0.234	8.1753	0.322	51.05	0.234	8.4859	0.357	1.524	0.234	9.2135	0.383	50	0.389	1.15
55.63	0.234	7.2009	0.347	47.75	0.234	7.5521	0.365	35.31	0.234	7.3219	0.389	50	0.403	1.15
139.7	0.234	5.5985	0.362	39.62	0.234	6.4254	0.376	25.15	0.234	5.4411	0.378	50	0.414	1.15
32.26	0.234	3.4504	0.373	3.81	0.234	4.5014	0.345	17.78	0.234	4.2825	0.393	50	0.416	1.15
57.66	0.234	6.5624	0.335	1.27	0.234	6.3289	0.258	24.89	0.234	6.5	0.353	50	0.403	1.15
51.56	0.234	6.404	0.357	47.24	0.234	7.2204	0.373	22.61	0.234	6.2588	0.383	50	0.411	1.15
42.93	0.234	6.0206	0.336	42.93	0.234	5.1587	0.382	17.02	0.234	9.0198	0.364	50	0.398	1.15
25.15	0.234	4.3609	0.341	63.5	0.234	4.4901	0.364	17.02	0.234	5.1125	0.381	50	0.4	1.15
17.27	0.234	8.0738	0.348	70.36	0.234	7.4977	0.379	19.05	0.234	8.2852	0.382	50	0.399	1.15
58.93	0.234	9.3319	0.345	19.05	0.234	2.1427	0.388	23.37	0.234	9.4095	0.364	50	0.391	1.15
43.18	0.234	7.478	0.336	14.48	0.234	8.1794	0.333	28.96	0.234	7.2984	0.384	50	0.392	1.15
41.4	0.234	7.3541	0.338	57.15	0.234	7.3384	0.355	29.72	0.234	5.3337	0.379	50	0.378	1.15
28.19	0.234	5.5699	0.321	28.7	0.234	5.542	0.336	36.58	0.234	5.5955	0.367	50	0.373	1.15
31.24	0.234	6.274	0.305	45.72	0.234	6.3205	0.333	44.2	0.234	6.3036	0.348	50	0.373	1.15
40.39	0.234	6.0857	0.318	36.58	0.234	5.2806	0.324	40.39	0.234	5.4311	0.34	50	0.369	1.15
9.144	0.234	2.3427	0.378	2.794	0.234	3.4954	0.333	32	0.234	4.0997	0.411	50	0.372	1.15
20.83	0.234	6.3349	0.337	43.94	0.234	7.5216	0.36	26.92	0.234	7.0737	0.379	50	0.369	1.15
21.34	0.234	5.5999	0.319	7.37	0.234	5.5946	0.329	24.38	0.234	6.0302	0.347	50	0.373	1.15
37.85	0.234	5.0161	0.297	25.65	0.234	5.3037	0.265	34.54	0.234	4.2445	0.333	50	0.37	1.15
10	0.253	0.5801	0.329	10	0.253	1.366	0.273	10	0.253	0.4027	0.352	50	0.291	11
10	0.253	2.486	0.34	10	0.253	1.37	0.362	10	0.253	5.476	0.323	50	0.292	11
10	0.253	1.233	0.212	10	0.253	2.266	0.181	10	0.253	3.044	0.185	50	0.292	11
10	0.253	0.511	0.198	10	0.253	1.425	0.185	10	0.253	1.18	0.228	50	0.289	11
10	0.253	0.464	0.238	10	0.253	0.429	0.271	10	0.253	1.35	0.255	50	0.285	11
10	0.253	0.511	0.282	10	0.253	1.125	0.314	10	0.253	2.343	0.286	50	0.391	11

10	0.253	0.548	0.282	10	0.253	1.25	0.341	10	0.253	4.213	0.253	50	0.287	11
10	0.253	1.552	0.292	10	0.253	2.028	0.325	10	0.253	4.14	0.293	50	0.306	11
10	0.253	0.593	0.272	10	0.253	3.436	0.23	10	0.253	1.565	0.297	50	0.309	11
10	0.253	1.1939	0.272	10	0.253	6.107	0.373	10	0.253	1.026	0.295	50	0.306	11
10	0.253	1.183	0.303	10	0.253	4.222	0.24	10	0.253	2.443	0.306	50	0.289	11
10	0.253	1.188	0.277	10	0.253	1.441	0.299	10	0.253	4.411	0.279	50	0.284	11
10	0.253	1.169	0.283	10	0.253	3.202	0.263	10	0.253	2.174	0.301	50	0.283	11
10	0.253	1.166	0.27	10	0.253	4.106	0.195	10	0.253	4.03	0.267	50	0.267	11
10	0.253	1.077	0.279	10	0.253	2.064	0.298	10	0.253	4.558	0.25	50	0.277	11
10	0.253	1.153	0.273	10	0.253	3.094	0.255	10	0.253	5.08	0.255	50	0.274	11
10	0.253	1.183	0.273	10	0.253	3.117	0.248	10	0.253	3.46	0.275	50	0.277	11
10	0.253	0.556	0.321	10	0.253	2.316	0.273	10	0.253	10.528	0.215	50	0.278	11
10	0.253	1.221	0.256	10	0.253	2.161	0.274	10	0.253	13.24	0.185	50	0.271	11
10	0.253	1.006	0.411	10	0.253	2.286	0.289	10	0.253	2.463	0.409	50	0.324	0.75
10	0.253	0.585	0.385	10	0.253	3.234	0.284	10	0.253	1.402	0.395	50	0.325	0.75
10	0.253	0.565	0.348	10	0.253	4.254	0.248	10	0.253	1.148	0.427	50	0.325	0.75
10	0.253	1.058	0.333	10	0.253	6.375	0.281	10	0.253	1.264	0.426	50	0.324	0.75
10	0.253	1.155	0.334	10	0.253	1.124	0.295	10	0.253	9.4	0.393	50	0.319	0.75
10	0.253	0.573	0.334	10	0.253	1.119	0.377	10	0.253	2.179	0.366	50	0.337	0.75
10	0.253	0.231	0.298	10	0.253	0.223	0.286	10	0.253	0.565	0.381	50	0.382	0.75
10	0.253	1.358	0.259	10	0.253	0.599	0.351	10	0.253	4.545	0.363	50	0.336	0.75
10	0.253	2.531	0.322	10	0.253	2.274	0.329	10	0.253	3.423	0.312	50	0.337	0.75
10	0.253	1.17	0.302	10	0.253	3.494	0.239	10	0.253	2.354	0.301	50	0.318	0.75
10	0.253	2.027	0.244	10	0.253	4.479	0.235	10	0.253	1.4349	0.339	50	0.322	0.75
10	0.253	2.034	0.278	10	0.253	1.446	0.317	10	0.253	3.5091	0.338	50	0.321	0.75
10	0.253	1.442	0.386	10	0.253	6.358	0.246	10	0.253	1.572	0.416	50	0.311	0.75
10	0.253	1.581	0.328	10	0.253	2.342	0.216	10	0.253	3.188	0.327	50	0.316	0.75
10	0.253	1.508	0.293	10	0.253	5.12	0.253	4	0.253	5.232	0.33	50	0.305	0.75

12	0.253	2.277	0.294	10	0.253	1.503	0.299	10	0.253	2.378	0.325	50	0.311	0.75
10	0.253	1.214	0.336	10	0.253	2.436	0.274	10	0.253	3.598	0.306	50	0.314	0.75
10	0.253	0.359	0.295	10	0.253	0.396	0.313	10	0.253	0.398	0.352	50	0.311	0.75
10	0.253	1.244	0.287	10	0.253	2.081	0.272	8	0.253	3.097	0.333	50	0.311	0.75
39.37	0.234	5.1881	0.368	16.92	0.234	6.2901	0.371	29.97	0.234	3.2165	0.411	50	0.387	1.15
31.24	0.234	3.5991	0.395	25.65	0.234	6.3648	0.373	33.02	0.234	3.2759	0.41	50	0.402	1.15
33.78	0.234	4.2745	0.353	26.42	0.234	7.4637	0.336	48.26	0.234	4.329	0.398	50	0.389	1.15
31.75	0.234	3.5674	0.354	25.4	0.234	6.1184	0.294	35.81	0.234	3.2869	0.39	50	0.39	1.15
31.24	0.234	4.1674	0.286	26.16	0.234	8.1113	0.268	34.04	0.234	3.1474	0.338	50	0.33	1.15
35.05	0.234	4.3273	0.305	23.62	0.235	7.5727	0.265	41.15	0.234	3.5443	0.286	50	0.3	1.15
26.67	0.234	5.0922	0.361	39.37	0.234	5.193	0.395	21.34	0.234	5.3518	0.401	50	0.397	1.15
43.69	0.234	8.288	0.363	65.28	0.234	8.4867	0.38	30.48	0.234	9.1783	0.374	50	0.403	1.15
39.37	0.234	8.0773	0.371	76.2	0.234	8.1597	0.398	20.83	0.234	7.5905	0.388	50	0.403	1.15
15.24	0.234	12.2358	0.39	50.8	0.234	5.2234	0.388	15.49	0.234	6.1256	0.351	50	0.402	1.15
35.31	0.234	2.1299	0.38	25.4	0.234	2.3002	0.372	15.49	0.234	4.5915	0.358	50	0.404	1.15
24.13	0.234	5.0934	0.336	39.37	0.234	4.1191	0.337	12.7	0.234	5.0051	0.324	50	0.394	1.15
20.32	0.234	5.0521	0.294	21.81	0.234	5.0776	0.258	21.59	0.234	3.218	0.287	50	0.405	1.15
25.91	0.234	5.2797	0.38	33.78	0.234	6.0046	0.369	33.02	0.234	6.0535	0.396	50	0.415	1.15
39.62	0.234	6.1859	0.361	37.59	0.234	5.5144	0.364	30.48	0.234	6.0749	0.384	50	0.39	1.15
25.91	0.234	4.5856	0.402	22.86	0.234	4.255	0.377	32.51	0.234	4.5465	0.429	50	0.421	1.15
33.78	0.234	5.5088	0.374	19.56	0.234	5.445	0.37	39.12	0.234	5.5797	0.43	50	0.387	1.15
19.05	0.234	7.5695	0.322	39.62	0.234	7.5756	0.348	41.66	0.234	8.1638	0.363	50	0.385	1.15
63.5	0.234	10.29	0.368	28.19	0.234	10.3067	0.346	27.69	0.234	10.359	0.372	50	0.378	1.15
59.69	0.234	9.494	0.381	17.78	0.234	23.1281	0.288	32.77	0.234	20.003	0.374	50	0.406	1.15
29.21	0.234	3.3404	0.429	25.4	0.234	10.028	0.47	25.4	0.234	8.1305	0.475	50	0.478	1.15
25.91	0.234	6.0842	0.453	25.4	0.234	8.5845	0.467	25.4	0.234	8.3009	0.463	50	0.478	1.15
23.37	0.234	18.2953	0.327	39.62	0.234	17.2387	0.664	39.37	0.234	18.028	0.361	50	0.377	1.15
50.8	0.234	4.3308	0.442	25.4	0.234	7.395	0.432	25.4	0.234	5.3977	0.431	50	0.455	1.15

50.8	0.234	5.3085	0.435	25.4	0.234	6.492	0.426	25.4	0.234	7.2088	0.442	50	0.455	1.15
50.8	0.234	4.5666	0.413	25.4	0.234	6.2252	0.421	25.4	0.234	6.148	0.417	50	0.437	1.15
76.2	0.234	6.0803	0.412	25.4	0.234	7.3177	0.408	25.4	0.234	6.5212	0.403	50	0.437	1.15
76.2	0.234	5.133	0.422	25.4	0.234	4.3086	0.418	25.4	0.234	6.2727	0.413	50	0.437	1.15
50.8	0.234	5.1122	0.302	7.62	0.234	8.5452	0.297	25.4	0.234	8.1777	0.304	50	0.315	1.15
50.8	0.234	5.3516	0.311	25.4	0.234	7.4527	0.292	25.4	0.234	7.2013	0.3	50	0.315	1.15
50.8	0.234	5.452	0.293	25.4	0.234	7.4216	0.301	25.4	0.234	8.102	0.298	50	0.315	1.15
50.8	0.234	5.201	0.291	25.4	0.234	7.521	0.303	25.4	0.234	8.2013	0.301	50	0.315	1.15
81.28	0.234	5.0113	0.298	25.4	0.234	7.5076	0.301	25.4	0.234	7.3782	0.292	50	0.315	1.15
33.02	0.234	7.1101	0.3	43.18	0.234	8.1577	0.323	45.72	0.234	8.1652	0.374	50	0.371	1.15
35.56	0.234	2.2102	0.4	5.334	0.234	6.546	0.405	25.4	0.234	6.4425	0.401	50	0.437	1.15